COMPLEXES OF CARBON NANOTUBES WITH IONS AND MACROMOLECULES; STUDIES ON ELECTRONIC CONDUCTION PROPERTIES

BY

PEERAPONG YOTPRAYOONSAK

Academic Dissertation
for the Degree of
Doctor of Philosophy

To be presented, by permission of the
Faculty of Mathematics and Science
of the University of Jyväskylä,
for public examination in Auditorium FYS–1 of the
University of Jyväskylä on June 27, 2014
at 12 o'clock noon

Jyväskylä, Finland
June 2014

Preface

The experimental work reported in this thesis has been done during the years 2009-2013 at Nanoscience Center, Department of Physics in the University of Jyväskylä, Finland.

First of all, I would like to thank my supervisor, Professor Markus Ahlskog, for the guidance and advices as well as for giving me an opportunity to participate and start working for my doctoral study and research in Molecular Technology group.

I would like to thank Dr. Andreas Johansson for his numerous helps and wonderful discussions in all issues as well as the relaxing moments with him and his family.

I acknowledge Dr. Tanja Lahtinen for her helpful collaborative work in the first publication. In addition to the second publication, I am thankful to Dr. Géza Szilvay, Dr. Päivi Laaksonen, and Prof. Markus Linder for their excellent collaboration. Their contributions have paid off perfectly.

I am delighted to know and work with people in Molecular Technology group: Dr. Deep Talukdar, Dr. Davie Mtsuko, Dr. Tuuli Gröhn, Dr. Olli Herranen, Mr. Konsta Hannula, Mr. Matti Hokkanen, Mr. Dongkai Shao and Mr. Ville Saunajoki as well as other people in Nanoscience Center (NSC). They have been a part of my memorable moments in Jyväskylä, Finland.

I am also thankful to Soili Leskinen, Anna-Liisa Blå, Marjut Hilska and Minttu Haapaniemi from the Department of Physics as well as Riitta-Liisa Kuittinen from NSC for their helps on the document administration.

I greatly acknowledge the support from Thai Ministry of Education, the Office of Higher Education Commission, project CHE-PhD-SFR 2007 for a really splendid Ph.D. scholarship.

Eventually, I am very grateful to my parents, my sister, and my brothers in Thailand for their cheerful words, supports and encouragements during the 5 years of my study and living abroad.

Jyväskylä, Finland, June 2014

Peerapong Yotprayoonsak

Abstract

In this thesis we have studied the electronic transport properties of individual single-walled carbon nanotubes (SWNT) in the field-effect transistor configuration (SWNT-FET), and in particular the effect on the SWNTs of various ionic or macromolecular species that form complexes with the nanotube. Experiments have been undertaken on SWNT complexes where the second component is alkali ions (lithium (Li)), or macromolecules like hydrophobin proteins or hemicellulose.

The effect of Li-Tetrahydrofuran-Naphthalene compound to the electrical properties of SWNT-FETs, typically considered as Li-doping, has been explored with gate-transfer characteristic measurements at room temperature. A consistent reversal of semiconducting SWNT electronic properties from p-type to n-type behavior is found, after the Li intercalation process results in a Li/SWNT complex. We also find that the doping mechanism is reversible upon exposure to oxygen and the electronic properties of nanotube devices can be recovered relatively close to their initial values by a simple cleaning method.

The hydrophobins have become interesting due to their excellent adhesive properties. We therefore have studied the adsorption effect of this protein onto carbon nanotubes in terms of gate-transfer characteristics in SWNT-FETs and electron- and scanning probe microscopy. We find that the electrical resistance increases upon exposure to hydrophobins, resulting from mobility degradation due to scattering from the adsorbed hydrophobins.

The electronic properties of asymmetrically contacted SWNT-FETs have been investigated, in which the two contacts to the SWNT have different configurations. In one contact, the electrode metal covers completely the SWNT (embedded contact) while in the other the SWNT is on top of the electrode, and thus potentially more susceptible to interactions with the environment. The temperature dependence of both device configurations has been measured, varying from 300 K to 4.2 K. The electrical

transport measurement of SWNT samples with palladium as metal electrode reveals that the resistance of all asymmetric channels is evidently larger than the resistance of all symmetric channels (which have both contacts of embedded type). The result is ascribed to molecularly thin surface oxidation of Pd.

In addition, we have explored the electronic properties of nanotube network films fabricated from a mixture of hemicellulose and double-walled carbon nanotubes (DWNTs). We have been able to prepare utterly thin DWNT films, where the average thickness of the thinnest one is ~ 8 nm. This hemicellulose-DWNT nanomaterial displays excellent electrical conductivity of $\sim 2\times10^3$ S/cm. The effect of temperature (in the range of 4.2 K - 420 K) and humidity (up to $\sim 90\%$ RH) to hemicellulose-DWNT films has also been investigated in terms of conductivity change.

Author's address   Peerapong Yotprayoonsak
Nanoscience Center
Department of Physics
University of Jyväskylä
Finland

Supervisor   Professor Markus Ahlskog
Nanoscience Center
Department of Physics
University of Jyväskylä
Finland

Reviewers   Dr. Carlos Rodriguez Abreu
International Iberian Nanotechnology Laboratory (INL)
Av. Mestre José Veiga s/n
4715-330 Braga
Portugal

Professor Carita Kvarnström
Laboratory of Materials Chemistry and Chemical Analysis
Department of Chemistry
University of Turku
Finland

Opponent   Associate Professor Noemi Rozlosnik
Department of Micro- and Nanotechnology
Technical University of Denmark
Produktionstorvet, Building 423, 2800 Kgs. Lyngby
Denmark

List of Publications

The main results of this thesis have been reported in the following articles:

A.I   P. Yotprayoonsak, K. Hannula, T. Lahtinen, M. Ahlskog, and A. Johansson, *Liquid-phase alkali-doping of individual carbon nanotube field-effect transistors observed in real-time*, CARBON **49** (2011) 5283-5291.

A.II   P. Yotprayoonsak, G. R. Szilvay, P. Laaksonen, M. B. Linder, and M. Ahlskog, *The effect of Hydrophobin protein on conductive properties of Carbon Nanotube Field-Effect Transistors; A first demonstration and study of the sensing mechanisms*, Submitted (2014).

A.III P. Yotprayoonsak, D. Talukdar, and M. Ahlskog, *Carbon nanotube field-effect devices with asymmetric electrode configuration by contact geometry*, J. Appl. Phys. **115** (2014) 214302.

Author's contribution

The author is the main contributor in all three publications and has participated in all phases of the works from planning to manuscript writing. He has partly contributed to the writing of the first article (A.I) and been the principal author of the two other articles. He has done the sample fabrication, measurements, and data analysis in all the works.

Other work to which the author has contributed:

D. Talukdar, P. Yotprayoonsak, O. Herranen, and M. Ahlskog, *Linear current fluctuations in the power-law region of metallic carbon nanotubes*, Phys. Rev. B **88** (2013) 125407.

D. Talukdar, P. Yotprayoonsak, C.D. Mukherjee, K.K. Bardhan, and B. Karmakar, *Gap states controlled transmission through 1D Metal-Nanotube junction*, arXiv:1404.6730 (27.4.2014).

Contents

1 Introduction

Carbon (C) is classified in the group 4 on the periodic table and has 4 valence electrons which are capable of making covalent chemical bonds. The electron configuration is generally arranged as $1s^2$ $2s^2$ $2p^2$ from which various hybridizations can be constructed, leading to different mechanical and electrical properties. There are a variety of allotropes made up of carbon. Diamond and graphite are the two crystalline structures of carbon but they are formed differently via electron bonding and thus show drastically different behaviors. Diamond possesses sp^3 hybridization in which all electrons are strongly packed in the bonds, resulting in a hard and insulating material. Whereas, graphite presents sp^2 hybridization in which 3 electrons are localized in $2s$ $2p_x$ $2p_y$ orbitals with σ-bonding but leaving one free electron in the $2p_z$ orbital with π-bonding, thus causing brittle and conducting material. However, three additional major types of carbon-based materials have emerged over the past 3 decades: fullerenes, carbon nanotubes (CNTs) and graphene.

In 1985, Kroto et. al. [1] discovered a new carbon allotrope which consists of 60 carbon atoms, and thus it was named as a buckminsterfullerene and it has the molecular formula of C_{60}. The fullerene is a closed carbon structure shaped as a spherical object, like a football, and is also called the buckyball. This pioneering work brought the main authors the Nobel Prize in Chemistry in 1996. Furthermore, a few years later, the discovery of CNTs by Iijima in 1991 [2] has attracted a lot of researchers to intensively study their various properties. The CNTs synthesized by the arc-discharge technique and characterized by transmission electron microscope (TEM) were comprised of several cylindrically concentric honeycomb shells, thus they were called multi-walled carbon nanotubes (MWNTs). A hexagonal structure of 6 carbon atoms (or honeycomb lattice) as in sp^2 hybridization is typically found in CNTs. Soon later, a single tubular shell of CNT was successfully synthesized in 1993 by Iijima et. al. [3] and Bethune et. al. [4]. They were called single-walled carbon nanotubes (SWNTs) and they can be either semiconducting or metallic depending on their chirality. In addition, in 2004, a few atomic layers of graphitic sheets were discovered in isolated form and they were a truly 2 dimensional (2D) material merging together with honeycomb lattices [5]. This single sheet of graphite is called graphene and its electrical properties has been extensively studied since then. Graphene can be considered as a link to the different dimensionalities of carbon allotropes, obviously wrapped into 0D for fullerenes, rolled into 1D for CNTs and stacked into 3D for graphite [6]. The experimental discovery of isolated graphene brought Geim and Novoselov the Nobel Prize in Physics in 2010. Currently, not only graphene has pulled the interest of many scientists but

also the research on CNTs proceeds vibrantly. Graphene and SWNTs are amazingly good candidates for nanotechnological applications in electronics [7].

SWNTs are popular because of the combination of nanoscale diameter and very high aspect ratio. Their diameter can be as small as 0.8 nm but can be several centimeters long [8]. The charge transport properties in this 1D system have been studied at both room- and low temperature [9]. Moreover, SWNTs and derived SWNT-FET devices are extremely sensitive to many physical, biological and chemical factors, being highly promising for biological and chemical sensing applications [10, 11]. The resistance change can be used as a sensing indication for each application.

(a) **(b)** **(c)**

(d) **(e)**
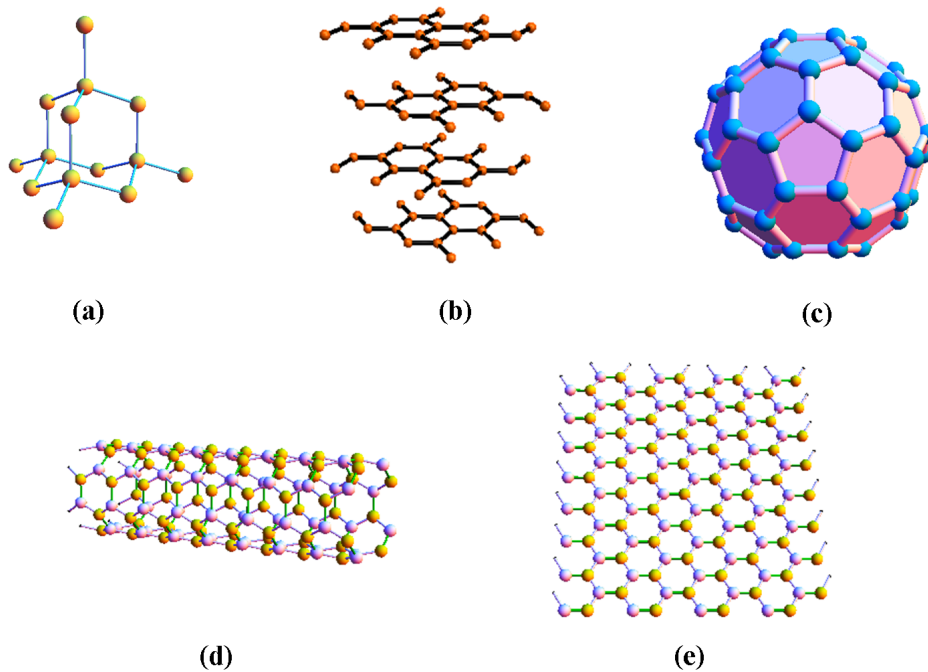
Figure 1.1: Molecular structures of allotropes of carbon-based materials: (a) diamond, (b) graphite, (c) fullerene, (d) single-walled carbon nanotube (SWNT) and (e) graphene.

The interaction of CNTs, especially SWNTs, with ions, molecules, or macromolecules often results in complexes where the latter is bound to the CNT in some non-covalent form. Such complexes are formed above all when CNTs are processed for the purpose of making them dispersible in some solvent. In this manner complexes of CNTs have been made with alkali metals such as Lithium (Li), proteins such as hydrophobin (HFBI), and other macromolecules such as cellulose. The character of the interaction between the CNT and the other species varies, but in all cases, as was argued above, some effect on the electronic properties of the CNT is expected, and in particular in the case of SWNTs.

The content of this Thesis

This thesis mainly focuses on SWNT-based electronic applications, particularly in cases where the SWNT forms molecular complexes. In this thesis, the concepts and fundamentals of CNTs are included for a more clear understanding of them in general (Chapter 2). Here, all experiments (Chapter 3) as well as results (Chapters 4-7) are presented and discussed. The individual SWNTs are fabricated as field-effect transistors (SWNT-FETs) which allow all the electrical measurements to be carried out in different conditions. The following topics are included in this Thesis:

• The doping effects of lithium compound onto SWNT-FET devices are studied (Chapter 4).

• Protein attachment and its influence onto conductance of SWNTs are explored. Individual MWNT field-effect transistors (MWNT-FETs) are also employed, but to lesser extent, to study the detection of biomolecules (Chapter 5).

• SWNT-FETs with different contact configurations are fabricated. The temperature dependence and the sensitivity to oxygen are characterized (Chapter 6).

• The electronic properties of thin conductive films made of double-walled CNTs and hemicellulose compound are studied in by varying the film thickness, temperature and humidity (Chapter 7).

2 Carbon nanotubes

2.1 Fundamentals of carbon nanotubes

Carbon nanotubes (CNTs) are carbon-based materials that basically have a tubular structure with very high aspect ratio (length/diameter). They have been categorized into two main groups according to the number of walls which they contain, namely singled-walled carbon nanotube (SWNT) and multi-walled carbon nanotube (MWNT). The SWNT consists of only one layer throughout its composition whereas the MWNT comprises of many walls along its structure. One can also in particular consider a nanotube configuration which composes of two carbon lattice layers as a double-walled carbon nanotube (DWNT). The diameter of CNTs depends on the number of their walls and can be as small as $\sim$ 1-2 nm for SWNTs [12]. On the other hand, MWNTs can be fabricated with the diameter range around 5-50 nm [13]. Currently with a variety of advanced techniques and tools, researchers are able to achieve the growth process for CNTs with an approximate length of centimeters [8], and thus resulting in an enormously large aspect ratio. The cartoons of different CNT types are illustrated in Figure 2.1.
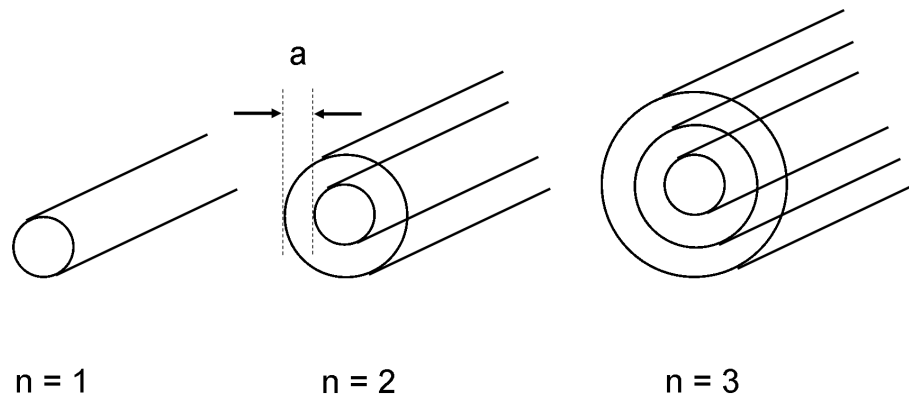
Figure 2.1: Illustrating the profile of SWNT (n = 1), DWNT (n = 2) and MWNT (n $\geq$ 3). In this cartoon, 'n' represents the number of carbon nanotube walls and 'a' is a distance between walls.

2.1.1 Synthesis

Carbon nanotubes can be synthesized by arc discharge, laser ablation and chemical vapor deposition (CVD) techniques. Arc discharge method requires two graphite electrodes with diameter of 5-20 mm spacing ~ 1 mm apart from each other. A low voltage of 12-25 V is usually set while a high current of 50-120 A is then supplied across carbon electrodes. The operating chamber of this method is normally filled with inert gas such as He or Ar at a pressure of 100-1000 Torr [12]. After the arc reaction is finished, CNTs are found to form at the cathode. With an addition of catalyst particles (i.e. Fe, Co, Ni) to the anode, one can produce MWNTs and SWNTs with controllable diameters [12]. Secondly, the laser ablation method uses a composite of Co/Ni catalysts and graphite as a target which is placed in the quartz tube furnace filled with inert gas (He or Ar) at ~ 500 Torr. A pulsed or continuous laser beam is employed to vaporize the graphite target at ~ 1200 °C. Once the graphite source is vaporized, the CNTs (and by-products) are formed in the plasma plume and collected via condensation process at a cold finger [12]. These techniques are suitable for synthesizing large quantities of CNTs however the resulting product typically includes some contaminations e.g. amorphous carbon. The developments on these procedures have been nowadays carried out to produce higher yields and to make the CNT products commercially and inexpensively available in the market.

The CVD method is basically a thermal synthesis with the operating temperature in the range of 900-1200 °C. It thus needs to be done inside the quartz tube with having a mixture of carrier gas (Ar/H_2) and carbon vapor source (i.e. methane, methanol, and ethanol) flowed during the process [12, 14]. The chemical reaction occurs on a substrate that contains metal catalysts, and then the hydrocarbon vapor reacts with catalyst particles to produce SWNTs. This CVD technique provides a wide range of CNTs, varying from large amount formation to individual SWNT composition on several types of Si substrates (e.g. Si/SiO_2 and Si/Si_3N_4). There are currently quite many various CVD procedures that are widely used to fabricate SWNTs for instance HiPCO (High-pressure carbon monoxide) and PECVD (Plasma-enhanced CVD). It has been known that CVD can produce highly pure SWNT materials with higher quality and greater yields than other techniques [12].

2.1.2 Structure and the chirality of carbon nanotubes

Carbon nanotubes are fundamentally a sheet(s) of graphene nano-ribbon rolled up into a hollow cylinder with nanometric diameter. The way of rolling honeycomb lattice layer(s) of carbon atoms into a cylinder is obviously infinite and thus resulting in a huge variety of possible helical geometries (chirality). The nanotube diameter can vary in a range of ~ 1-50 nm. Since CNTs are relatively small (in terms of diameter)

when compared to other conductive materials i.e. thin film (2D) or bulk (3D), they can be considered as either single molecules or quasi one-dimensional crystals with certain translational periodicity along the tube axis [15]. The electronic properties of CNTs are primarily determined by their chirality and diameter as these two factors are directly related to CNT energy band gaps (E_g), thus contributing to semiconducting ($E_g \neq 0$) and metallic ($E_g = 0$) CNTs. However, there is some nanotube structure forming with certain chirality that behaves as semi-metallic conductor (small band gap semiconductor, $E_g \approx 10$ meV) [16].

Because a SWNT can be geometrically obtained by rolling up a single layer graphene sheet, one can start studying the geometry of graphene in order to make it clear how SWNTs are made with various chiralities. In addition to that, exploring the band structure of graphene can potentially lead to better understanding of the band structure of CNTs and their electronic properties [17], as will be discussed in the next section.

Basically, a graphene ribbon consists of carbon atoms constructed periodically with hexagonal lattice configuration, as shown in Figure 2.2. When wrapping this graphene sheet, the structure of obtained SWNTs can be described by a chiral vector ($\mathbf{C}_h$)- a vector that connects two crystallographically equivalent sites on a graphene sheet [15]. The chiral vector used for honeycomb lattices is defined as

$$\mathbf{C}_h = n\mathbf{a}_1 + m\mathbf{a}_2 \tag{2.1}$$

Where n and m are integers and can be considered as a pair of indexes (n,m) whereas $\mathbf{a}_1$ and $\mathbf{a}_2$ are the unit vectors of a hexagonal lattice. These two lattice vectors are given by:

$$\begin{aligned} \mathbf{a}_1 &= (\frac{\sqrt{3}}{2}a, \frac{a}{2}) \\ \mathbf{a}_2 &= (\frac{\sqrt{3}}{2}a, -\frac{a}{2}) \end{aligned} \tag{2.2}$$

Where a is the lattice constant of a graphene sheet and $a = \sqrt{3}a_{CC}$, where a_{CC} is the distance between two carbon atoms in graphene lattice as constant value of $a_{CC} \approx$ 1.42 Å. Hence a is estimated to be $a \approx 2.46$ Å.

Since the chiral vector ($\mathbf{C}_h$) when rolled from graphene sheet goes along the nanotube cross section perpendicular to the tube axis and it finally ends up at its original position, this chiral vector actually defines the circumference of nanotubes. The diameter (d_t) of any SWNTs can be then derived from

$$d_t = \frac{|\mathbf{C}_h|}{\pi} = \frac{a}{\pi}\sqrt{n^2 + nm + m^2} \qquad (2.3)$$

The specific chiral angle (θ) - an angle between the chiral vector and the unit vector $\mathbf{a}_1$ (see Figure 2.2) - is also obtained from the fundamental vector analysis as

$$\theta = cos^{-1}(\frac{\mathbf{C}_h.\mathbf{a}_1}{|\mathbf{C}_h||\mathbf{a}_1|}) = cos^{-1}(\frac{2n+m}{2\sqrt{n^2 + nm + m^2}}) \qquad (2.4)$$

This chiral angle is limited in the range of $0 \leq \theta \leq 30°$ owing to the symmetry of the hexagonal lattice [15]. When $\theta = 0°$, the structure of SWNTs is then determined by (n,0) indices and they are called zigzag tubes because they display a zigzag pattern along their circumference. The carbon-carbon bonds of these zigzag tubes basically arrange in parallel to the tube axis. While $\theta = 30°$, the chiral vector of SWNTs is then defined by (n,n) indices and they are called armchair tubes as the atomic pattern along the circumference is found to be an armchair configuration. The carbon-carbon bonds of these armchair tubes actually exhibit in perpendicular to the tube axis. We can consider both zigzag and armchair nanotubes as achiral tubes, the rest however are chiral tubes with (n, m $\neq$ n $\neq$ 0) indices (see Figure 2.3).

2.1.3 Electronic properties of carbon nanotubes

As already stated above, the graphene lattice is a perfect material to start discussing for later having a clear idea about the electronic properties of CNTs. The honeycomb lattice of graphene is constructed with single carbon bonds (C-C) where each carbon atom binds to other three carbon atoms to form a network (see Figure 2.2). Carbon has four valence electrons and in this particular structure only three orbitals (s, p_x, p_y) form a planar sp^2 hybridization with σ bonding and σ^* anti-bonding states [15]. The σ bonds tie up with covalent interactions which accounts for the binding energy and mechanical properties of the graphene sheet, and they do not contribute to the electrical conduction of graphene. The electronic properties are therefore determined by the remaining electrons in p_z orbitals ($\hat{z}$ is perpendicular to the graphene sheet) that form with π bonding as well as π^* anti-bonding states, and there is no interaction between the σ and the π orbitals due to their different geometries [17]. These π orbitals are mobile (delocalized) and play a major role in the electrical conduction of graphene and carbon nanotubes [15].

In the graphene lattice, the unit cell consists of two carbon atoms, as represented by point A and B in Figure 2.4 (a). By using Fourier transform of the real space into
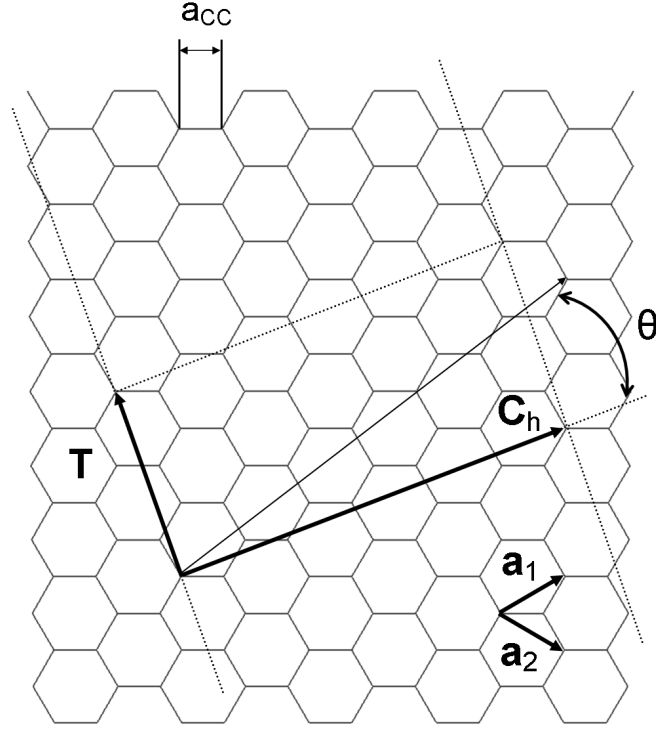
Figure 2.2: Hexagonal lattice of graphene ribbon with lattice vectors $\mathbf{a}_1$ and $\mathbf{a}_2$ pointing as the directions shown in the Figure. $\mathbf{C}_h$ is the chiral vector used for wrapping graphene sheet into a tubular structure, and finally becoming a tube circumference. The chiral angle (θ) is defined by $\mathbf{C}_h$ and $\mathbf{a}_1$ vectors. The translational vector ($\mathbf{T}$) is given by $\mathbf{T} = t_1\mathbf{a}_1 + t_2\mathbf{a}_2$, where (t_1, t_2) are integers. a_{CC} is a carbon-carbon bond length. Adapted from Ref. [17].

k-space, the reciprocal lattice can be obtained as shown in Figure 2.4 (b) and the reciprocal lattice vectors ($\mathbf{b}_1$ and $\mathbf{b}_2$) are given by:

$$\mathbf{b}_1 = (\frac{2\pi}{\sqrt{3}a}, \frac{2\pi}{a}), \quad \mathbf{b}_2 = (\frac{2\pi}{\sqrt{3}a}, -\frac{2\pi}{a}) \tag{2.5}$$

The first Brillouin Zone (BZ) is hexagonal (grey color in Figure 2.4 (b)) and it comprises of three symmetry points namely Γ at the center, K and K′ at the corners of the first BZ. These points are crucial for calculating the electronic band structures of graphene.

The energy dispersion relation of graphene can be calculated by the tight-binding approximation model and obtained as:

$$E(k_x, k_y) = \pm\gamma_0\sqrt{1 + 4cos(\frac{\sqrt{3}k_xa}{2})cos(\frac{k_ya}{2}) + 4cos^2(\frac{k_ya}{2})} \tag{2.6}$$

(10,0)   (10,10)   (10,5)
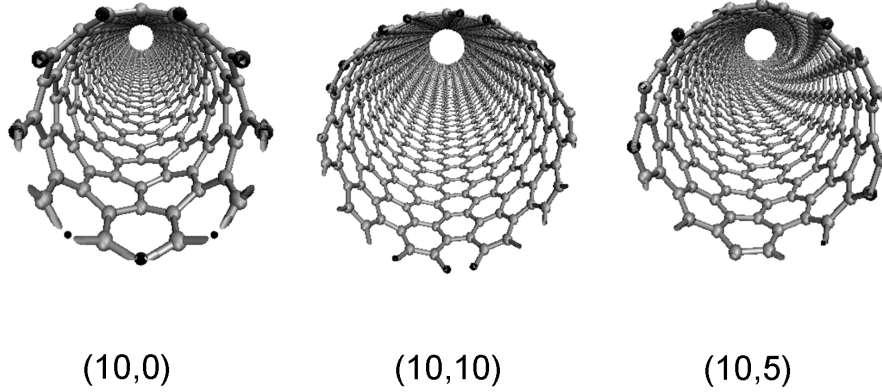
Figure 2.3: Illustrating 3 different types of SWNT's chirality. The zigzag (10,0), armchair (10,10) and chiral (10,5) configurations are displayed from left to right, respectively.

where γ_0 is the overlap integral between the two first-neighbor π orbitals. From equation (2.6), there are obviously two energy branches according to two signs of the dispersion relation, corresponding to the upper energy band (π bonding) and the lower energy band (π^* anti-bonding). These two bands meet each other at the points where E = 0 and the crossing points appear at six K points (3 positions of each K and K' points) at the corners of the first BZ (see Figure 2.5 (a)) [17]. At these vertices there is no energy gap between the bands in K-points, and thus resulting in a zero bandgap semiconductor.

When a graphene sheet is rolled up into a tubular structure, the wavefunctions around the tube circumference are quantized as a consequence of periodic boundary conditions, they in contrast are continuous along the tube axis. The discrete allowed wavevectors can be drawn through the first BZ of graphene as parallel lines (see Figure 2.5 (b)). These lines correspond to the allowed states and can intersect or miss the K and K' points at the corners of BZ. If at least one line crosses the K point, the carbon nanotube is metallic (no energy gap, $E_g = 0$) but if no lines cross the K point, the nanotube is semiconducting. The dispersion relation of metallic nanotubes is linear near the Fermi level (E_F) whereas the dispersion relation of semiconducting nanotubes is non-linear and separated by energy gap (E_g) [15]. The band gap of semiconducting tubes can be calculated as:

$$\triangle E_g = \frac{2\gamma_0 a_{CC}}{d_t} \approx \frac{0.8eV}{d_t(nm)} \tag{2.7}$$

It is evident that the semiconducting gap is inversely proportional to its diameter, thus relatively large for small diameter SWNTs.
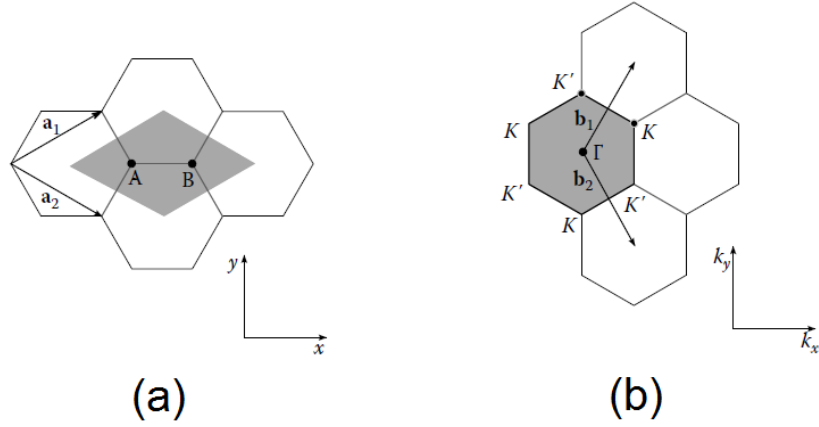
Figure 2.4: (a) Graphene honeycomb lattice with two-carbon basis (A and B), the unit cell (grey area) and the real-space lattice vectors $\mathbf{a}_1$ and $\mathbf{a}_2$. (b) The reciprocal space of graphene with the first Brillouin zone (grey area) and the reciprocal lattice vectors $\mathbf{b}_1$ and $\mathbf{b}_2$. Adapted from Ref. [17].

The prediction whether a carbon nanotube is metallic or semiconducting can be achieved by a simple calculation of chiral indices (n,m). Armchair nanotubes (n = m) are always metallic while zigzag and chiral nanotubes are semi-metallic (or small band-gap semiconductors) if n - m = 3i $\neq$ 0 where i is a non-zero integer, and the rest of zigzag and chiral tubes where n - m = 3i $\pm$ 1 are semiconducting with different bandgap values that can be roughly calculated by the given equations 2.3 and 2.7. From these chirality relations, we are able to estimate that $\sim$ 1/3 of the nanotubes are metallic and the rest is semiconducting [16].

The density of states (DOS or D(E)) represents the number of available states (N(E)) per unit energy range (E) and it is defined as:

$$D(E) = \frac{dN(E)}{dE} \tag{2.8}$$

The feature of DOS strongly depends on dimensionality of the studied material. In a one dimensional (1D) system, the DOS is inversely proportional to the square root of the charge carrier energy ($\sim E^{-1/2}$ dependence) [19]. It thus yields the spike characteristics at certain energies when the fraction is very small and the DOS diverges to those extreme peaks, as can be seen in Figure 2.6. These peaks are so-called Van Hove singularities (VHSs). Since SWNTs are relatively small, they can be considered as quasi-1D objects and their DOS is similar to a 1D object.

In Figure 2.6, it is obvious that there are always available states (DOS) in metallic CNTs (image (a)) because two electronic bands in the dispersion relation cross at the Fermi level. Therefore metallic nanotubes have no band gap but constant DOS at the
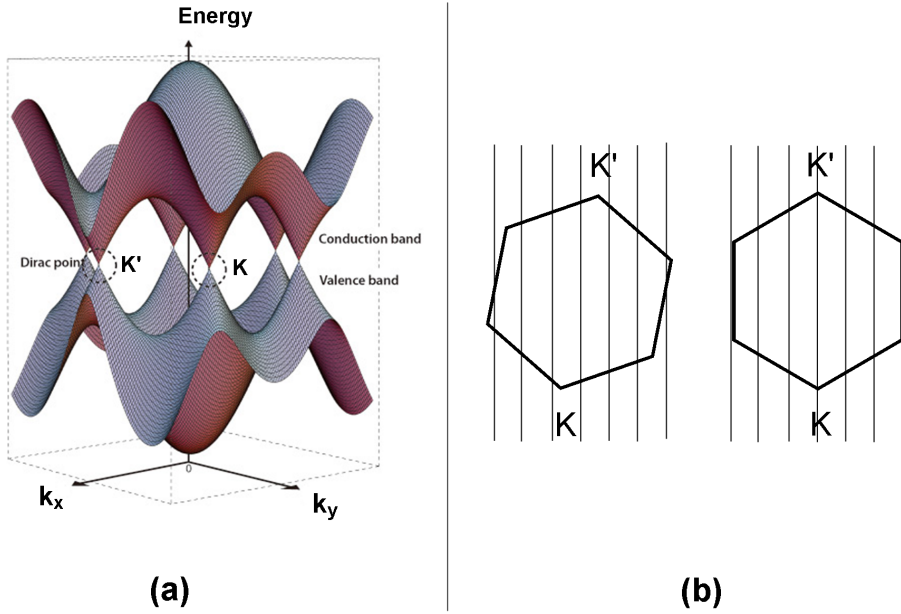
Figure 2.5: (a) The energy dispersion of graphene in 3D. The intersections of π (upper band) and π^* (lower band) orbitals at K and K′ points are called Dirac point, then indicating a zero-bandgap in graphene. (b) Quantization of allowed states of carbon nanotubes on graphene Brillouin zone. Right: armchair tube where the quantized wavevectors always cross the K-points, thus leading to a metallic tube. Left: zigzag and chiral tube where the quantized wavevectors can either meet or miss the K-points, thus contributing to either a quasi-metallic or semiconducting tube, respectively. Adapted from Ref. [18].

Fermi level as

$$D(E_F) = \frac{2\sqrt{3}a_{CC}}{\pi\gamma_0|\mathbf{C}_h|} \tag{2.9}$$

For the case of semiconducting CNTs (image (b)), there are no allowed states at the Fermi energy which basically implies that $D(E_F) = 0$. This forbidden band results in an energy gap (E_g) near the Fermi level in their electronic structure, therefore splitting the energy band into the valence band (E_V) and the conduction band (E_C). The semiconducting band gap of SWNTs is simply calculated by $E_g = E_C - E_V$. Notably, the Van Hove singularities are visible in both cases.
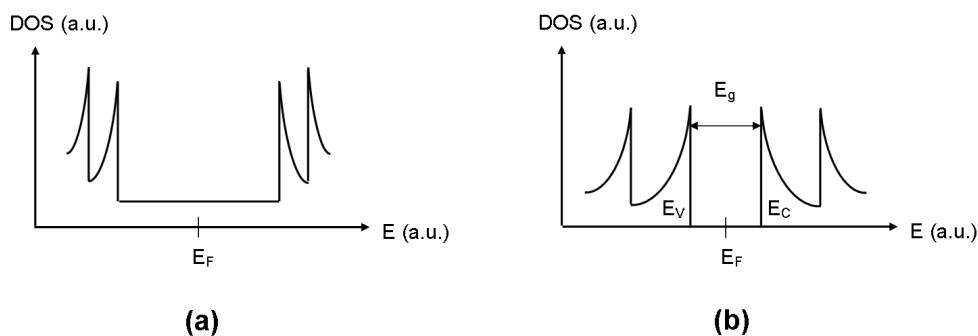
Figure 2.6: The density of states (DOS) for metallic CNTs (a) and semiconducting CNTs (b). The metallic tubes has a constant DOS and has no energy bandgap at Fermi level whereas there is a band gap ($E_g = E_C - E_V$) existed in semiconducting tubes but no DOS at Fermi level. Adapted from Ref. [15].

2.1.4 Colloidal dispersibility and functionalization of carbon nanotubes

Carbon nanotubes are proposed to be exploited in many applications in different ways such as individual CNTs or CNT network [20]. There are however some obstacles to obtain a well-dispersed CNT suspension because as-grown CNTs (in terms of mass production for a commercial need) typically aggregate in a powder form with strong van der Waals interactions and they also contain a tiny amount of amorphous carbon [21]. The van der Waals forces occur everywhere between nanotubes and their actions can stack and entangle them into big particles. These serious factors result in a difficulty to disperse CNTs in normal manners and thus contributing to a poor colloidal dispersibility in both aqueous and non-aqueous solvents [20]. SWNTs are essentially found to be as ropes or bundles with a diameter of 10-30 nm and efforts have been made for some time to properly disperse these huge molecules [21].

When using some common methods to separate CNT bundles for instance treating with acid or sonication, it is crucial to note here that these powerful techniques can potentially damage nanotubes [21–23]. It also has been discovered that CNTs after the harsh treatments are shorter and have more defects on their sidewalls. On the other hand, there is another successful approach to increase the colloidal dispersibility of CNTs: that is to functionalize them with either chemical or biological molecules. Each type of functionalizing molecules interacts differently with the CNT sidewalls, and therefore yielding a variety of functional and electrical properties. Depending on the binding strength to CNTs, one can briefly divide the functionalization method into 2 groups, namely covalent and non-covalent modifications [21]. Both interactions of course can make nanotubes highly dispersible but in the case of covalent functionalization the chemical molecules are able to alter the optical and electronic properties of CNTs [24]. In a few particular covalent modifications, SWNTs are essentially found as

ropes or bundles [25]. Therefore non-covalent functionalization is somewhat promising to mildly modify CNTs and solubilize them without disturbing their π system, and so having unchanged electronic properties. This gentle functionalization can be achieved by a simple technique of mixing pristine CNTs with some chemicals and/or proteins including DNA (as surfactants) and/or active alkali-salt solutions [20, 21, 26, 27]. Indeed, functionalization of CNTs not only enhances their dispersibility in aqueous solutions but also make them functional for specific uses i.e. immobilization of proteins and other smaller biomolecules as biosensors or detection of chemical vapors as gas-sensors.

2.2   Electrical transport in carbon nanotubes

2.2.1   Fundamental transport phenomena in carbon nanotubes

In carbon nanotubes, the electrons around their circumference are very confined, especially in SWNTs, and therefore can be truly considered as a quasi-1D material due to their extremely small diameter [28]. The electron transport in nanotubes relates to three characteristic lengths of the mesoscopic system: the mean free path (L_m), localization length (L_0), and phase coherence length (L_ϕ) [29, 30]. The mean free path is the length scale that electrons travel freely before scattering on defects or impurities. The localization length describes the elastic scattering of electrons without losing their phase and the phase coherence length is the length that electrons as waves maintain their coherence property before inelastic scattering. These length scales are involved in the scattering mechanisms in nanotubes which can typically be electron-phonon scattering, electron-defect scattering as well as electron-electron interaction, and thus crucially resulting in the resistance of CNTs. The nanotube resistance (R_{CNT}) strongly depends on the distance between metal electrodes contacted to CNT itself (channel length (L) of the conductor) compared to the characteristic length scales since it determines whether the charge carriers inside CNT can travel with or without scattering. The electrical transport corresponding to the channel length of CNT device is basically divided into several groups but only ballistic transport, diffusive transport and strong localization transport regimes are discussed in this chapter. However, there is a mismatch of the number of states to allow the incoming and outgoing current transport to occur between the continuous states of metal electrodes and the discrete states (modes) of CNT that contributes to a quantized contact resistance (R_Q) [28]. This kind of resistance always exists in CNT device constructed with metal contacts. In addition to the quantum resistance, the difference of electronic structures, particularly work function, between metal electrodes and CNT can cause potential barriers at metal-CNT interfaces which is the so called Schottky barrier. This kind of barrier is more pronounced in the case of metal/semiconducting CNT junctions. Certainly

the contact resistances (R_C) always exist in the CNT devices and the total resistance of one device is given as:

$$R_{device,tot} = R_{CNT} + R_C \tag{2.10}$$

Notably the quantum resistance is ideal and unavoidable for CNT devices nevertheless one can reduce (or even remove) the contact resistances resulting from the Schottky barriers by choosing the proper metal with having a work function compatible to CNT band structure [9]. Without Schottky barrier, the total resistance appeared in ballistic conduction is only the quantum resistance, R_Q.

Ballistic transport

In the case when channel length of the sample is shorter than the mean free path (L < L_m or L < L_ϕ, L_0), the electronic conduction in CNT is ballistic - that is, no scattering or energy dissipation of charge carriers inside CNT exists. This implies that there is no resistance in the nanotube, thus no voltage drop across the ballistic CNT. However there are in fact the quantum resistances (or inversely quantum conductance, G_Q) at the metal-CNT interfaces which are associated with the different allowed-state distribution of electrons that can transport into CNT and come out to metal electrodes. These resistances lead to the voltage drop at the electrode-nanotube contacts when the source-drain potential is applied to a ballistic CNT device. The electrical transport in ballistic regime for a typical 1D conductor can be explained by the Landauer equation as [31]:

$$I(V) = \frac{4e}{h} \int [F(E) - F(E + eV_D)]T(E)dE \tag{2.11}$$

Where V_D is the drain voltage, F(E) is the Fermi distribution function and T(E) is the energy dependent transmission probability. By taking the difference of chemical potentials at both metal-CNT contacts into account, the quantum conductance (G_Q) of a 1D object can be simplified and obtained as [29]:

$$G_Q = 2e^2MT/h \tag{2.12}$$

Where M is the number of modes (or subbands) and T is the average transmission probability. Since the factor $2e^2/h$ is constant and equal to 7.75×10^{-5} S (or $h/2e^2 \approx 12.9$ kΩ), the resistance of a single-mode 1D conductor with perfect contacts and

electron transmission (M = 1 and T = 1) is $R_Q = G_Q^{-1} \approx 13$ kΩ. In the case of ballistic SWNTs, there are basically two modes (subbands) available for the electrical transport and thus the maximum conductance (or minimum resistance) of such ballistic nanotube device estimated by equation (2.12) at M = 2 and T = 1 is: $G_Q = 4e^2/h \approx 1.55\times10^{-4}$ S (or $R_Q = h/4e^2 \approx 6.5$ kΩ) [28].

Diffusive transport

In the diffusive regime, L_ϕ is shorter than both L and L_0 ($L_\phi <$ L, L_0) and the inelastic electron-phonon scattering is dominant [30]. This implies that the traveling electrons are not encountering the localized states caused by either defects or impurities but inelastically scattering with phonons. In this regime, the electrical transport is controlled by the diffusive propagation of electrons. The diffusive transport in CNTs can be basically observed at low bias and clean samples, thus L_0 is relatively long. Since electrons travel diffusively inside the sample, one can expect to obtain Ohmic transport behavior where the resistance is linearly proportional to the length of 1D sample (or G is inversely proportional to the sample length, L). The conductance of a sample in diffusive regime can be estimated by a phenomenological relationship between the conductance and the scattering rate as [15]:

$$G \approx 2e^2/h.(L_{ie}/L) \tag{2.13}$$

Where L_{ie} is a typical inelastic scattering length ($L_{ie} \sim$ 1-2 μm at 300 K). It should be noted here that the temperature of the sample in this electron-phonon coupling regime also affects the decoherence mechanisms and the inelastic scattering rates [15].

Strong localization transport

In the imperfect nanotubes containing a large number of defects and impurities and supplied with low bias voltage, the strong (Anderson) localization regime governs the transport mechanism. Under these conditions (or $L_0 <$ L $< L_\phi$), the electrons are localized by the random potentials of the defects and impurities. The localized electron wavefunctions have a size of the same order as the localization length, L_0. The electron transport of CNT devices in this regime can thus be only a tunneling process - that is, the hopping transport from one localized state to the other. As a consequence of tunneling conduction, the nanotube resistance becomes exponentially dependent on the length of the nanotube [30] and is given by:

$$R \approx R_0 exp(L/L_0), \quad or \quad G \approx G_0 exp(-L/L_0) \tag{2.14}$$

Particularly, it should also be mentioned that the electronic transport in 1D system (CNTs in this case) is determined by many important factors, and thus resulting in different transport regimes. These parameters, for instance dimension and structural cleanliness of the samples, the system temperature and the bias voltages, need to be known in order to analyze the electrical transport mechanisms inside the samples pertinently in the right regime.

2.2.2 Transport in single-walled carbon nanotube field-effect transistors (SWNT-FETs)

The first carbon nanotube field-effect transistors (CNT-FETs) were successfully demonstrated in 1998 at Delft and at IBM [12]. The CNT-based transistors were fabricated in such a way that a few of semiconducting nanotubes were deposited on top of two metal electrodes which were initially pre-patterned on silicon (Si) substrate covered with silicon dioxide (SiO_2) acting as a back gate. The p-type FET behaviors of CNT devices were achieved with several orders of magnitude in ON/OFF current ratio (I_{ON}/I_{OFF}). They however noticed that even at ON-state conduction the resistance of CNT devices was quite high, at ~ 1 MΩ [12]. This implied that the contact resistance of such devices was also evidently high. Since then, there have been lot of efforts to reduce contact resistances and improve the entire resistance of CNT-FETs to be as small as quantum resistance limit ($R_Q \sim 6.5$ kΩ for ballistic CNTs) for further applications in nano-electronic devices. Eventually ballistic conduction in CNT-FETs has been achieved by using an individual semiconducting-SWNT as a conducting channel with palladium (Pd) electrodes deposited on top [9]. The resistances of SWNT devices in that study were of course not extremely close to R_Q but they have at least obtained $R_{ON} \sim 10$ kΩ for short channel length of ~ 300 nm (nearly ballistic channel) and $R_{ON} \sim 37$ kΩ for long channel length of ~ 3 μm (diffusive channel) [9].

It is important to understand how the contact resistance occurs and how it influences in CNT-FETs. The idea of the Schottky barrier is also indeed necessary to discuss because this particular barrier plays significant roles in electronic transport in CNT-FET devices.

Schottky barriers

A potential energy barrier that forms at the contacts between metal and semicon-

ductor is called the Schottky barrier. Its feature strongly depends on the electronic structures of both materials for instance the band alignment, the work function (Φ) and the energy gap (E_g). Basically the height (Φ_{SB}) of this particular barrier is directly related to the work function and band gap [32, 33], specifically to conduction band (E_C) and valence band (E_V). The work function is in general the minimum energy required to remove one electron from a solid to the vacuum state (E_{vac}) and thus for metal (Φ_M) is simply defined as the energy difference between vacuum level and metal Fermi level ($E_{F,M}$), $\Phi_M = E_{vac}$ - $E_{F,M}$. In the case of semiconductors e.g. S/C-CNTs, the work function is basically referred to the electron affinity (χ) that is the energy difference between the vacuum level and the conduction band ($\chi = E_{vac}$ - E_C) and their workfunction (Φ_{CNT}) therefore according to the definition can be given as a sum of electron affinity and a half of energy gap, $\Phi_{CNT} = \chi + E_g/2$ [34]. The relation of these energy parameters is schematically displayed in Figure 2.7.

Before the metal and semiconductor are electrically bridged, their band alignments are in equilibrium state as shown in Figure 2.7 (a) and in fact their Fermi energy can be placed in different levels. The Fermi level of intrinsic semiconductor is however definitely aligned at the middle of the band gap because the DOS is symmetric around the Fermi energy. When they are then brought into contact, the Fermi levels of both materials are re-balanced into a new equilibrium condition and eventually ended up with aligning at the same level [32]. During the balancing process, there is a charge transfer mechanism happened as the charge carriers are also transferring between metal and semiconductor contacted-junctions. These phenomena contribute to the band bending of semiconductor and the Schottky barrier is formed at the interface with various possible sizes. The barrier height and width are relevant to the bandgap size of semiconductor as well as the Fermi-pinning level at the interface. Nevertheless in one-dimensional metal-semiconductor system (i.e. metal-CNT), the Fermi-level pinning is not strongly effective due to the limitation of length scales of the channel diameter (a few nanometers in the case of SWNTs) [12].

The Schottky barrier for p-type transport (holes as major charge carriers) is constructed between Fermi level of metal and valence band of CNT whereas for n-type transport (electrons as major charge carriers) is formed at conduction band of CNT (see Figure 2.7 (b) and (c) respectively). Both barrier types can be given as:

$$\Phi_{SB,p} = \chi + E_g - \Phi_M, \qquad \Phi_{SB,n} = \Phi_M - \chi \qquad (2.15)$$

Noticeably, semiconducting CNTs with large diameters (i.e. $\sim$ 3 nm) have small band gaps ($\sim$ 0.3 eV, estimated by using equation 2.7) and therefore the Schottky barrier for one type of carriers is always small ($<$ 250 meV) no matter what kind of metal is used to contact to CNTs [12].

Depending on the work function of metals, the nanotubes (work function reported $\sim$ 4.7 - 4.9 eV [35]) contacted with high work function metals such as palladium (Pd) and gold (Au) tend to have p-type barriers while the low work function metals such as yttrium (Y) and scandium (Sc) most likely yield n-type barriers when connected to CNTs [36]. The Fermi level of CNTs with p-type contact lies close to valence band whereas aligning close to conduction band for n-type contact. The electrical transport through the Schottky barrier is basically based on the thermally assisted quantum tunneling [12]. The tunneling current is exponentially dependent on the barrier thickness for a fixed source-drain voltage (V_{ds}) [34]. Besides the thickness of this particular barrier can be modulated by gate potential (in terms of FET configuration), and thus leading to the regulation of charge transport (or switching of the current conduction) in semiconducting CNT devices.
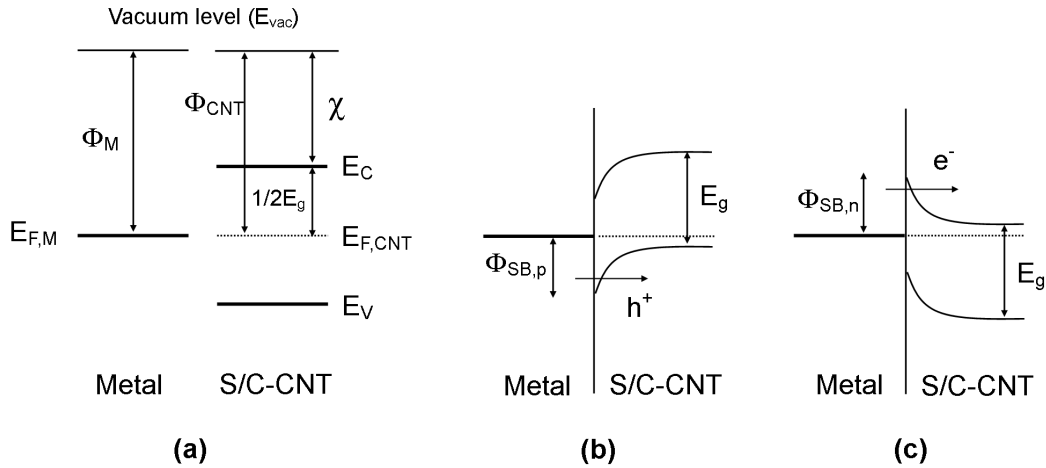
Figure 2.7: Schottky barrier formation at metal/semiconducting-CNT (S/C-CNT) interface. (a) The energy bands of metal and CNT at equilibrium state before getting contacted. (b) A p-type Schottky barrier (hole conduction, h$^+$) is formed after connection between a S/C-CNT and a high work-function metal. (c) An n-type Schottky barrier (electron conduction, e$^-$) is formed with low work-function metal.

Transport properties of semiconducting and metallic SWNT-FETs

In the semiconducting SWNTs fabricated with FET configuration (SWNT-FETs), the electrical transport can be dominated by either holes (p-type) or electrons (n-type). One type of these carriers is driven in the SWNT devices by the potential difference supplied across source and drain electrodes, V_{ds} [13]. The drain current (I_d) through SWNTs is measured and results in the I-V_{ds} characteristics, thus providing the intrinsic properties of nanotubes such as resistance. Besides with the help of external electric field produced by the gate voltage (V_g, either back or top gate), one

can modulate the alignment of nanotube bandgap (or basically Fermi level) and this action leads to controllable electronic conduction in SWNT-FET devices [13]. The mechanism of gate voltage dependence is schematically demonstrated in Figure 2.8, with different supplied gate potentials. Without any applied gate voltage ($V_g = 0$), the electronic structure of nanotubes remains neutral and the Fermi level lies at the middle of band gap. By applying positive gate voltage ($V_g > 0$), the bandgap level of nanotube is diminishing (conduction band lowering close to Fermi level) and then yielding more available states for electron conduction (n-type) - and of course less available states for hole injection. On the other hand, the valence band of nanotube is rising toward the Fermi level (bandgap level is lifting up) when applying negative gate voltage ($V_g < 0$) and then more allowed states for hole conduction (p-type) - of course less allowed states for electron injection [37].
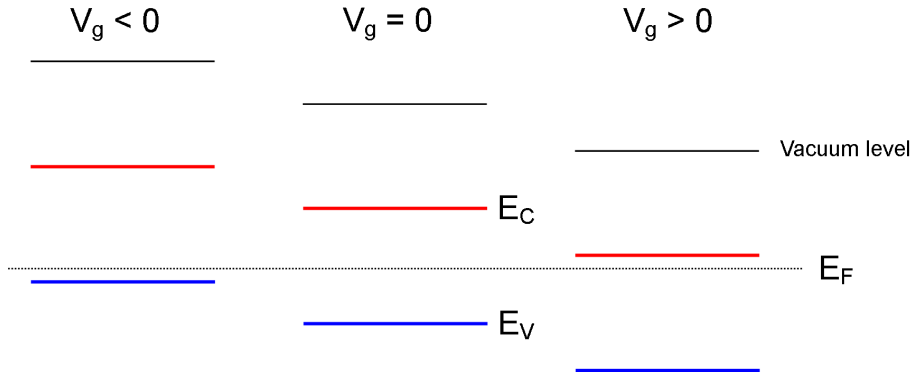
Figure 2.8: The field effect to band structure of an intrinsic semiconductor (i.e. S/C-CNT) as a consequence of the applied gate voltages. The gate modulation influences the number of available states in the electronic structure of S/C-CNT, corresponding to the current conduction through the channel.

For semiconducting SWNT devices, there can be p-type FETs (holes dominated) and n-type FETs (electrons dominated), which are unipolarly behaving (see Figure 2.9 (a) and (b) respectively). The drain current plotted in log-scale is observed to be in saturation at ON-state (I_{ON}) and OFF-state (I_{OFF}) conductions. The gate voltage at which the conduction switches on or off is defined as the threshold voltage, V_{th}. It is a device-dependent parameter and it can be any value but it is also difficult to determine V_{th} unambiguously. However in the case of large diameter nanotubes, the Schottky barrier heights are small because of a small band gap and the electrical conduction can be obtained by both holes and electron in the same device [12]. It is commonly called the ambipolar transport (see Figure 2.9 (c)). In such ambipolar SWNT-FETs, they consist of p-type and n-type transport corresponding to the applied gate voltages and the gate potential difference from having electron transport to hole transport can be estimated as $\sim \Delta V_g$.

For metallic SWNTs, there is no such band gap and their electrical response to the

gate potential is observed to be extremely weak, nearly no gate dependence at all (see Figure 2.9 (d)). Therefore one will not be able to indicate the important electronic parameters from metallic SWNT-FET devices for instance I_{ON}, I_{OFF} and the subthreshold slope.

Nevertheless only p-type and n-type SWNT-FETs have been currently utilized in nano-electronic applications because they indeed provide several substantial abilities with extremely small dimension (1D) [9, 38]. For example, they can be used as biological- and chemical- nanosensors with excellent sensitivity and efficiency [10, 11, 14, 16]. Furthermore they show very promising FET properties in terms of fast switching ON-to-OFF response with huge ON/OFF ratio as close to silicon-based transistors and they are likely to be fabricated as memory devices in the near future [7, 39].
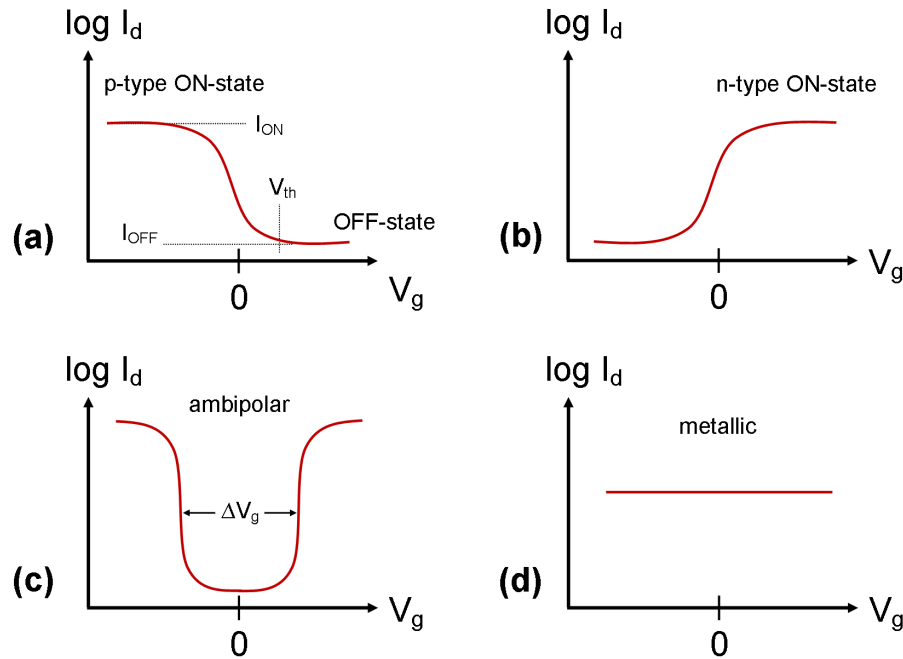
Figure 2.9: Illustrating the FET characteristics of semiconducting and metallic SWNTs. The S/C-SWNTs can perform as p-type (hole transport), n-type (electron transport) or ambipolar (both hole and electron transport) FETs, shown in (a), (b) and (c) respectively. On the contrary, metallic SWNTs (d) cannot perform as FETs due to zero bandgap and then no gate response.

3 Sample fabrication and characterizations

In this study, single-walled carbon nanotube field-effect transistors (SWNT-FETs) are the major tool to explore the effect of various environments, i.e. solutions, oxygen, vacuum and low temperature conditions, to the electronic properties of CNTs. The samples were fabricated in cleanroom with a top-down technique and followed the standard microfabrication procedure. Electron beam lithography was used for the exposure process. A highly p-doped silicon chip having a thin thermally-grown dielectric layer on top of it was chosen to be a substrate and to act as a back gate. The details of the whole fabrication method are described in section 3.1 and a few changes are explained in section 3.2. However in this Thesis, there are two different structures of electrode configurations contacted to CNTs which are exploited for different purposes, as following.

- In Chapters 4 and 5; SWNT-FET device which has both source (S) and drain (D) electrodes electrically placed on top of CNT is performed to investigate the influences on the electronic properties of CNT in the presence of, firstly Li compound and, secondly protein molecules. The actual aims of this device configuration are to utilize as chemical and biological sensors, respectively. The schematic of this device with operational circuits is illustrated in Figure 3.1 (a).

- In Chapter 6; SWNT-FET device which has two electrodes deposited on top of CNT but has one electrode placed underneath CNT is used to study the effects on electrical transport of CNT with different contact configurations. This kind of specifically-made device is basically referred to 'asymmetric contact' FET device because it consists of both symmetric and asymmetric sections within the same CNT. The effects of having different tube-contacted features are studied in various conditions, in vacuum and oxygen environments as well as low temperature condition. The schematic of this device with operational circuits is shown in Figure 3.1 (b).

The measurement setup and the sample characterization are described in section 3.3. In addition, more details in each experiment are explained later in chapter 4, 5 and 6.
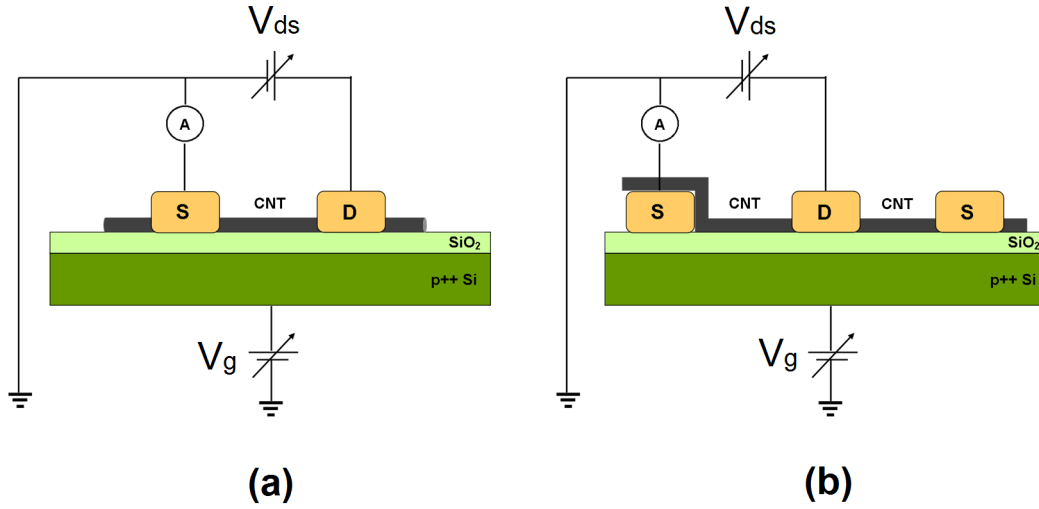
Figure 3.1: (a) Symmetrically-contacted SWNT-FET device fabricated with conventional contact feature. (b) Asymmetrically-contacted SWNT-FET device showing 2 sections consisting of symmetric and asymmetric contacts on the same CNT.

3.1 Fabrication of conventional CNT-FET devices

3.1.1 Substrate

A big piece of highly p-doped single crystal silicon wafer was chosen to be a substrate in this experiment. It is a single-side polished wafer and the thickness is 500 μm. The wafer was initially cut into smaller pieces for being conveniently brought inside the oven in cleanroom. Before loading into the furnace, tiny silicon wafers were completely cleaned with acetone and isopropanol (IPA). The temperature inside the oven was then set at 1100 °C and silicon wafers were kept in the oxidization process under oxygen flow for $\sim$ 5 hours in order to achieve the silicon dioxide (SiO_2) layer of approximately 300 nm thick. After the oxidation, the wafers were pre-cut by silicon saw into 5 mm $\times$ 5 mm size from the back side with a half-way-through distance before getting separated by simply breaking them apart.

In addition, a single-side polished silicon wafer with thermally grown SiO_2 of $\sim$ 500 nm thick was obtained from VTT Technical Research Center of Finland. It is also a highly p-doped single crystal silicon wafer similar to the one which was made in cleanroom.

The ellipsometer in cleanroom was used to measure the oxide thickness of all oxidized wafers after being processed in furnace.

### 3.1.2 Marker structure and electron beam (e-beam) patterning

Commercial MicroChem positive e-beam resists were used as transparent masks for e-beam lithographical process. A double layer of resists was employed to perform an undercut profile during the e-beam exposure which would be helpful for the lift-off process after metal deposition. A first resist layer was a polymethylmethacrylate with a molecular weight of 495 u dissolved 3% weight in anisole (495 PMMA A3) and it was coated by a spinner at the spinning speed of 3000 round per minute (rpm) to obtain ∼ 100 nm thick resist layer. A second resist layer of 2% weight PMMA with a molecular weight of 950 u dissolved in anisole (950 PMMA A2) was then spun on top of the first layer at the speed of 6000 rpm to obtain ∼ 30 nm thick layer resist. At each step before and after spinning, the sample was baked on a hot plate with ∼ 150 °C for 3 min to evaporate the solvent and humidity as well as to solidify the resists.

The first e-beam lithography process was carried out to obtain outer electrodes and inner electrodes with markers. There were 28 bonding pads linked with 28 outer electrodes to the central area where there also were 28 inner electrodes and 6×6 marker matrix (see Figure 3.2). The whole area of the marker grid was 35 μm $\times$ 35 μm and each marker which had a size of ∼ 100 nm wide was designed in different shapes and spaced away to each other by 7 μm. The Raith e_LiNE electron beam writer together with ELPHY Quantum Version 4.0 software was thus employed to expose these patterns with 20 kV of acceleration voltage and 220 μC/cm^2 of exposure dosage. The entire pattern was exposed with 500 μm write field size. Basically, the outer area was exposed with 120 μm aperture size whereas the inner area and markers were done with 30 μm aperture. However, the working area was an adjustable parameter according to one's purposes.

The exposed sample was thus developed in a developer I containing 2:1 isopropanol (IPA) : methylisobutylketone (MIBK) solution for 45 sec and followed by rinsing the sample with plain IPA and then blowing with nitrogen (N$_2$) stream. This process merely removed the exposed areas of an upper layer of a double resist mask. In order to remove the lower resist layer, sample was immersed into a developer II containing 2:1 methanol : methoxyethanol for 5 sec to wipe out the lower exposed-resist layer. At this step, the undercut feature was obtained.

3.1.3 Metal deposition and lift-off

The metal deposition was done with an ultra-high vacuum evaporator (UHV) in which the pressure can be as low as ∼ 10^{-9} mbar, providing a perfectly clean environment. A thin titanium (Ti) layer of ∼ 5 nm think was first deposited onto the sample with
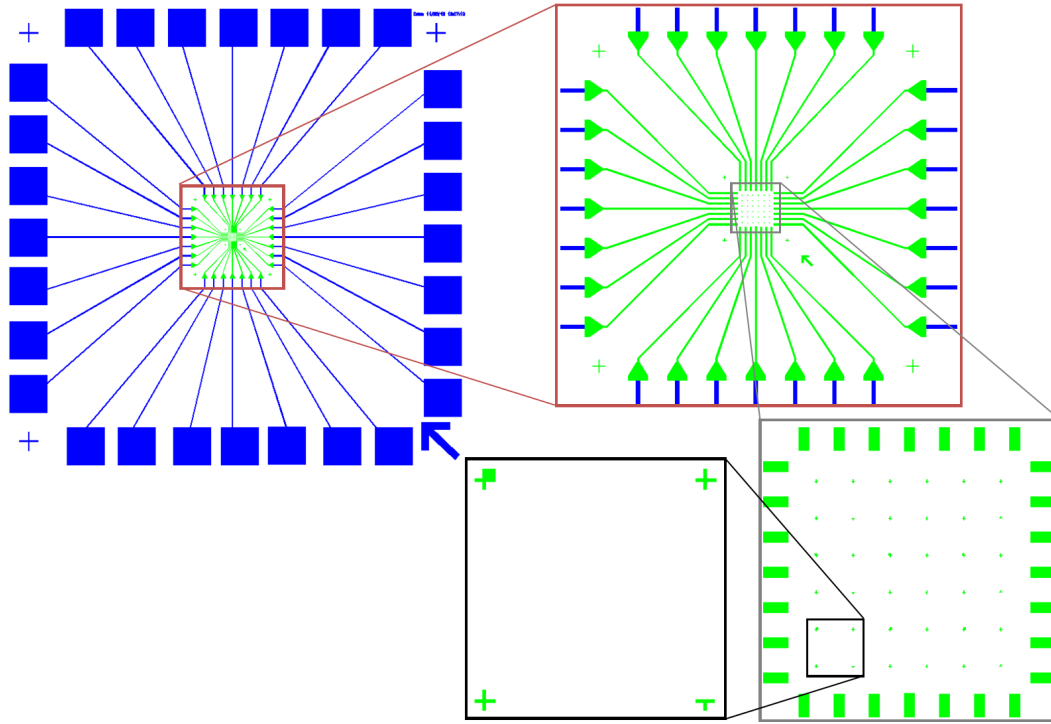
Figure 3.2: There are basically 28 outer electrodes (blue lines) linking the 28 bonding pads (blue squares) to the 28 inner electrodes (green lines). At the central area of a chip, there are totally 6 × 6 marker matrices designed with different features to help the alignment for CNTs and contact electrodes as much accurate as possible. The last zoomed-in image shows an example of 4 markers with different shapes.

the deposition rate of ~ 5 Å/s. A ~ 20 nm thickness of gold (Au) was then evaporated on top of Ti metal with a deposition rate of ~ 7 Å/s. Therefore, the total thickness of outer electrodes, inner electrodes and alignment markers was ~ 25 nm. A layer of Ti film was used here as an adhesive layer to strengthen the attachment of Au metal on SiO_2 surface. Since the contact electrode to CNTs which would be performed later in the second exposure and metallization process was aimed to be Au, it should also be used for the rest of electrodes in order to minimize any extra resistance caused by different metals. In addition, Au has been well-known as a noble metal having good chemical resistive properties to liquid environment and with a work function relatively close to palladium (Pd) which can also yield ohmic contacts with CNTs [40].

The lift-off procedure was done in hot acetone to remove unnecessary metal and PMMA residue but left only the metal which was deposited onto the substrate. The sample was then cleaned with IPA and was ready for the CNT deposition process.
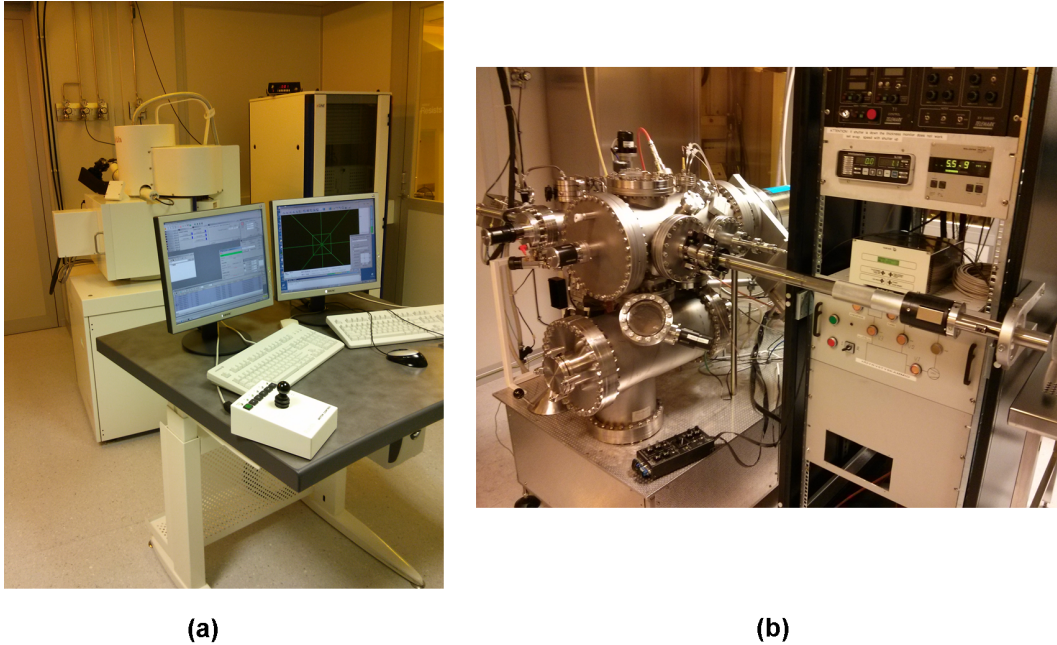
Figure 3.3: The e-beam writer (a) and UHV evaporator (b) stationed in cleanroom.

3.1.4   CNT deposition

Commercial NANOCYL-NC1100 series single-walled carbon nanotubes with an average diameter of ~ 2 nm [41] were used as a conducting channel for all devices. These tubes were bought in powder form and they were produced by the catalytic carbon vapor deposition (CCVD) method. The suspension was prepared by dissolving SWNT powder in 1,2 dichloroethane and softly sonicated for ~ 15 min before depositing onto samples. A few droplets of the nanotube solution were randomly spread onto a 5 mm $\times$ 5 mm chip while spinning at the speed of 1500 rpm. Since this method was quite uncontrollable, the number of CNTs and their positions were basically varied for each sample. A cleaning process with acetone and IPA was needed to get rid of undesired residues left over from the deposition.

3.1.5   CNT mapping and contact electrode designing

The atomic force microscope (AFM), model Digital Instruments Veeco Nanoscope, was used for searching the suitable tubes, with respect to diameter and length, and locating their positions. The 10 μm $\times$ 10 μm sized images having 4 alignment markers included were taken with tapping mode (see Figure 3.4 (b)). For all chosen tubes, the zoomed-in images were captured in order to accurately measure their diameters. The analysis of AFM images was executed by software Nanoscope version 7.30 which

was able to measure many parameters and also export various file types as ordinary pictures. The tube diameter was basically obtained by measuring the height profile of CNTs at different sections and then averaging these values (see Figure 3.4 (c)). However, this conventional AFM cannot determine the chirality of CNTs due to the limitation on its resolution. In addition to mapping CNTs with AFM, the scanning electron microscope (SEM) is possible to be employed but the deposition of amorphous carbon to the CNTs during SEM imaging [42] needs to be taken into consideration.

The exported AFM images as bitmap file were transferred to the Raith ELPHY Quantum software and 4 markers thus needed to be aligned appropriately with the overlay pattern. We first searched all promising CNTs (straight and small diameter) on which one could possibly put at least 2 electrodes ($\sim$ 100-150 nm wide) at their both ends. The contact electrode structures connecting to CNTs were then designed and the number of selected tubes was expected to be as much as possible for each chip (see Figure 3.5). By getting guided from initially fabricated markers, the design was more precise and provided almost 100% successful results in making contacts to CNTs after the second exposure and metallization.
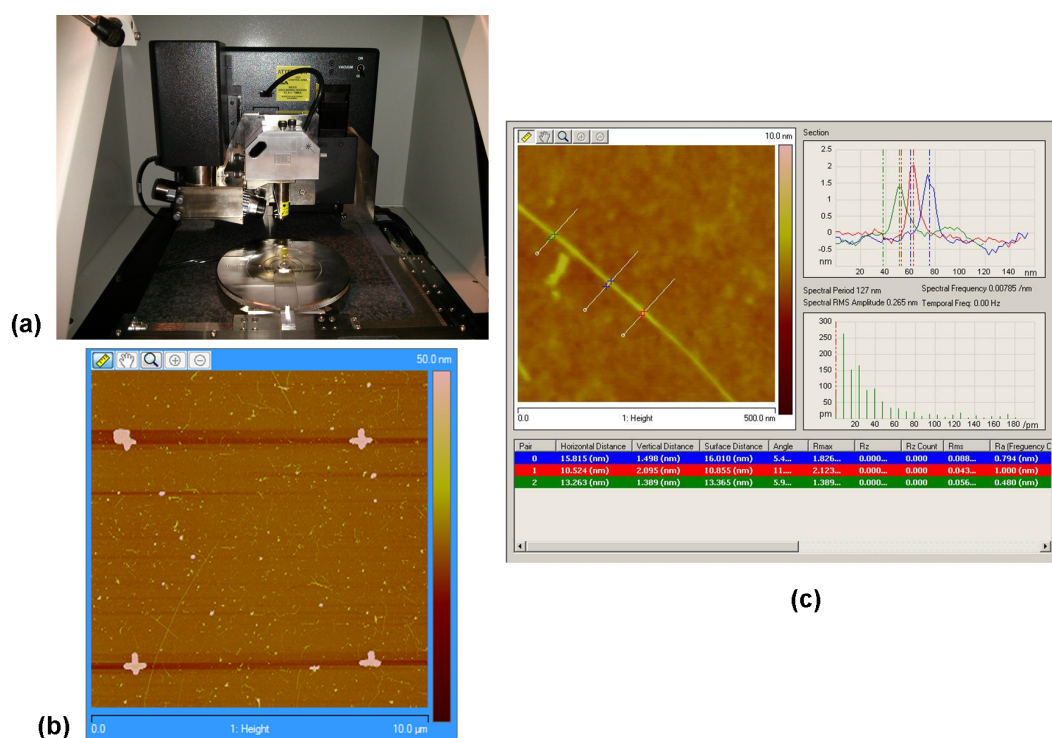
Figure 3.4: (a) The atomic force microscope (AFM) used for seeking CNTs and measuring their diameters. (b) Showing four markers and CNTs lying within 10 μm $\times$ 10 μm area. (c) Demonstrating a zoomed-in image of a SWNT while being measured its diameter.
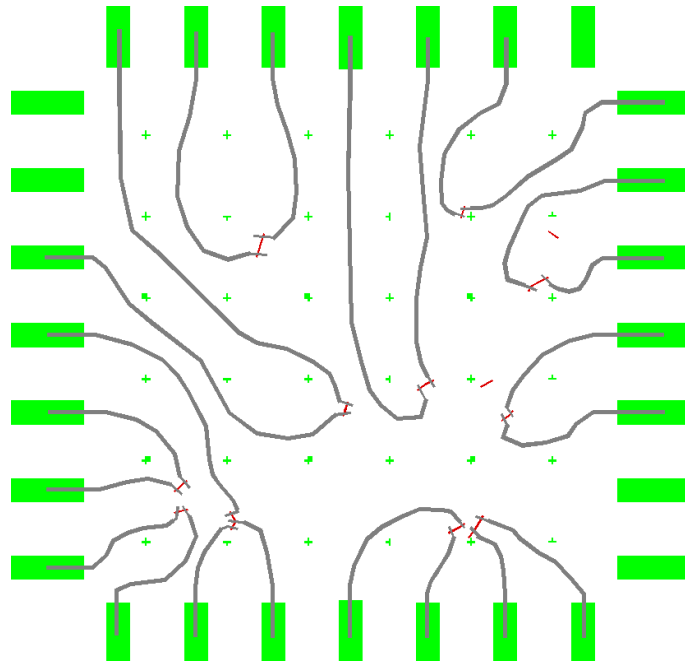
Figure 3.5: The design of CNTs and contact electrodes by e_LiNE software. Each red feature represents one CNT and grey lines are electrodes, supposing to be exposed and made as contacts.

3.1.6 Contact patterning, metal evaporation and sample pro-filing

This exposure step was done for bridging the metal electrodes to CNTs. The same recipe for PMMA coating and e-beam lithography was followed as described previously but just the smaller write filed size of 100 μm was replaced in order to enhance the accuracy of the exposure. The procedure for development and metallization was still the same as done previously but only thin Au layer of $\sim$ 20 nm was evaporated directly to CNTs. There was no Ti layer in between. The lift-off was then done and the sample was ultimately cleaned with acetone and IPA. All devices (CNT-FETs) were investigated with the optical microscope to quickly look at the overall result and with the AFM to measure the diameter and channel length (see Figure 3.6).

All as-fabricated devices were inspected by AFM not only to measure the device structures but also to confirm that the fabrication process was successfully carried out.
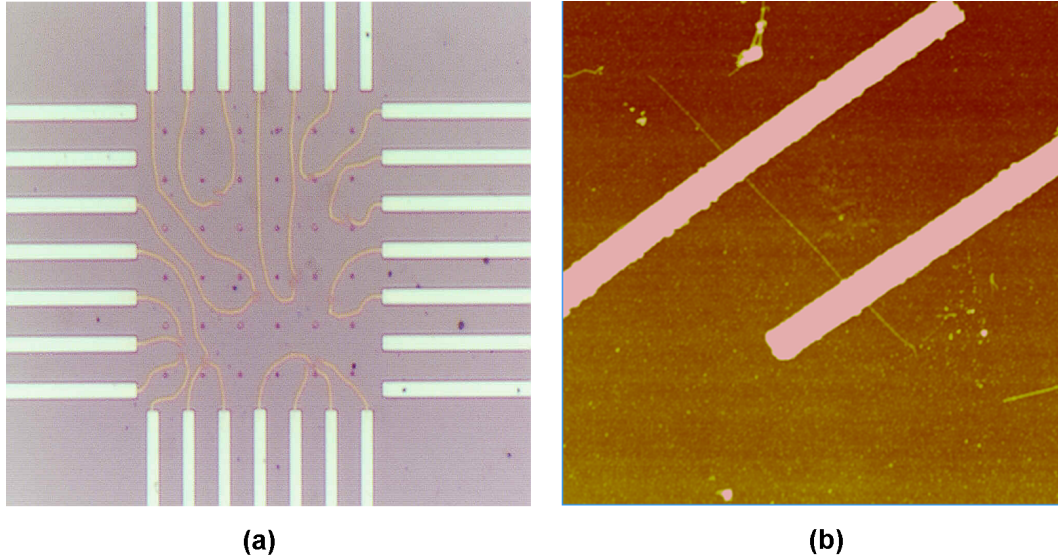
Figure 3.6: (a) The as-fabricated sample taken by an optical microscope displaying the Au contacts bridging from inner electrodes to CNTs. But unfortunately, CNTs cannot be visible with this resolution. (b) AFM image showing a typical device having source and drain electrodes on top of CNT. The whole image size is 3 μm x 3 μm.

3.1.7   Sample bonding

For the I-V measurement purpose, the chip was glued with varnish to a chip carrier which has the same amount of bonding pads (28 pads) as the sample that we fabricated (see Figure 3.7 (a)). These pads are made up of Au metal. This chip carrier is suitable for 28-pin square socket which was already mounted in the measurement setup (see Figure 3.7 (b)). Each pad on a chip carrier was connected to each electrode on the sample with aluminum wire by the operation via bonder machine. However, two bonding pads were connected to the wafer at 2 different edges and causing the substrate to be intentionally used as a global back gate. The reason why 2 wires were made for back gates is to ensure and check that the back gate is working properly.

3.2   Fabrication of CNT-FETs with asymmetric contact configuration

The fabrication process was followed almost similarly to the method described above. The only difference is that when the first e-beam lithography was carried out, there were not only outer electrodes, inner electrodes and alignment markers but also four small electrodes patterned at the central area where the marker grid was constructed (see Figure 3.9). These 4 extra electrodes were aimed to be acting as contact electrodes

(a) **(b)**
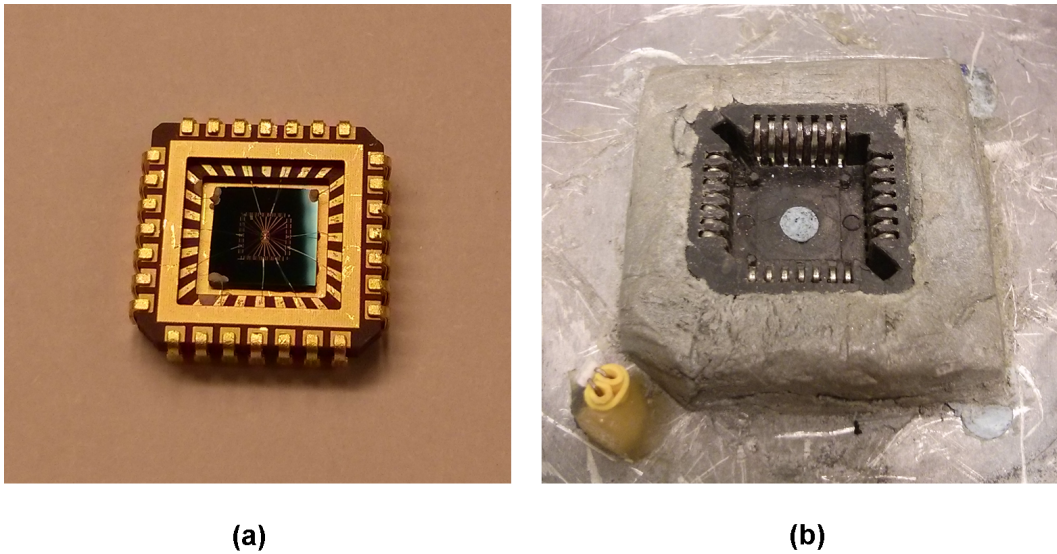
Figure 3.7: (a) A 28-pin chip carrier having an as-made sample attached. There are a few aluminum wires bonded inwards the sample. The silver paste at three corners for a global back gate and bonding wires are visible in the picture. (b) A 28-pin socket permanently embedded in the measurement box.

lying under CNTs and the CNT deposition was done with the same technique. Since we were focusing on the asymmetric contact structure of CNT-FET devices, only CNTs which were crossing above those pre-patterned contact electrodes were particularly mapped by AFM (see Figure 3.10). The design of normal contact electrodes was done by e_LiNE ELPHY Quantum v.4.0 software and then followed with the e-beam writer for the second exposure (see Figure 3.11 (a)). The metal deposition was made out later on in UHV evaporator. A practical asymmetric device can be seen in Figure 3.11 (b). In addition to different contact features, we were also interested to study different metal contacts for such asymmetric devices. Thus, Au and Pd were chosen to be explored and compared.

3.3   Characterization techniques

3.3.1   Atomic Force Microscopy (AFM)

The CNT diameter, length and channel length as well as the mapping of CNT locations were characterized by AFM. In addition to those, the imaging of CNTs as before exposure and after exposure to protein molecules was practically done by AFM in order to see the difference on CNT morphologies. All the analysis was executed by Nanoscope software version 7.30.
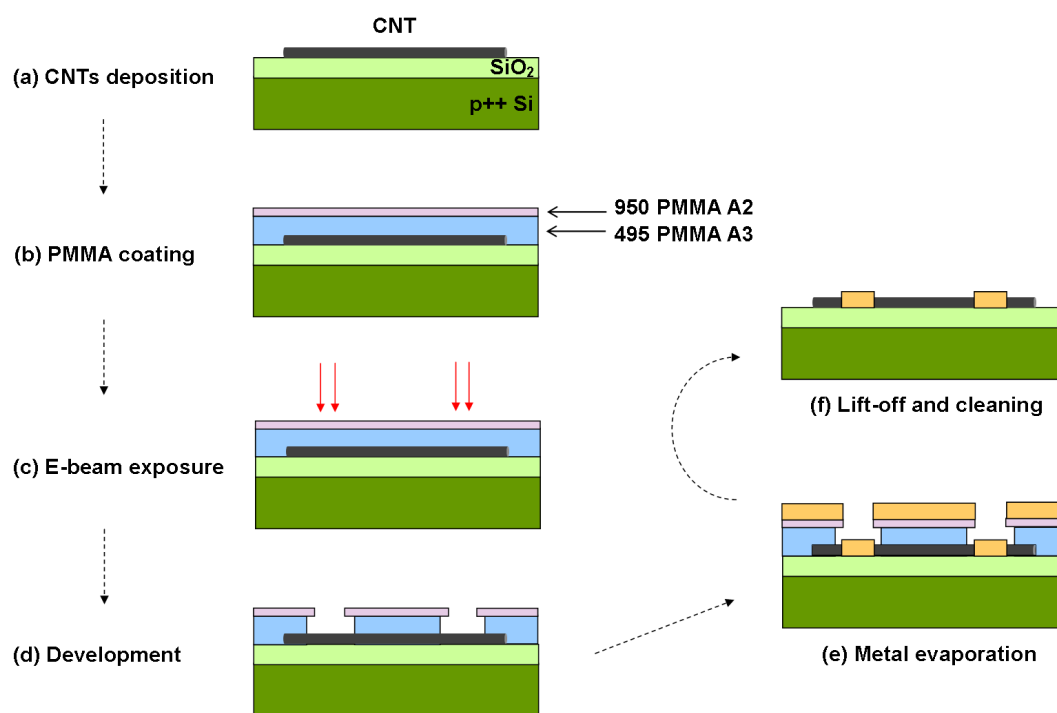
Figure 3.8: A step-by-step diagram presenting the whole fabrication process of conventional CNT-FETs having electrodes on top of CNTs.

The operation was performed in non-contact mode (tapping mode). The tip is of silicon material which has a spring constant of 40 N/m, resonant frequency of 300 kHz, tip height of 14 μm and radius $<$ 10 nm.

3.3.2 TEM - protein/CNT imaging

To visualize the CNT side wall with the attachment of protein molecules, transmission electron microscope (TEM) is one of the best tools to do this task. Therefore TEM, model JEOL JEM-1400, was employed to characterize the suspended CNTs crossing the slit on silicon nitride membrane. The different conditions such as before exposure and after exposure to proteins were carried out by TEM. Anyhow, we used gold nanoparticles (AuNPs) for labeling the proteins which adsorbed onto CNTs and also to make sure that proteins truly attached to CNTs.
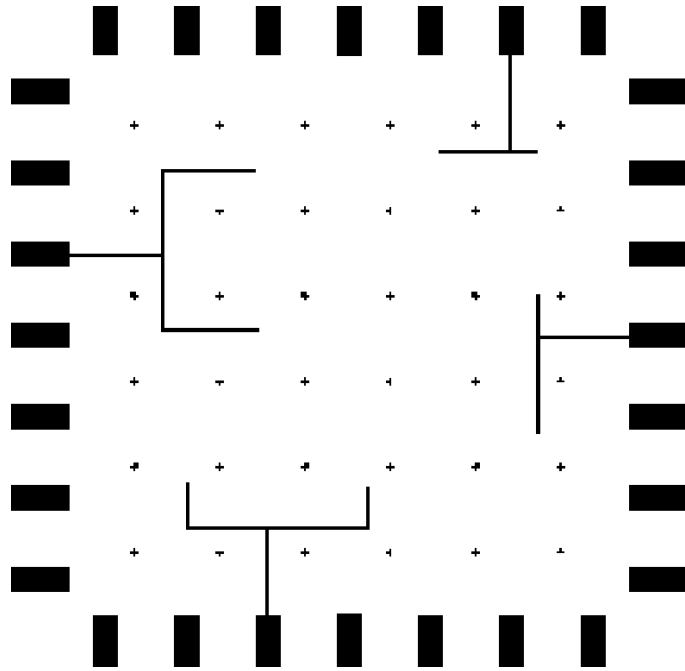
Figure 3.9: A design of the first exposure step displaying 28 inner electrodes, 6 × 6 marker matrix and 4 contact electrodes.

3.3.3 I-V measurement at room temperature

The I-V characteristics of CNT-FETs were measured with two-terminal probe technique. Two Yokogawa voltage sources used to supply source-drain voltage (V_{ds}) and gate voltage (V_g) were controlled via the LabView program. The digital commands were sent through optical fibers to national instrument (NI) chassis (NI PXI-1031) equipped with NI PXI-8336 MXI-4, NI PXI-GPIB and NI PXI-6281 M Series data acquisition (DAQ) cards. The PXI-8336 MXI-4 DAQ is linked directly to optical fibers and the PXI-6281 M Series DAQ (18-bit AI and 16-bit AO) is connected to NI BNC-2110 device for collecting the data. The PXI-GPIB DAQ has 2 GPIB cables connected in series to two Yokogawa voltage sources. Each DC voltage signal (both V_{ds} and V_g) was split into 2 paths, one to sample while another one to NI BNC-2110 device for reading the voltage data that was applied. Since the drain current (I_d) through a CNT was relatively small, the signal was brought into a low noise current preamplifier (DL Instruments Model 1211) to amplify the current up to the measurable range. The current signal was basically converted into voltage signal as an output data from a current preamplifier with several adjustable sensitivities such as 10^{-6} A/V, 10^{-7} A/V and 10^{-8} A/V which were the most often used in this experiment. The voltage signal obtaining from current preamplifier was then led to NI BNC-2110 box and read by the NI PXI-6281 M Series DAQ, finally to a computer. A LabView software was also utilized to collect and display the measured information. All the data recorded was

(a)   **(b)**
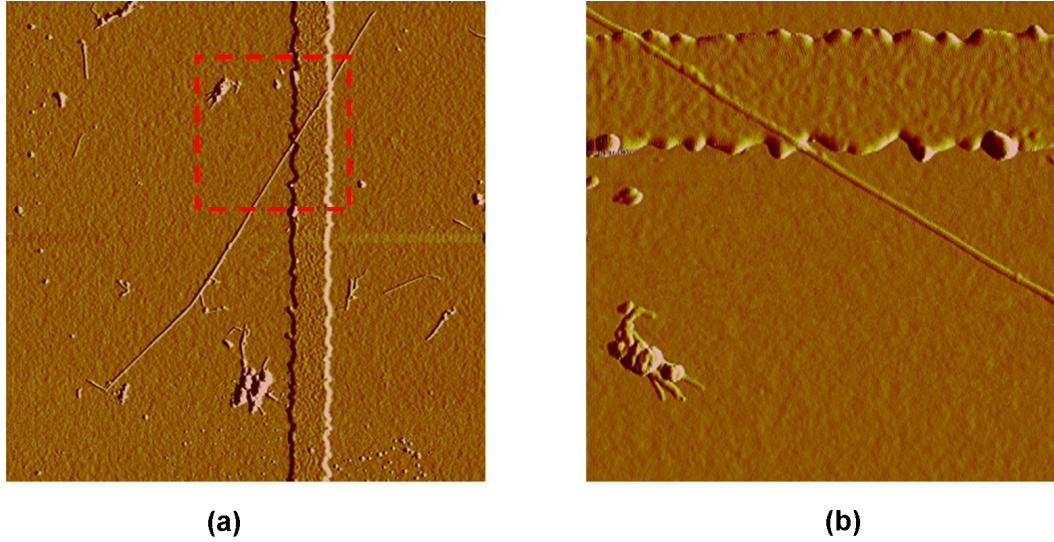
Figure 3.10: (a) AFM image showing CNT lying above pre-patterned contact electrode. The image size is 4 μm $\times$ 4 μm. (b) A zoomed-in image of the same tube across the electrode (red dashed square) captured with the size of 1.3 μm $\times$ 1.3 μm.

plotted and analyzed with Origin and Matlab software. The equivalent diagram of the whole measurement setup is shown in Figure 3.12.

For the I-V_{ds} measurement, the V_{ds} was usually applied in the ohmic regime (linear I-V response) from -50 mV to ... +50 mV in order to measure the tube resistance. The gate potential must be kept fixed, but at any interesting values, while measuring the I-V_{ds}.

For the I-V_g measurement, the gate bias (V_g) was swept from negative value to positive value for a few loops while V_{ds} was kept constant, most often at 10 mV depending on the CNT resistance. The back-gate sweeping range was basically adjusted proportionally to the oxide (dielectric layer) thickness.

For the time dependence (I-Time) measurement, both V_{ds} and V_g were kept fixed at certain values and the current signal (I_d) was continuously measured for the time period of interest. When the experiment was finished, both V_{ds} and V_g were slowly set back to zero.

We note here that the minimum resistance at ON-state of CNTs with 2 leads connected is basically $\sim$ 10 kΩ for short tubes (ballistic channels) [9], but the total resistances of two wires connecting from the electronic equipment to the measurement box and then to CNT are approximately order of tens Ohms (still small at low temperature). Therefore the wire resistance is obviously negligible when compared to CNT-FET resistance and does not influence the electrical measurements. Hence, the 2-probe technique is chosen for all experiments. The 4-wire measurement technique does not work well
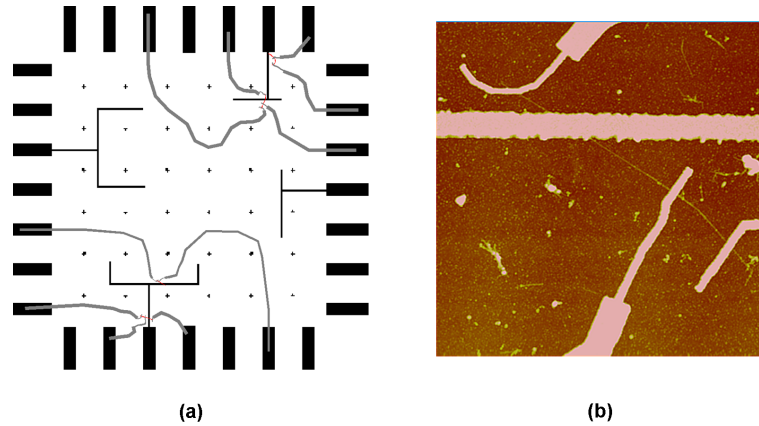
Figure 3.11: (a) Showing a lithographical design of asymmetric contact FETs for the second exposure. Only CNTs which lay over the pre-patterned contacts are selected. CNTs and normal contact electrodes are represented by red and grey colors, respectively. (b) A typical as-fabricated device consisting of 1 symmetrically-contacted and 2 asymmetrically-contacted CNT-FETs. The image size is 4 μm $\times$ 4 μm.

with 1D material since it separates the tube into sections and affects the electronic transport properties where the 1D-object/metal contacts exist [43], particularly in our case - CNT/metal contacts. Moreover, there is an extra voltage difference induction occurring with 4-probe setup as well as the analysis is relatively complicated [44].

3.3.4 Low temperature measurement setup

A home-made dip stick was employed for vacuum/oxygen sensing and low temperature experiments. A 28-pin socket was attached at the end of the dip stick as well as the silicon diode temperature sensor (Lakeshore) was placed nearby a socket to monitor the sample temperature. All wires were electrically soldered to the other end of the dip stick where there were many BNC connector heads for the I-V and temperature measurements. After mounting the as-fabricated sample, the section at the end of dip stick was enclosed with a metallic cylindrically-shaped can. An indium wire was then put in between, acting as an O-ring, before two metallic c-shape clamps were used to seal the chamber tightly. The setup was pumped to have a vacuum in order to remove the water and moisture surrounding inside the dip stick that might affect the samples. All pumps were turned off completely when the pressure of ~ 0.01 mbar was achieved. The ready dip stick was thus inserted into the liquid helium (L-He) dewar and by adjusting the distance of dip stick in L-He tank (relative to L-He level), the temperatures of CNT-FET samples at certain values were obtainable. This technique allowed the measurements being operated at the temperature range starting from nearly room temperature (~ 300 K) to liquid helium temperature (4.2 K). A little amount of helium gas was definitely needed to exchange the heat between liquid

helium and sample in order to have the sample temperature reach 4.2 K. The I-V$_{ds}$ and I-V$_{ds}$ measurements were, however, performed as similarly as explained in section 3.3.3 at different temperatures. Besides, the experiments on sensitivity of CNTs to vacuum condition (0.01 mbar) and to oxygen gas (ambient) were carried out before the cooling process started.

We also note here that the total resistances of two wires in the cryostat are ~ 900 Ω (~ 450 Ω for each) but it is still much smaller than the CNT resistances at ON-state. Therefore, it can be considered as an insignificant factor and does not disturb the I-V measurements. The two-probe measurement technique is also used in the cryogenic experiments.
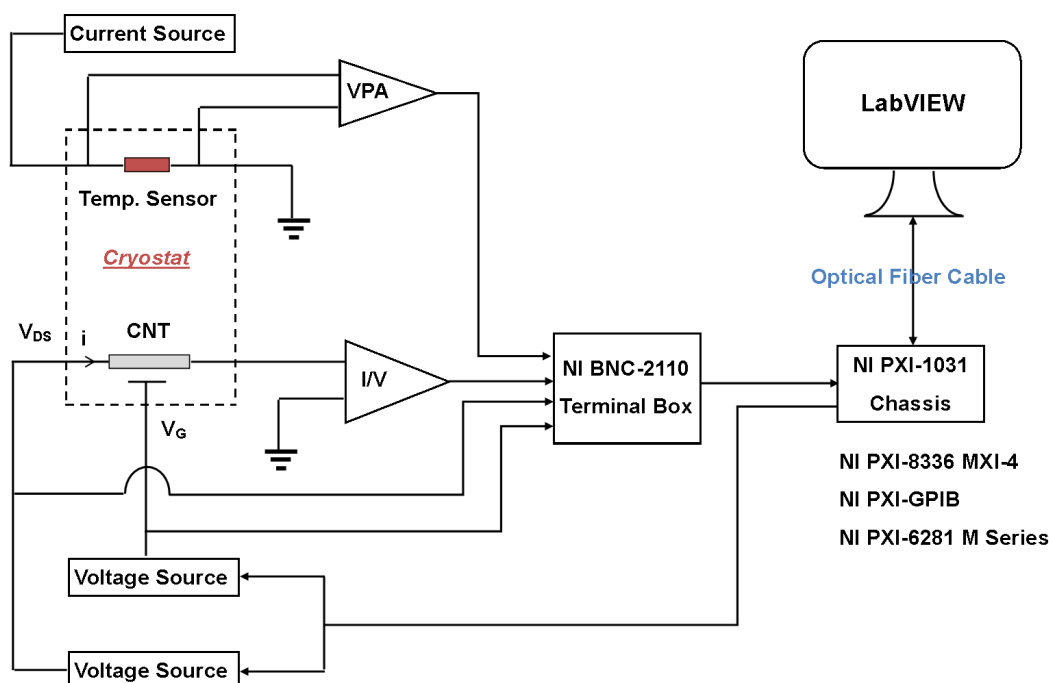
Figure 3.12: A simplified schematic of entire I-V measurement setup including the cryogenic system. All input signals for reading data and output commands for applying source-drain voltage (V$_{ds}$) and gate voltage (V$_g$) are communicated to electronic equipment via LabView software. The data recorded are processed by other programs i.e. Origin and MatLab. In this sketch, VPA and I/V stand for a voltage preamplifier and a current preamplifier, respectively.

4 Li doping of carbon nanotube field-effect transistors

4.1 Background on alkali metal - CNT complexes

There are several means to fabricate FET devices with individual and long CNTs as a conducting channel. A typical technique is to grow CNTs with catalytic chemical vapor deposition (CCVD) procedure which can yield individual nanotubes as long as about centimeters [8]. However, there are other possibilities to obtain individual CNTs without having samples been through the catalyst preparation and thermal process. One simply needs to disperse a CNT powder into some organic (polar aprotic) solvents for instance 1,2 dichloroethane (DCE), dimethyl sulfoxide (DMSO) and dimethylformamide (DMF) [21]. But there are, of course, some disadvantages with this CNT/solution preparation as already mentioned in Chapter 2.1.4. Briefly, this kind of mixture is not practically stable as CNTs tend to combine and stay in a bundle form due to the attractive Van der Waals forces among nanotubes in solution [45]. Thus this method requires powerful sonication for certain time to separate a bunch of nanotubes which leads to cutting CNTs into smaller pieces and creating unexpected defects on nanotube sidewalls [22,23]. After sonication stops for a short time, each CNT starts to aggregate and sediment as a black powder again. Once the solution is needed again, sonication is also again required and then the damage on CNTs continues. In an additional strategy, different types of surfactants can be mixed with CNTs to improve on the dispersibility. These surfactants, for instance protein molecules [27,46], DNA [20] and chemical molecules [47–50], can adsorb non-covalently onto nanotube sidewalls and make CNTs soluble. In addition to CNT functionalization, the use of some chemicals can chemically modify the carbon nanotube lattice structure and covalently bond to the tube walls, but affect the electronic properties of CNTs [51,52]. Although the functionalization with covalent and non-covalent bonds yields better dissolution, the suspension is still considered as a metastable dispersion [26].

Therefore an attempt for mildly separating the bundled CNTs without any use of sonication, surfactants and/or functionalization had been carried out by Penicaud et al. [26]. This technique utilizes the redox reaction by intercalating alkali metals in between CNT bundles to balance the Van der Waals forces (CNTs) and the Coulomb repulsive forces (alkali metals). The intercalation results in reduced CNTs and allows them to form polyelectrolyte salts (alkali-CNT salt compounds) which spontaneously

dissolve in polar aprotic solvents and remain thermodynamically stable. This method, however, has to be processed in a humidity- and oxygen-free environment because alkali metals will oxidize in normal ambient condition [26,45]. Moreover, the challenging development on SWNT separation, purification and dissolution without any help of ultra-centrifugation and sonication has been recently achieved by Shaffer et al. [53]. They have demonstrated that the treatment of SWNTs in a mixture of sodium metal and liquid ammonia (liquid sodium metal ammonia solution) can yield an excellent sodium/nanotube-anion salt which spontaneously dissolves in a polar aprotic organic solvent (i.e. dry DMF). This method perfectly results in individualized, purified and undamaged SWNTs.

The motivation of this work

In the work done previously, the driving motivation for having CNTs in redox reaction with alkali metal intercalation lies in the radically improved solubility. However, it is also a process of chemical doping which definitely is expected to influence the electronic properties of semiconducting CNTs. Even though the alkali doping in gas-phase on CNT-FETs has been carried out by evaporating alkali metals in vacuum chamber [54,55], in the liquid phase on individual CNTs it has not so far been characterized. A major goal of this study is to perform this lacking experiment. The effects of alkali salt doping on the electronic transport properties of individual CNT-FET devices are studied in different conditions, including before/after exposure, during exposure, and reversibility. Thus, unlike in the previous works, the processing of the CNT-FET devices are done by conventional methods and the alkali solution is applied solely for doping purposes. However, for completeness, the dispersion of CNTs reduced with alkali salt is performed as part of a CNT-FET fabrication process, and the electrical transport of these is measured.

The experiments in overview

The key issue in exploring the efficient dissolution and effective doping is the Li-complex solution which is basically a compound of lithium, naphthalene and tetrahydrofuran (THF). The Li atom is known to be a very good reducing agent (in other words, easily to be oxidized) to donate electrons in redox chemical reactions and finally acting as cation whereas naphthalene in this case is an oxidizing agent by receiving electrons and finally becoming an anion. Lithium cations in solution are basically coordinated by THF and paired with naphthalene anions, leading to a complex-structured formation which is chemically stabilized by polar THF [26,56]. Due to the complexity and tediousness of the lithium solubilization, a good part of the experimental work

has been dedicated to that, which is explained in section 4.2. Section 4.3 describes the doping and measurement procedures, while section 4.4 describes and discusses the results of the main measurements.

The measurements described in section 4.4 are:

• Doping of SWNT-FET with Li. Gate dependent conduction measured before and after the doping process. Different complementary control measurements also performed (4.4.1).

• The gate dependent conduction measured during the doping process and recording the time dependence (4.4.2).

• Gate dependent conduction measured of SWNT-FET devices that have been processed via the alkali solubilization method of CNTs. This measurement does not include intentional doping. The lithium is not present anymore when the devices are measured (4.5).

4.2   Experimental details: Preparation of Li solution

Humidity- and oxygen-free environment

Since alkali metals are easily oxidized, an efficient glove box system has been chosen for the study of the alkali-CNT salts, to keep away oxygen and humidity. It is a model PL-4GB-2400 Dual Module made by Innovative Technology Co.. There are two parts connected and four gloves equipped which make the use of it convenient. The gas purification system is able to keep the oxygen (O_2) and humidity (H_2O) level lower than 1 ppm and can maintain the pressure and gas circulation with various inert gases, for example nitrogen, helium and argon. The glove box has a slight overpressure, which decreases the amount of normal air outside leaking in, and is equipped with analyzers to monitor O_2 and H_2O levels. In our case, the entire experiments are performed under an argon-flowed atmosphere. To avoid the oxygen and humidity as well as other undesired gases coming inside the glove box while transferring any materials in and out, two different sizes of chambers together with a rough pump are then needed to purify all stuff in vacuum before opening and loading into the glove box. A glove box involved in this alkali liquid-phase experiment is shown in Figure 4.1.

Preparation of active Li-compound solution
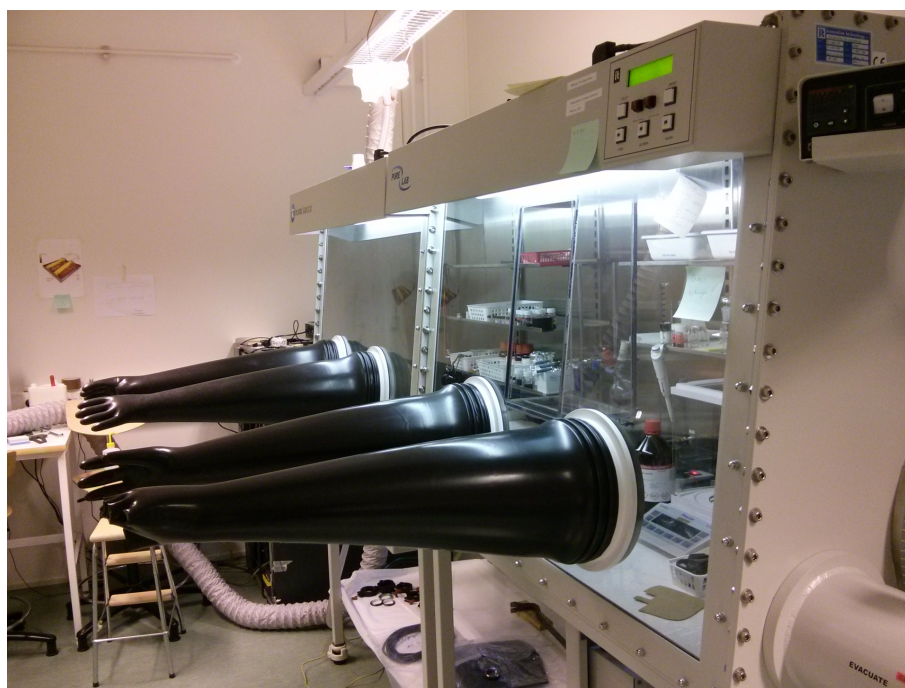
Figure 4.1: Dual Module glove box made by Innovative Technology Inc. having argon gas filled. The equipped gas purifier system can efficiently maintain the entire flow of the box, so that the oxygen and humidity level inside can be basically kept lower than 1 ppm.

Naphthalene was stored under vacuum environment in a flask to keep it dry before using in the next step. Pure THF was obtained by refluxing a mixture of sodium, benzophenone, and THF under nitrogen atmosphere for one hour. The vaporized THF was condensed in a condenser column, and then 30 ml of dry and clean THF was taken out by syringe and mixed into a flask containing 400 mg of dry naphthalene. Lithium (Li) wire was cut into tiny pieces (within mineral oil) for 35 mg in total weight and was cleaned in petroleum ether before adding quickly to the naphthalene-THF mixture. At this step, the solution is, however, not chemically active, which means that the alkali-salt compound (Li/naphthalene/THF) does not form yet. To obtain an active alkali-complex salt solution, thermal energy must be provided to supply the activation energy, where the chemical reaction starts. Therefore, a mixture of those was refluxed at temperature 60-70 °C for approximately half an hour. Finally, the active alkali compound was transferred via small metal tube into Rotaflo flask (filled with argon and sealed with rubber septum/paraffin film) with the pressure gradient technique to avoid the leaking air, and immediately loaded into argon-flowed glove box.

Nuclear magnetic resonance (NMR) spectroscopy was employed to characterize and confirm that an alkali-salt solution prepared was active and contained the Li/naphthalene/THF complex molecules.

## 4.3 Experimental details: The procedure for Li doping and measurement

The electrical transport measurements were carried out both in ambient condition and in glove box. Individual SWNT-FET devices (fabricated as explained in chapter 3.1) were utilized to study the effect of Li-salt compound on their electronic properties. Since many components are involved in the solution that brings the Li atom to the CNT and since the solubilized Li is extremely vulnerable to water, several different control measurements were undertaken in the investigation.

4.3.1 The basic Li-doping experiment

The idea of the fundamental doping experiment is schematically shown in Figure 4.2. First, the transport properties of individual SWNT-FET devices were characterized in ambient air (a). The devices were then brought into glove box and left overnight in argon atmosphere (b). The electrical transport properties of all devices were again measured (b). Before exposure to active Li-salt compound, a home-made glass chamber was softly mounted on top of the samples to ease the control of handling with solution. An active Li-complex salt ($\sim$ 100 mM) was then fed into chamber and FET devices were exposed for 15 min (c). After the doping process was done, dry THF was flowed into chamber to flush out the Li-salt solution, after which the chamber was taken off and samples were dried with argon stream. The electrical transport properties were then characterized once again in argon environment (d). After all experiments required inert atmosphere had been done, the chip was brought outside the glove box and cleaned with 5% HCl for 10 min, followed with distilled water (90°C) for 20 min and rinsed with IPA, then dried with nitrogen stream. The last I-V characterizations were achieved in ambient condition (a).

Complementary reference level control experiments

To make sure that the Li carrying THF/naphthalene compound does not itself dope the CNT, we performed control experiments for reference. A few Individual SWNT-FET devices were brought into glove box and kept overnight before being further proceeded. The electrical transport characteristics were first measured in argon atmosphere and the flow chamber was mounted. A 100 mM mixture of THF and naphthalene was then fed into the chamber and the FET devices were exposed for 15 min. A chip was afterwards rinsed with plain THF, and dried with argon stream. Finally, the electrical transport measurements were carried out once again in argon environment.
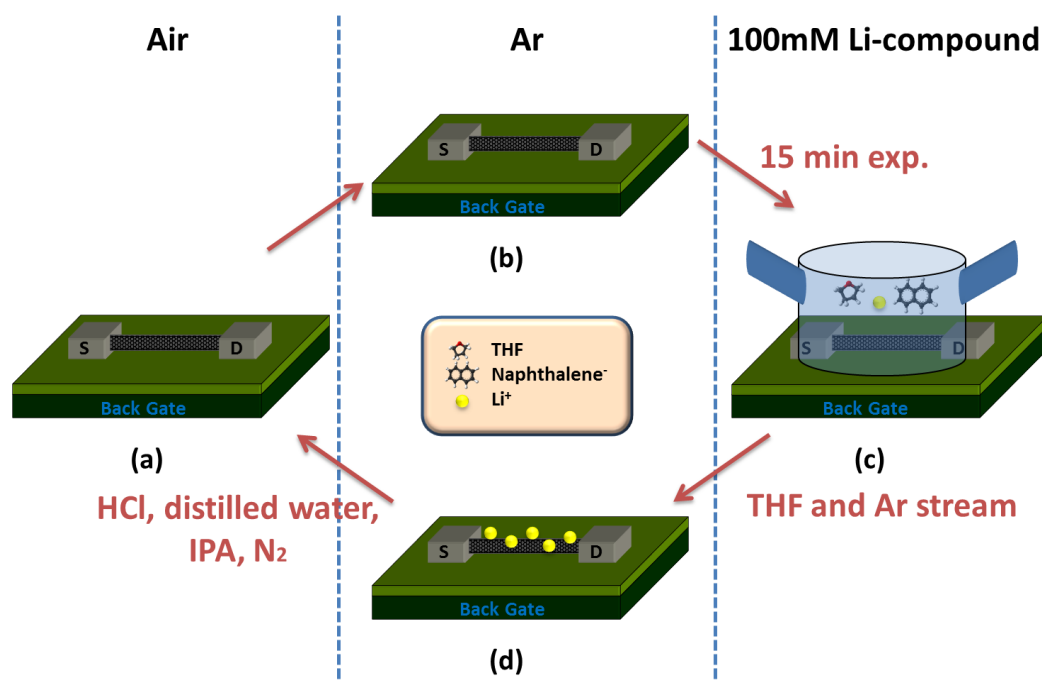
Figure 4.2: Scheme illustrating all the processing steps of Li-doping and reversibility experiments on CNT-FETs.

The reference characterization procedure is shown in Figure 4.3.
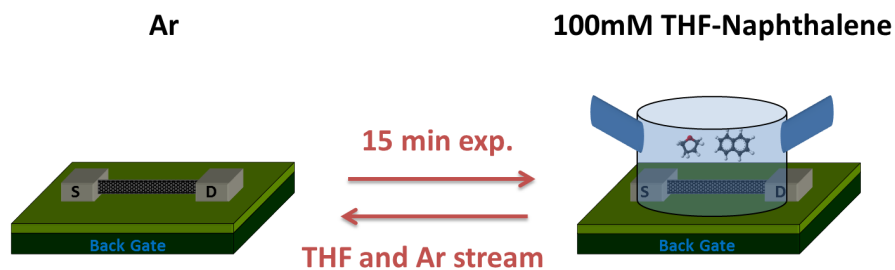
Figure 4.3: Displaying a method for investigating THF-naphthalene solution onto CNTs as a reference measurement.

4.3.2 Time dependence measurements in Li-doping

A device was initially characterized in ambient environment and then brought inside glove box. After being kept overnight in argon atmosphere, the electrical transport was measured and a chamber was gently placed on top of a device. A mixture of THF and naphthalene ($\sim$ 100 mM) was fed into chamber and the I-V measurements were performed. At this step, we fixed the gate voltage (V_g) to maintain the device in the

ON-state. Then an active Li-complex salt (~ 100 μM) was slowly injected into the chamber. The lithium doping dependence of the source-drain current in real-time was monitored for a certain period of time. The entire scenario of the real-time detection of Li atoms can be seen in Figure 4.4.
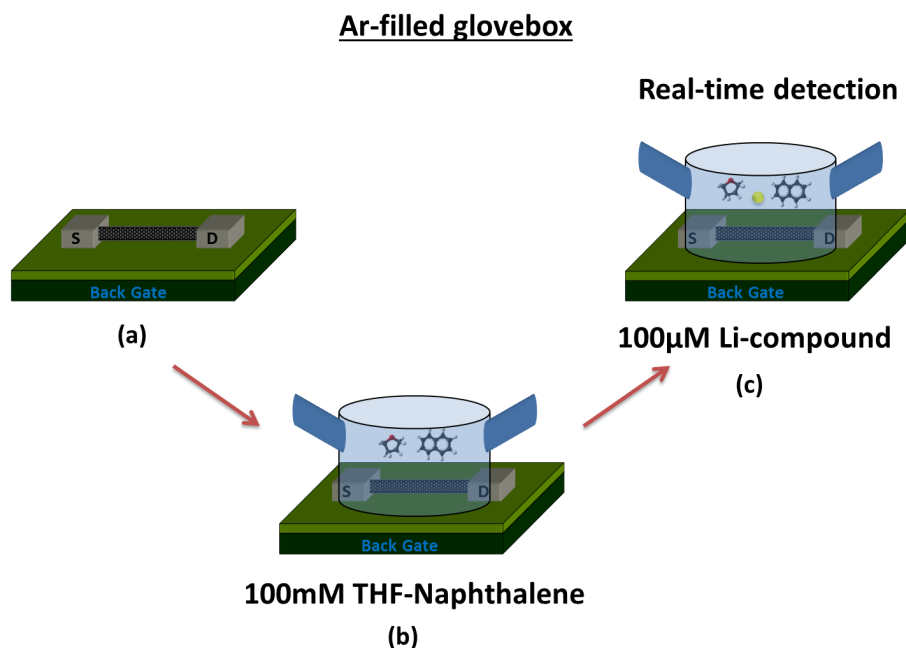
Figure 4.4: The diagram showing the transfer characteristic measurements in each step before the real-time sensing of Li atoms can be started. This experiment is carried out mainly in glove box in order to avoid the contaminations from oxygen and humidity.

4.4 Electrical measurements of Li doping

In this section I describe the results of our measurements on the effects of Li-doping on CNTs. Key data on the devices measured are summarized in Table 4.1 at the end of this Chapter.

4.4.1 The electrical transport of SWNT-FETs upon Li-doping

Reference level measurements

As described in section 4.3.1, we performed for reference the direct characterization of
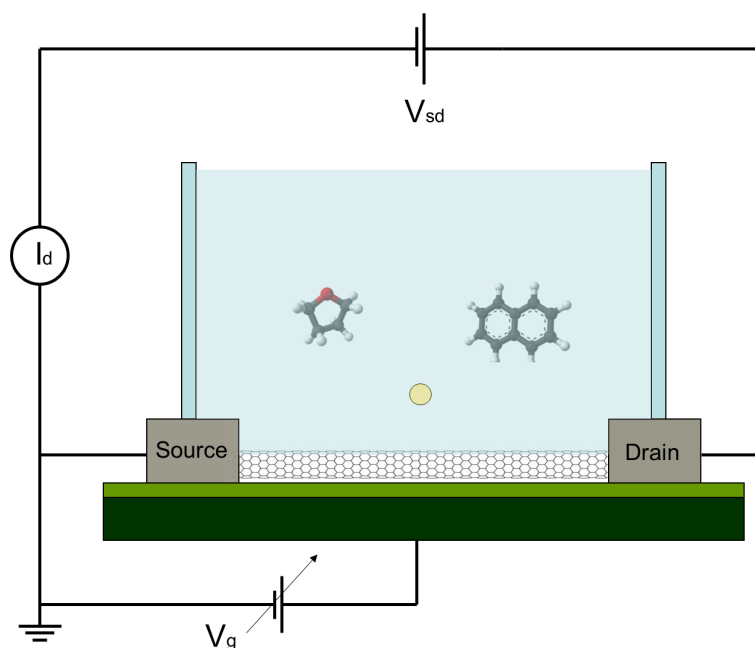
Figure 4.5: The electrical measurement setup of CNT-FETs having lithium, naphthalene and THF mixed inside chamber. The source-drain voltage (V_{ds}) is usually applied at 10 mV while the gate voltage (V_g) is continuously swept in few loops from positive to negative values.

gate responses on SWNT-FETs as before and after exposure to a 100 mM mixture of THF-naphthalene (without Li added) in order to make sure that this compound does not actually influence the electronic properties in such a way of changing semiconducting behaviors from p-type to n-type. The source-drain bias (V_{ds}) of 10 mV was applied and the gate potential (V_g) was being swept in several loops from positive to negative values. The results measured in argon atmosphere (see Figure 4.6) obviously indicate the absence of doping of CNT by THF-naphthalene compound as we can clearly see that its electrical transport behavior remains p-type with exactly the same ON/OFF ratio as well as the sub-threshold slope value. The gate response of the reference device after being exposed (grey trace in Figure 4.6), however, displays a threshold voltage (V_{th}) shift towards the left side of sweeping gate voltage (negative V_g value) which implies that the exposure by this solution merely influences the charging on the SiO_2 surface and thus resulting in a local screening of the electric field on CNTs. This disturbance possibly occurs from the residual grime when THF-naphthalene solution is blown drying.

The charge transfer of SWNT-FETs after Li doping

The effect of Li intercalation onto CNTs was studied by measuring the gate transfer
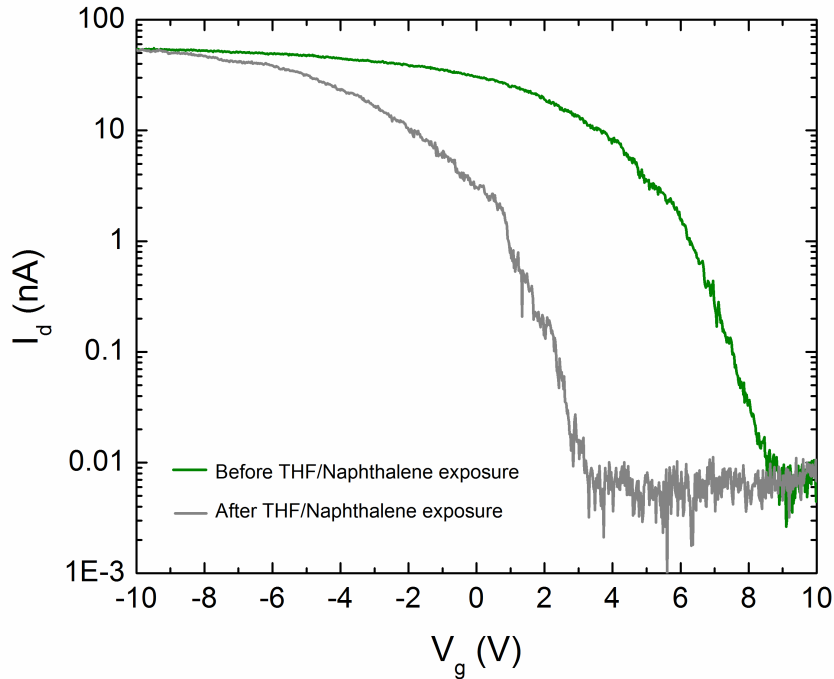
Figure 4.6: A reference investigation concerning the doping effect of THF-naphthalene solution on CNTs. The doping result by this compound obviously cannot be observed.

characteristics (I-V_g) of FET devices, such that electronic properties can be directly observed. Before FET devices were exposed to active solution, they show a p-type semiconducting behavior (blue trace in Figure 4.7), as normally observed in CNTs having high work function (W) contacts [9]. In contrast, the gate transfer after devices being exposed to Li-complex solution behaves oppositely, as its electronic behavior changes from p-type to n-type (orange trace in Figure 4.7). This implies that the charge carriers are switched from holes (p-type) to electrons (n-type) as a result of redox interaction between complex molecules and CNTs, thus contributing to a change in nanotube energy band configuration.

Once Li-complex molecules begin to interact with CNTs, naphthalene anions directly react and provide their excessive electrons to CNTs while Li^+ and THF are surrounding the negatively charged nanotubes [56, 57]. After the exposure is finished and the system is completely dried out by N_2 stream, Li atoms are however still surrounding the CNTs and form a polyelectrolyte salt $Li(THF)C_{10}$ [26]. This chemical mechanism results in a disturbance in energy band structure of semiconducting CNTs by shifting the Fermi level (E_F) towards the conduction band (E_C), and thus modifying the electronic properties to become n-type semiconductor [54, 55, 58]. The major charge injection occurs with electrons tunneling through modified Schottky barriers in the conduction band.

We nevertheless note here that the Li-doping mechanism on CNTs is not perfectly controllable, in such a way that their electronic behavior is equally but oppositely maintained as prior to exposure. As observed in our study, the on-state current (I_{ON}) of p-type (before exposure) CNTs is not necessarily equal to I_{ON} of n-type CNTs (after exposure) as well as the off-state current (I_{OFF}) of both p-type and n-type CNTs has not remained at the same level. Some devices even show ambipolar characteristics after the exposure. It is very difficult to have I_{ON} and I_{OFF} after exposure as exactly the same value as before exposure.
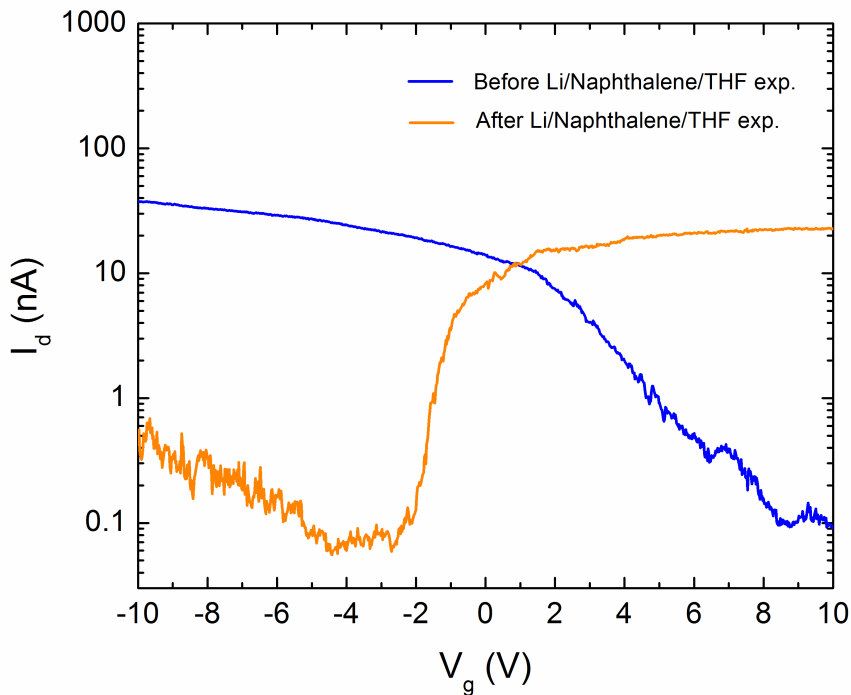
Figure 4.7: The gate transfer measurement of p-type CNT as before exposure to Li-complex solution is displayed as blue line whereas the measurement of the same tube after exposure is shown as orange curve. The n-type characteristic (orange trace) is clearly observed. The source-drain voltage (V_{ds}) is kept constant at 10 mV during the gate scanning.

Reversibility

We performed the experimental series in which CNT-FETs were treated in different conditions, and the gate transfer characteristics were monitored in each stage. Here we mainly explore the consequence on electronic properties of Li-doped CNTs after cleaning with a suitable procedure (as mentioned above), to follow the reversible phenomenon of redox reaction on CNT sidewalls. As seen in Figure 4.8, I-V_g characteristics of as-fabricated FET device before exposure to active solution were measured

at room condition and it displays p-type behavior (green curve), similarly to its gate response measured in argon environment (blue curve) with having almost exactly the same I_{ON}. After being exposed to active solution, its electronic behavior converts from p-type to n-type semiconductor (orange curve) but with having relatively different I_{ON} and I_{OFF} level compared to prior gate responses (green and blue traces). We again point out that the doping reaction process is not absolutely complete as already explained in previous section. This n-type behavior is stable under argon atmosphere but as soon as a Li-intercalated CNT-FET is exposed to air, CNT is oxidized back to neutral state and Li is reduced to form Li_2O. When CNT has been processed through properly cleaning steps to get rid of Li_2O residues, the gate transfer measurement changes back to p-type (black curve) with however having Ion observed to be somewhat smaller than initial p-type I-V_g characteristics. This reduction of on-state current is most likely as a result of the left-over residues on the nanotube sidewalls, and thus leading to the creation of defects and/or scattering sites along CNT. In addition, the rinsing procedure requires the use of hydrochloric acid (HCl) which might also affect the nanotube and/or CNT-metal contact interfaces. We find that the reversibility on electronic properties of CNTs to be doped and un-doped with Li-complex salt is possible to achieve but the device contact resistances are usually observed to be increasing after doping and cleaning. We also discover that the doping cycle is repeatable.
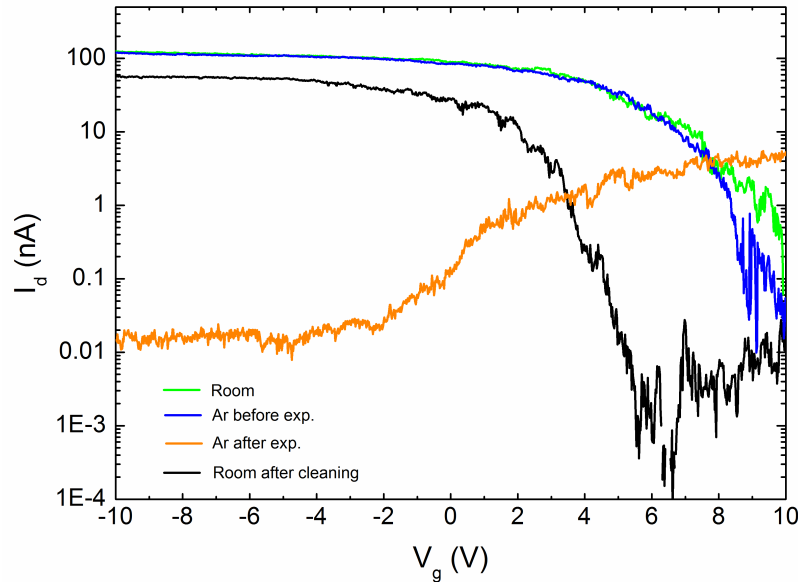
**Figure 4.8**: The I-V_g characteristics of an individual SWNT-FET device measured as pristine at room condition (green), as before exposure to Li-complex salt under argon environment (blue), as after exposure to Li-complex salt under argon environment (orange), and finally as after cleaning at room condition (black).

4.4.2   Time dependence of Li-doping

We first performed the electronic transport characterizations of individually pristine SWNT-FETs under argon atmosphere. Many of them exhibit p-type behavior with different on-state currents (I_{ON}) owing to a variety of tube diameters and CNT/metal contact resistances, whereas some of them act with metallic properties. Among their transfer characteristics, a semiconducting CNT device displaying the best gate response (high ON/OFF drain current ratio (I_{ON}/I_{OFF})) was chosen to perform further in the rest of the whole steps. A home-made chamber was softly mounted onto a silicon chip and a fresh mixture of naphthalene and THF ($\sim$ 100 mM) was then fed through the samples. After a while to let a device get saturated with a mixture, a constant V_{ds} of 10 mV was applied and we started to sweep the back-gate potential. The inset of Figure 4.9 shows an I-V_g result measured in a solution, indicating the ambipolar characteristics where the transport charge carriers can be both electrons (n-type) at positive gate voltage and holes (p-type) at negative gate voltage. Since the active solution is electrically conducting as it is polyelectrolyte, we thus need to dilute its concentration down to a non-conducting range. In our study a concentration of $\sim$ 100 μM was tested with two Au electrodes with the spacing $\sim$ 1 μm gap (average channel length of measured FET devices), giving an average resistance of $\sim$ 10 GΩ which is comparable to the off-state resistance of a single CNT-FET device. The real-time detection of Li atoms ultimately started by having the device set at on-state conduction (V_{ds} = 10 mV and V_g = -5 V) until the drain current was achieved steadily for $\sim$ 15 min, in this moment the electrical transport is dominated by holes as the Fermi energy level (E_F) locates close to a valence energy band (E_V). A 100 μM Li-complex salt was then slowly flowed into the chamber at a moment of $\sim$ 18th min (dashed line in Figure 4.9). Once the Li-complex molecules interact to CNT, a sudden drop in drain current is observed and continued to decrease nonlinearly until reaching the off-state conduction. The electrical transport has apparently changed from p-type to n-type as the CNT has been chemically doped by Li atoms, implying that the Fermi level is altered and shifted closer to conduction energy band (E_C), in which the primary charge carriers are electrons. The conversion in electronic properties from on-state to off-state conduction takes about 20 min and the time dependent measurement was terminated after off-state drain current had been monitored further for $\sim$ 10 min.

As observed in both liquid-phase doping and real time sensing measurements, drain current at on-state conduction switches back to off-state conduction at the same source-drain bias and (negative) gate potential which implies that holes (carriers for p-type) are no longer governing the transport but electrons (carriers for n-type). We believe that the electronic properties of individual p-type SWNT-FETs electrically convert to n-type CNT transistors as a consequence of Fermi level relocation by the influence of Li atoms doped onto CNT sidewalls. In addition, the Schottky barriers at CNT/metal interfaces are possibly modified in accordance with Fermi level shift,

as the charge injection by tunneling through the barriers (directly contribute to drain current) is found to be different after exposure to Li-salt compound. This can be simply explained by Landauer-B´uttiker formula as previously expressed in equation 2.11 [31]. Here in our time dependent measurement of liquid-phase Li-doping both V_{ds} and V_g are kept steady during the sensing period, initially yielding a constant drain current at on-state condition. Thus the only variable parameter that can make equation (2.11) exist at off-state conduction ($I_d \ll 1$) while all parameters e.g. V_{ds}, V_g, and *T(E)* are constants is the Fermi level, as it can be electrically delocalized and settled down close to conduction band due to extra negative charges given by Li atoms. This relocation of E_F results in the electrical modification of CNT energy band, and then the conversion from on-state current of p-type (hole carriers) to off-state current of n-type (electron carriers) at the same fixed V_{ds} and V_g, as evidently seen in Figures 4.7, 4.8 and 4.9.
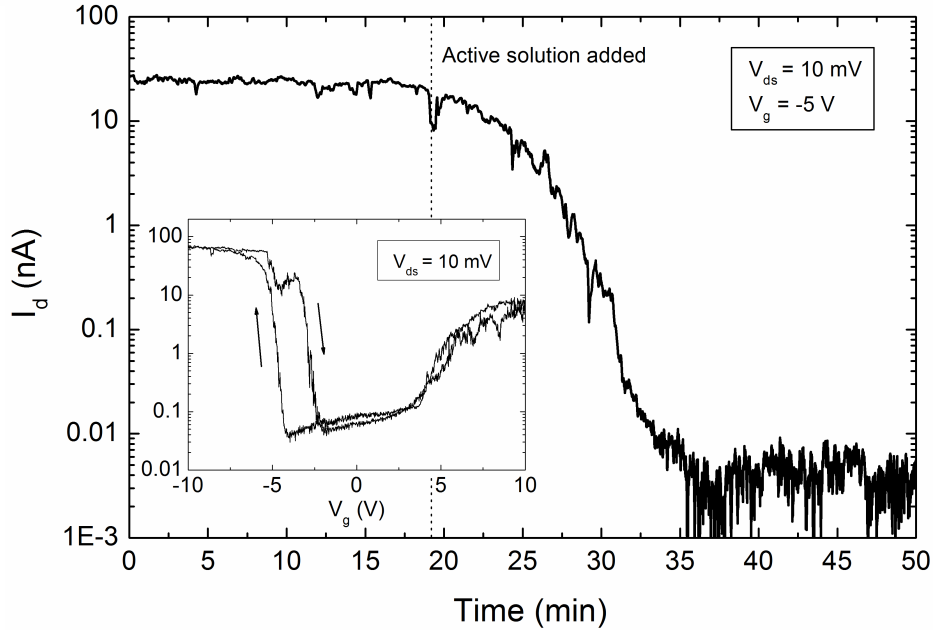
Figure 4.9: The drain current response monitored in real time during exposure to 100 μM active Li-complex solution at fixed constant of both source-drain and gate voltages, initially set at device on-state conduction. The doping events begin almost immediately after an active solution is introduced into chamber (dashed line) and take about 20 min to finish when reached the off-state conduction. Inset shows the gate transfer characteristics measured in 100 mM naphthalene/THF mixture.

Interestingly, this study can most likely lead to a single alkali sensing application where the drain current response might appear with step-like discrete reduction when individual alkali atoms interact to CNT sidewalls. In order to observe those single events, the CNT-FET devices indeed require a relatively short channel and small nanotube diameter to have as little amount of carbon atoms as possible otherwise the electrical detection would show a continuous change, as observed in Figure 4.9.

Besides, it has been already found that the chemical reaction between CNTs and Li cations conjugated by naphthalene anions is consequently finished with LiC_{10} compound formula [26]. By knowing the CNT diameter and device channel length together with using a carbon-carbon distance (in the tubular honeycomb lattice) of 1.42 Åand the Li-C atomic ratio (1:10), we therefore are able to approximate ideally the number of Li cations involved in entire doping process [58].

4.5   Electrical measurements of Li-dissolved CNTs

A powder of 18 mg CVD-grown CNT raw material (NanoCyl Inc.) was dissolved in an active Li-salt compound inside glove box and left on a shaking table for overnight. The mixture was then filtered out the Li-intercalated CNT material by PTFE membrane filter (0.45 μm pore size) and entirely rinsed with plain THF until a color of draining THF turned clear. The Li-treated CNTs were subsequently redissolved in dimethyl sulfoxide (DMSO) and placed on a shaking plate for overnight. The CNTs from Li-CNT suspension was deposited inside the glove box by spinning technique onto pre-patterned Si chips isolated with a 300 nm thermally grown SiO_2. The samples were afterwards taken out from the glove box and immersed in 5% HCl for 10 min, followed with distilled water at $\sim 90°$C for 20 min, then rinsed with IPA and dried with N_2 stream. From this step onwards, the conventional micro-fabrication process to achieve SWNT-FETs was completed in cleanroom by following chapter 3.1.5. Eventually, the electronic properties of CNTs dispersed by Li-treated procedure were studied in ambient environment to perform the effect of Li intercalation.

The Li-separated CNT dissolved in DMSO is successfully obtained, and the suspension is found to be very stable for at least 2 years when being stored inside argon-filled glove box. In order to emphasize the extraordinary stability of Li-treated CNT dissolution, we then prepared a fresh mixture of the same CNT raw material and DMSO, followed by dispersing for $\sim$ 15 min with shaking table. Initially before shaking, raw CNT powder (black aggregates) was obviously not dissolved in DMSO (Figure 4.10(a), right bottle). Immediately after shaking was finished, as-prepared CNT solution looked dark as similar as Li-doped CNT suspension, basically yielding a well-dispersed and stable solution (Figure 4.10(b), right bottle). The untreated CNTs however started to bundle up within approximately 30 min later, eventually sedimenting in solvent at the bottom (Figure 4.10(c-d), right bottle). A disadvantage of harsh stirring, for example ultra-sonication, should also be taken into consideration when making a nanotube suspension because this method is found to create the defects and shorten the CNTs [22, 59]. This difficulty on solubility and instability is in contrast not an issue when working with Li-intercalated CNTs because they spontaneously dissolve in several solvents, for instance DMSO, and retain thermodynamically stable quite long (in our case, more than 2 years) under argon atmosphere.
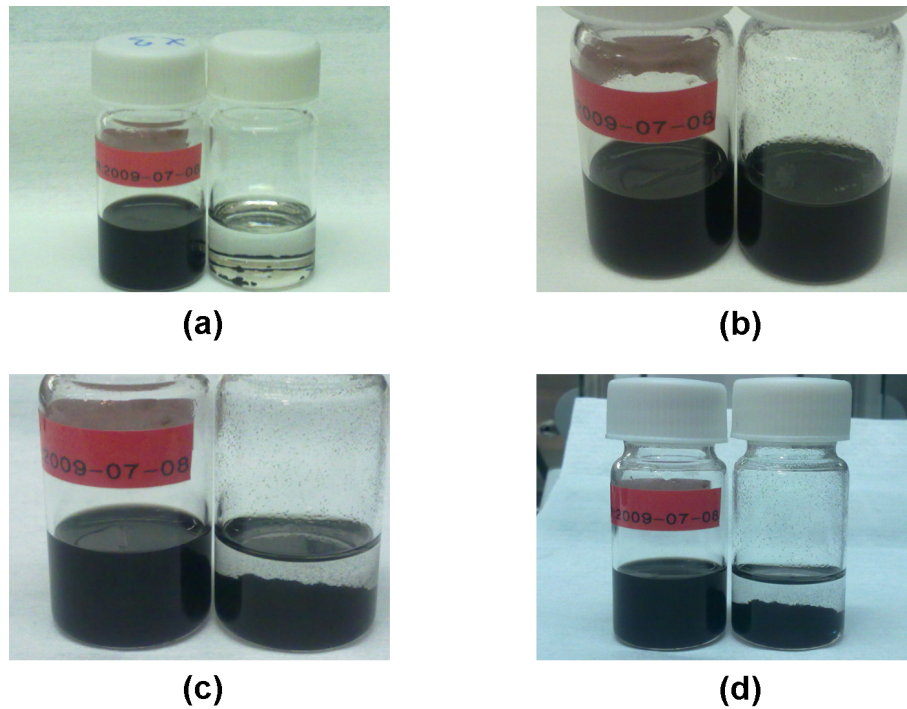
Figure 4.10: Demonstrating the solubilization and the stability of left bottle: Li-intercalated CNTs dissolved in DMSO in comparison with right bottle: the same weight of pure CNTs dispersed in DMSO as before shaking (a), after shaking immediately (b), 30 min (c) and 60 min (d). A suspension in the left bottle has been stored in glove box and retained stable for more than 2 years.

Additionally, the electronic transport measurements of individual SWNT-FETs fabricated with Li-treated nanotubes were carried out at room condition. The electrical characterization was performed by scanning the back-gate potential while having source-drain voltage fixed at $V_{ds} = 10$ mV. The gate transfer measurement (Figure 4.11) reveals that the electronic transport of CNT-FET device remains evidently p-type behavior with Au contacts, even though this nanotube had been through a chemical doping process. A few FET samples tested with Li-treated CNTs show similar results as normal FET devices fabricated with pristine CNTs dispersed in dichloroethane together with the help of ultra-sonication. These results also point out that a simple cleaning procedure can easily remove Li_2O, which simultaneously forms when Li-doped CNTs expose to air, away from CNTs. This all implies that the alkali intercalation method does not affect the major electronic properties of CNTs, instead enhancing the solubility and maintaining their intrinsic properties. This technique, on the other hand, can be a promising alternative for preparing CNT suspension without any use of extreme shearing.
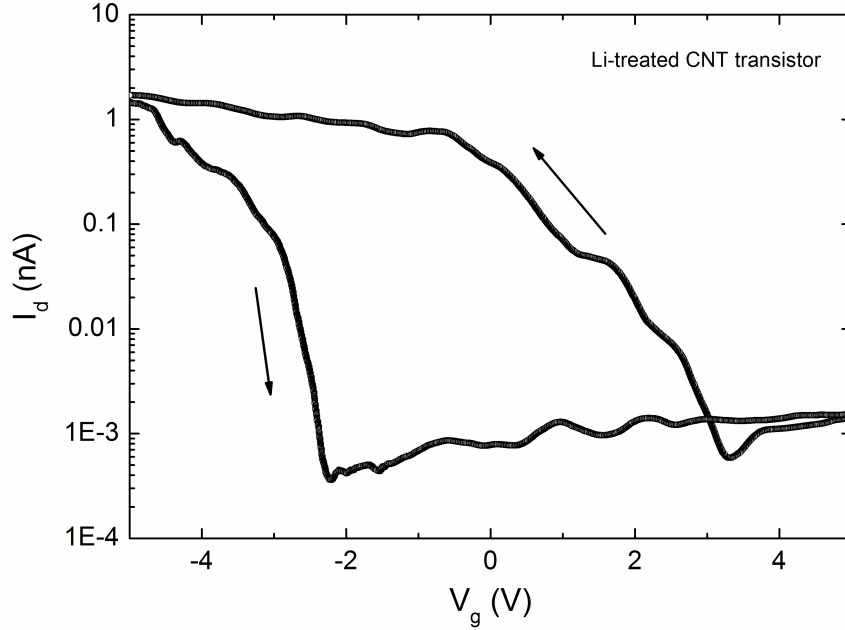
Figure 4.11: Showing the gate dependence of Li-treated CNT transistor (electrically contacted by Au) measured in ambient condition with a constant source-drain voltage, $V_{ds} = 10$ mV. The gate transfer response indicates p-type behavior as normally observed in nanotube FET devices with having Au (or Pd) contacted to pristine CNTs.

Device	Diameter (nm)	Channel length (μm)	R_{ON} p-type (before Li exp.)	R_{ON} n-type (after Li exp.)
1	2	1.05	200 kΩ	150 kΩ
2	1.8	0.42	30 kΩ	40 kΩ
3	1.9	0.82	140 kΩ	460 kΩ
4	1.5	1.00	400 kΩ	3.3 MΩ
5	2	1.34	250 kΩ	400 kΩ
6	1.8	0.62	370 kΩ	380 kΩ
7	1.9	1.79	4.5 MΩ	7.2 MΩ

Table 4.1: List of conventional (symmetric) Au-contacted CNT-FET devices measured as before and after exposure to Li-complex salt. There are totally 7 devices that their electronic properties change from p-type to n-type whereas other 4 devices (not included in the table) change from p-type to ambipolar.

5 Interaction of hydrophobin with carbon nanotubes

5.1 Background on hydrophobin proteins (HFBI) and their interaction with CNTs

Hydrophobins (HFBI) are proteins that can be found in filamentous fungi, for instance *Agaricus bisporus* (common button mushroom) [60]. Their biological properties appear to be various but mainly seem to be involved in the interfacial interactions or surface phenomena providing themselves to be flexible and useful in many applications. They have been in general categorized into two classes namely class I and class II, based on their functional properties and alignments of the protein sequences [60–62]. These two groups of hydrophobins contribute to different functionalities as the major difference is that the class I members basically form aggregates or assemblies that are relatively difficult to dissolve in aqueous solution, while class II members typically form aggregates that are readily soluble. This solubility can be used as a quick guide to classify the type of hydrophobins.

The crystallographic structures (taken by high resolution X-ray crystallography) of hydrophobins in class II members, HFBI and HFBII from *Trichoderma reesei*, have shown that the protein basis is actually a large and rigid amphiphilic molecule [63–65]. It contains both a patch that is merely comprised of aliphatic chains, functionally acting as hydrophobic domain and the hydrogen-bonding side chains, typically acting as hydrophilic domain. For class II hydrophobin, the hydrophobic patch is flat and covers approximately 19% of the whole surface area whereas the rest of the molecule surface area is essentially hydrophilic [64]. This amphiphilic basis makes hydrophobins well soluble in aqueous solution, generally performing like surfactants, besides they are able to form oligomers containing with a few discrete numbers of protein molecules, such as two or four [66]. The diameter of one hydrophobin molecule is estimated to be 2-3 nm which consists of $\sim$ 70-120 amino acid residues, and the molecular weight is 7.2 kDa [60, 66].

Hydrophobins have been explored in many aspects but the most attractive topic seems to be the surface adhesion properties. Since hydrophobins are small, amphiphilic and surface active, they can adhere to various surfaces, and thus leading to the ability of

functionalization and then solubilization [61, 66, 67]. Besides they can be utilized as adsorbed molecules or molecular layer to immobilize other functional proteins which in this case perform similarly to biosensors [68]. In addition to those interesting capabilities, one issue that cannot be ignored when talking about hydrophobins is the self-assembly at interfaces. It has been demonstrated with class II hydrophobins that oriented and well-ordered monolayer film formation can be achieved on surfaces [61]. On the other hand, the naturally occurring (wild type) HFBI has also been genetically modified by adding a Cys amino acid residue at its N terminus to become a variant, called NCysHFBI, having a single free reactive -SH group which is able to conjugate with gold nanoparticles (AuNPs). This NCysHFBI-AuNPs conjugation can be utilized not only as the labeling method to position hydrophobins but also as an applicable technique to pattern hybrid nanostructures [27, 69]. Moreover, the electronic properties of hydrophobins deposited onto graphite substrate have been explored by using conductive atomic force microscopy, and found that the electrical transport through hydrophobin monolayer is essentially owing to tunneling [70]. These striking interfacial and surface properties of hydrophobins have brought them to a variety of nanotechnological applications of biological, physical, and chemical character.

The motivation of this work

There have been of course some experiments dealing with a combination of hydrophobins and CNTs, as hydrophobins are amphiphilic and able to attach on CNTs by hydrophobic reaction. The major idea of those studies is to noncovalently functionalize CNTs with hydrophobins and then utilize them for specific applications e.g. hybrid nanostructures [27], human IgG immobilization [71], and glucose biosensor [72]. However, the electrical transport measurements on sensing hydrophobins with CNT-FET devices and the adsorption of hydrophobins on suspended CNTs still remain to be explored. Due to the importance of both hydrophobins and CNTs, this work is worth doing. ***In our experiment, we have studied the noncovalently hydrophobic interaction between CNT sidewalls and hydrophobins, and its effect on electronic transport properties of CNTs (mainly focusing on SWNTs)***. More specifically, we have used in this work genetically engineered class II hydrophobins (NCysHFBI) and have undertaken experiments to study functionalization of CNT-NCysHFBI complex with AuNPs, in addition to the electronic transport experiments.

The experiments in overview

The electrical transport measurements of CNT-FET devices upon exposure to NCysHFBI solution have been carried out largely in the same way as with the alkali doping, de-

scribed in Chapter IV. Naturally, in this case glove-box protection from the environment was not needed.

In this case, substantial effort was invested in imaging the protein and attached AuNP that had adhered to the CNT. Atomic force microscopy (AFM) as well as transmission electron microscopy (TEM) has been employed to characterize the protein adsorption on CNTs.

In this Chapter, the following steps are described:

• All experimental details on material preparation (CNT, NCysHFBI, AuNP), imaging equipment (AFM and TEM), and the measurement technique (5.2).

• Imaging of CNTs functionalized with NCysHFBI protein and NCysHFBI-AuNP complex (5.3).

• Conduction measurements on the effect of NCysHFBI adhesion to CNT. In-situ measurements were also made (5.4).

(a)   **(b)**   **(c)**
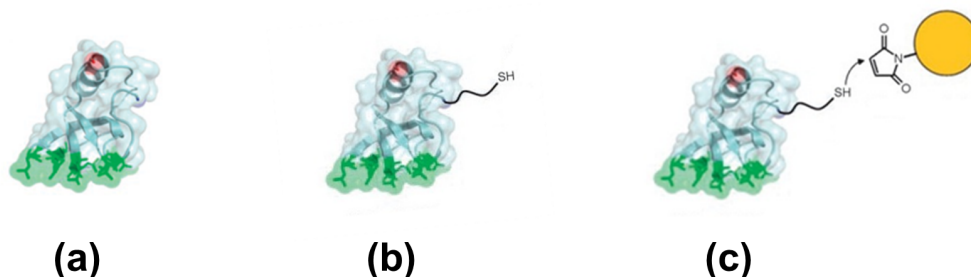
Figure 5.1: Illustrating the X-ray crystal structure of class II hydrophobins in three different stages: (a) HFBI, (b) genetically modified HFBI (NCysHFBI), and (c) NCysHFBI conjugated with mono-maleimido AuNPs. The green patch of them indicates the planar hydrophobic aliphatic domain, leaving the rest of the molecule with hydrophilic surface (light-blue color). This character makes the protein amphiphilic and very soluble. The conjugation exists with the interaction between a free reactive -SH group of NCysHFBI and a functionalized group of AuNP, specifically shown in (c). [27]

5.2 Experimental details

5.2.1 Materials

Protein solution

NCysHFBI protein powder was obtained from collaborating group at VTT Biotechnology via genetically engineering Trichoderma reesei hydrophobins HFBI with an addition of single Cys residue at the N-terminal, followed by the biological purification and the chemical extraction procedures as described in Ref. [66]. The NCysHFBI solution of 0.1 mg/ml concentration at pH7 was prepared by dissolving NCysHFBI in MilliQ water and was used for investigating the protein attachment onto CNTs lying on Si/SiO$_2$ substrate and the suspended CNTs (see below). Besides, the protein solution of 1 μg/ml ($\sim$ 100 nM) pH7 dissolved in 10 mM Na-phosphate buffer solution (NaP) was prepared for the electrical transport measurements of CNT-FET devices.

AuNP solution

Gold nanoparticles (AuNPs) were synthesized as explained in Ref. [73] with a little modification as the capped functional group to gold particles was basically changed from mercaptoundecanoic acid to mercaptosuccinic acid (MSA), yielding the MSA-functionalized AuNPs. These particles were soluble in water and had a diameter of $\sim$ 3 nm, however some bigger particles might be found due to the aggregation upon storage. For the experiment, a 5 g/l solution of MSA-AuNPs dispersed in MilliQ water was prepared and employed to make conjugation with NCysHFBI, for labelling the proteins.

SWNTs and MWNTs on Si/SiO$_2$ substrate

Commercial CVD-grown SWNTs (bought from NanoCyl S.A.) and MWNTs (obtained from NEC Corp. [74]) were dispersed in dichloroethane, followed with soft ultrasonication before use. The SWNT and MWNT suspensions were then deposited onto Si/SiO$_2$ substrates by spin-coating technique. Some of the samples were used in the experiment with protein adsorption and then characterizing with AFM (as explained later in Chapter 5.2.2) while the rest of samples were further fabricated into FET devices (as described in Chapter 3.1) for the study on protein detection (as explained later in Chapter 5.2.3).

Suspended SWNTs for TEM imaging

TEM imaging of a CNT requires a fully open view to it, which has been accomplished in this work by having SWNTs suspended above a Si$_3$N$_4$ slit membrane. The slit structure (free open window) of silicon nitride membrane (Si$_3$N$_4$) was patterned on Si/Si$_3$N$_4$ wafer, followed by the procedure described in Ref. [75]. The size of as-

fabricated slits was approximately 1-2 μm wide. Afterwards, the individual SWNTs suspended on slits were thermally grown by a chemical vapor deposition (CVD) technique as explained in Ref. [76] with the growth temperature of 850°C. These samples were used for the work on protein adsorption, and then characterizing with TEM (as explained later in Chapter 5.2.2). The labelling by AuNPs to NCysHFBI is also performed in suspended CNT samples for TEM characterization.

5.2.2 Imaging of protein and AuNP attachment on CNTs

AFM characterization

The solution of 0.1 mg/ml NCysHFBI dissolved in water was gently sonicated for 1 min before use. The SWNTs and MWNTs lying on Si/SiO$_2$ substrates were cleaned with acetone, IPA, and DI water (1 min), and then they were dipped in protein solution for 10 min. After the incubation process was finished, samples were thoroughly rinsed with DI water for 1 min to remove excessive proteins and were dried by N$_2$ stream. These hydrophobin-treated CNTs were eventually characterized by AFM. In addition, an investigation on the removal of proteins attached on CNT sidewalls was carried out by sonicating samples in acetone for 10 min and then followed by a normal cleaning process.

TEM characterization

The protein deposition on slit samples was done in various conditions. The solution of 0.1 mg/ml NCysHFBI dissolved in water was softly sonicated for 1 min before use. The suspended SWNTs were then immersed in protein solution for 45 min (CNTs + NCysHFBI). The protein-treated samples were rinsed with DI water for 1 min and dried by N$_2$ stream. Moreover, the NCysHFBI-AuNP conjugation was performed in order to label the protein adsorbed on SWNTs. The AuNP solution of 5 g/l was ultrasonicated for 10 min, then the NCysHFBI-treated SWNTs were incubated in it for 45 min followed by washing with DI water for 1 min and drying with N$_2$ stream (CNTs + NCysHFBI + AuNPs). Also, for reference purpose we immersed untreated suspended SWNTs into AuNP solution for 45 min, then cleaned with DI water for 1 min and blew by N$_2$ stream (CNTs + AuNPs). These samples were ultimately characterized by TEM.

5.2.3   Electrical measurement method

We have employed CNT devices in a normal FET configuration fabricated as described in Chapter 3.1 for all the electrical transport measurements. Au electrode of 25 nm thick was deposited onto CNTs acting as metal contacts. The electronic properties of CNT-FETs were characterized as before and after exposure to NCysHFBI protein solution. The time dependent measurement of protein sensing was also performed in this work.

The electronic measurements of all as-fabricated CNT-FET devices were first done in ambient condition at room temperature. A home-made Teflon chamber was softly mounted on top of a Si chip. A buffer solution of 10 mM NaP pH7 was gently sonicated for 1 min before injection into a flow cell. The gate transfer characterization was then performed at this stage to observe their characteristics before having protein molecules flow into the chamber. A solution of 1 μg/ml ($\sim$ 100 nM) NCysHFBI dispersed in 10 mM NaP pH7 was gently sonicated for 1 min, and then injecting it over the CNT devices. After the transport measurements in liquid conditions were finished, DI water was fed through the flow cell for 1-2 min to clean the unnecessary proteins left over on a Si chip. The flow chamber was then taken out and the Si chip was blown dry with N_2 gun. Eventually the electrical measurements were again carried out at this stage in dry condition as after exposed to NCysHFBI protein. The source-drain voltage (V_{ds}) was supplied to SWNT devices at $V_{ds} = 10$ mV and to MWNT devices at $V_{ds} = 1$ mV for the gate transfer measurements while the gate potential was scanned several loops from positive to negative values.

In addition, an experiment with recording of the time dependence of the hydrophobin sensing was performed in two ways. Firstly, by having the source-drain bias kept constant at $V_{ds} = 10$ mV (for SWNT-FETs) and at $V_{ds} = 1$ mV (for MWNT-FETs) while the gate voltage was also fixed at device ON-state conduction. The time dependence of the current was recorded. Secondly, the gate dependence (I-V_g) was recorded multiple times during immersion in HFBI solution.

5.3   Imaging of hydrophobin attachment to CNTs

5.3.1   AFM of protein adsorption

The SWNTs and MWNTs on Si/SiO$_2$ substrate processed in various conditions were imaged by atomic force microscopy (AFM) as seen in Figure 5.3. It obviously reveals that the NCysHFBI molecules actually attach to both CNT sidewalls and SiO$_2$ surface (see Figure 5.3(b)). The height profile measurements of the same SWNT at the

Real-time detection of hydrophobin protein
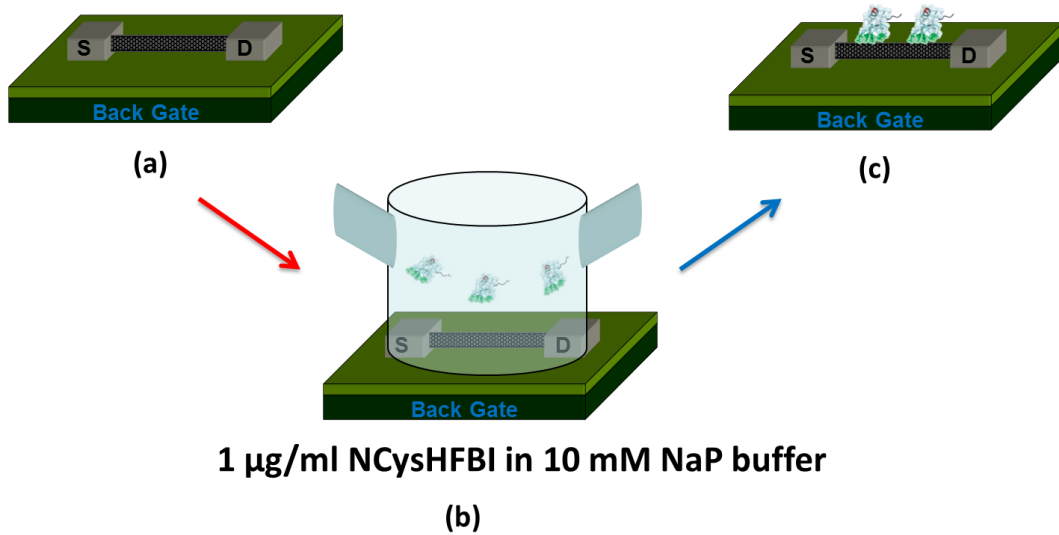
Figure 5.2: A simplified schematic displaying the experimental process on sensing hydrophobin molecules. The electronic properties of CNT-FETs were measured in dry condition (a), in 1 μg/ml NCysHFBI protein solution (b) and again in dry condition after being treated with hydrophobin (c).

same location of pristine (red dotted line in Figure 5.3(a)) and hydrophobin-treated (blue dotted line in Figure 5.3(b)) SWNT are shown in Figure 5.3(d) and evidently indicate the increase of surface roughness after protein adsorption which also confirms the adhesion of NCysHFBI on SiO$_2$ surface, and therefore causing the complexity in verifying the actual diameter of exposed CNTs. On the other hand, we have found that sonicating CNT sample in acetone for 10 min can completely remove the NCysHFBI molecules attached on CNTs and SiO$_2$ surface (see Figure 5.3(c)), as the surface roughness turns to be as initially. The result of protein adsorption on MWNT can also be seen in Figure 5.3(f) whereas Figure 5.3(e) displays an initial MWNT prior to protein treatment.

Since NCysHFBI is an amphiphilic protein consisting of hydrophobic and hydrophilic domains, hydrophobin is able to bind to other non-polar materials with non-covalent bonding via its hydrophobic patch [72]. In this work, NCysHFBI molecules non-covalently adhere to CNTs and SiO$_2$ surface due to both materials are hydrophobic, as observed in Figure 5.3(b) and 5.3(f). This non-covalent interaction is known to be weak and can be easily overcome.
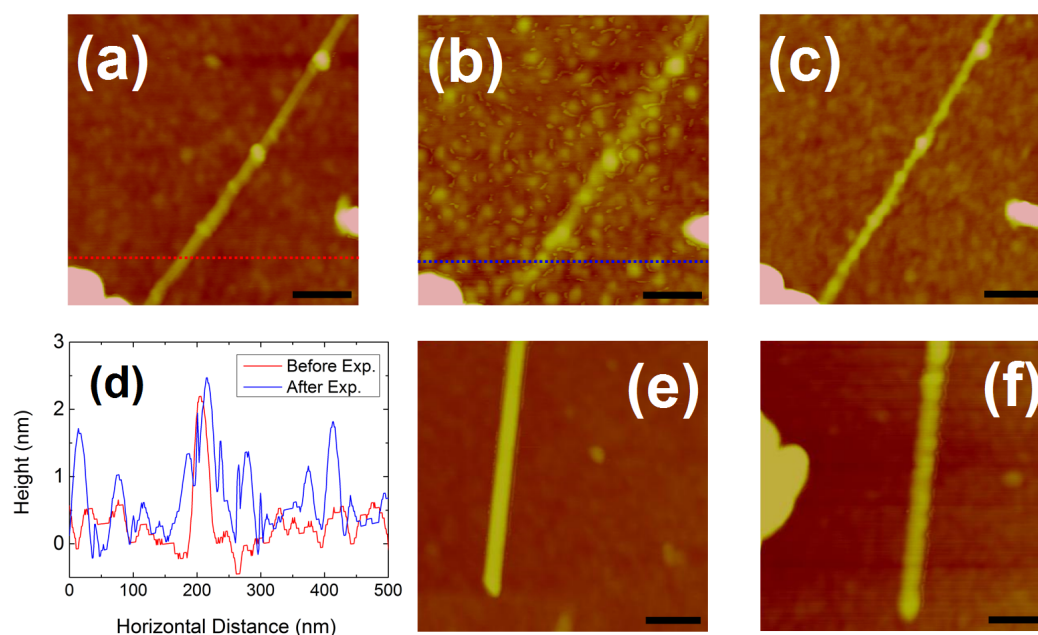
Figure 5.3: AFM images showing the same SWNT of diameter 2.3 nm (a-c) and MWNT of diameter 8.5 nm (e-f) deposited on Si/SiO$_2$ substrate. The treatment on SWNT is as (a) pristine SWNT, (b) after exposure to NCysHFBI solution and (c) after sonication in acetone for 10 min. Panel (d) displays the height profiles measured along the dotted lines in panels (a-b), and essentially reveals the change of surface roughness due to hydrophobin adsorption. While panel (e) shows an as-deposited MWNT and panel (f) presents the same MWNT after immersion in NCysHFBI solution. Scale bar (black solid line) in each image is 100 nm.

5.3.2   TEM and the labelling with gold nanoparticles

Moreover, the suspended SWNTs treated in different conditions have been imaged by transmission electron microscopy (TEM) as illustrated in Figure 5.4. The result shows that AuNPs do not attach to bare SWNTs (Figure 5.4(b)) so the outcome is basically similar to pristine SWNTs (Figure 5.4(a)), while the NCysHFBI proteins are widely found to adhere on SWNT sidewalls (Figure 5.4(c)). However, we notice that hydrophobins incoherently attach along the tubes and they are frequently observed to have a capsule-like structure. Eventually, the labeling by AuNPs to confirm the NCysHFBI adsorption (NCysHFBI-AuNP conjugations) has been successfully achieved as seen in Figure 5.4(d). This is because hydrophobins adhere to SWNTs with hydrophobic side and leave hydrophilic domain free to bind with functionalized AuNPs, in which such conjugation has been demonstrated to be capable of patterning the hybrid nanostructures [27]. We have also found that NCysHFBI molecules are able to form as a film structure even though there is no support under its layer (Figure 5.4(e)). These protein layers are quite often found in suspended SWNT samples and tend to be hanging in a relatively stable manner.

5.4 The electronic transport measurements: the effect of protein adsorption on CNT-FETs

The gate transfer characteristics of as-fabricated SWNT-FETs (Figure 5.5(a)) and MWNT-FETs (Figure 5.5(b)) have been plotted with red traces and clearly indicate p-type semiconducting behavior with the current ratios $I_{ON}/I_{OFF} \approx 4$ and ≈ 1 orders of magnitude for SWNTs and MWNTs, respectively. Their hysteresis, indicated by the arrows drawn in Figure 5.5, which is basically caused by local charge accumulation in the vicinity of the CNTs, is shown to be in the advanced direction [77, 78]. These p-type transport properties are quite often found in CNTs contacted with high work function metals measured at room temperature [9, 33]. After exposure to NCysHFBI molecules, the electronic properties of SWNT-FETs and MWNT-FETs (displayed by blue curves) remain p-type with the same hysteresis direction as observed before protein adsorption. Noticeably, the ON-state current (I_{ON}) of both types of FET devices significantly decreases when having hydrophobins attached onto their sidewalls. We discover that the reduction in device ON-state conductance (G_{ON}) for SWNTs is typically larger than MWNTs, pointing out that the electrical effect by protein attachment on SWNTs is stronger than on MWNTs. Figure 5.5(a) illustrates an example SWNT-FET device having the G_{ON} decrease of ~ 1 order of magnitude which is mostly observed for SWNTs while Figure 5.5(b) shows the best gate response of a MWNT-FET device among all MWNTs measured in this work with the biggest G_{ON} drop of ~ 0.5 order of magnitude. The ON-state resistance (R_{ON}) at $V_g = 0$ V of SWNT has approximately changed from 70 kΩ to 1.7 MΩ and from 7 kΩ to 35 kΩ for MWNT, as can be seen in the insets. The measured devices are summarized in Table 5.1 at the end of this Chapter.

We believe that the mobility of CNTs after exposure to NCysHFBI has decreased because of hydrophobins adhered on their sidewalls, and therefore leading to reduction of electrical conductivity. These attached particles can potentially contribute to an addition of scatterers along CNTs, as already seen in AFM and TEM images. The introduced scattering sites are able to hinder the electrical transport (i.e. hole for p-type) and slow down the drift velocity (V_D) of charge carriers. As a simple scenario, mobility can be considered analogously as an average speed (called drift velocity-V_D) of charge carriers traveling in materials [29] and implies how fast an electron/hole can transport through metal/semiconductor under the applied electric field. The mobility (μ) is then given by:

$$V_D = \mu E \tag{5.1}$$

where E is an electric field supplied across such material. The mobility in semiconductor is basically relevant to the impurity concentrations as well as defect concentrations.

Although the electrical conduction of CNTs in the diffusive regime is mainly determined by scattering, resulting in a certain drift velocity, the increase of scattering events in CNTs definitely diminish further the conductivity. To be more specific, the field-effect mobility (μ_{FE}) is often used to compare device properties instead of effective mobility (μ) due to the difficulty in defining an exact threshold voltage (V_{th}) of the gate dependent (I-V_g) characteristics [38]. This factor is a device-specific parameter which includes the practical device relevance i.e. contact resistances. The field-effect mobility (μ_{FE}) is thus given by [38]:

$$\mu_{FE} = \frac{L}{c_g} \frac{\partial G}{\partial V_g} \tag{5.2}$$

Where L is the channel length of a FET device, c_g is the capacitance per length and G is the conductance. We have calculated the field-effect mobility of our SWNT-FET devices by employing Equation 5.2 in which we obtain the mobility prior to protein exposure as $\mu_{FE} \approx 1500$ cm^2/Vs and after protein adsorption as $\mu_{FE} \approx 120$ cm^2/Vs. These results distinctly manifest the decrease in device mobility (~ 1 order of magnitude) which also worsens the electrical conductivity of SWNT-FET devices. In contrast, most MWNTs show very little change in their mobility. This biomolecular sensing mechanism based on mobility degradation has been also explored by investigating CNT-FET devices with various protein molecules [79, 80].

Furthermore, the time-dependence measurement of drain current (I_d) upon NCysHFBI adsorption has been monitored as shown in Figure 5.6(a). The transconductance of SWNT-FET was first measured in plain NaP buffer (see inset of Figure 5.6(a)) and the device was then set at its ON-state conduction by adjustment of gate voltage. The ON-state current is observed to be stable in pure buffer solution until the NCysHFBI molecules are introduced into a flow cell at a moment indicated by the arrow in Figure 5.6(a). Soon after that, the drain current rapidly decreases until the device reaches the OFF-state conduction, and a new stable drain current is finally obtained in a few minutes later. Notably, the change in this device conductance is ~ 2 orders of magnitude. This increase of nanotube resistance is obviously a consequence of NCysHFBI molecules which adsorb onto the tube sidewalls. These molecules act as extra scattering centers that can obstruct the current going through CNTs. It basically implies that the device mobility subsides when CNTs have hydrophobins deposited on their sidewalls.

We have also investigated the gate transfer characteristics measured during exposure to NCysHFBI molecules, as plotted in Figure 5.6(b). The current-gate dependent measurement was carried out by sweeping gate voltage from positive to negative as several loops at a fixed source-drain bias of $V_{ds} = 10$ mV in different conditions. The transconductance of SWNT-FET was first monitored in pure 10 mM NaP buffer solution pH7 (dotted lines), and later in a mixture of NCysHFBI and NaP buffer

(solid lines). We notice one major effect during protein exposure; it is involved with an alternation of hysteresis responses. Without NCysHFBI molecules in a flow cell, the current-gate behaviors monitored in plain NaP buffer show retarded hysteresis (dotted traces) [81]. On the other hand, the current-gate responses have changed to advanced hysteresis after having NCysHFBI flowed into the chamber (solid traces). This obvious influence on device hysteresis is possibly caused by hydrophobins coated on CNTs and also SiO_2 surface that might perturb the effective electric field of the system. This is to some extent a promising evidence to probe and confirm that NCysHFBI molecules truly adsorb to CNTs.

Ultimately, we note here that the current-time and the current-gate dependent measurements of MWNT-FETs in the presence of NCysHFBI were also done similarly to the experiments in SWNTs. However, the change in device conductivity and hysteresis is observed to be extremely small, compared to SWNTs. It seems that hydrophobins do not significantly affect the electronic properties of MWNTs. Even though they do affect, the influence on MWNTs is still rather weak than on SWNTs. We therefore suggest that individual MWNT-FETs are most likely not suitable for utilizing as biomolecular sensors.

## 5.4.1   Channel length dependence on device conductance

We have also plotted the ON-state conductance (G_{ON}) of SWNT-FET devices, as measured before and after exposure to NCysHFBI (red and blue squares, respectively in Figure 5.7), with respect to their channel length (L). Interestingly, we find that devices with longer channel length tend to be more sensitive to hydrophobin molecules as the ON-state conductance is observed to diminish more in relative terms, than in shorter SWNT devices, even though the result somewhat displays a spread of data points in the plot. This channel length dependent phenomenon is possibly relevant to the number of scattering sites added to the nanotube surface which will likely be a lot more for longer conducting channels. When CNTs contain many scattering centers, their electrical transport is easily hindered by these particles, and thus contributing to the increase of device resistance. The channel length correlation on the electronic properties of SWNT devices could be useful for the bio-molecular sensing and presumably other detecting applications. This result suggests that the SWNT-based biosensors will be more sensitive and efficient with longer channel lengths.

Device	Diameter (nm)	Channel length (nm)	R_{ON} (before NCysHFBI exp.)	R_{ON} (after NCysHFBI exp.)
1	2.4	600	370 kΩ	440 kΩ
2	2.0	880	8.85 MΩ	53.76 MΩ
3	2.5	930	1.03 MΩ	1.77 MΩ
4	2.2	1170	950 kΩ	106.16 MΩ
5	1.7	580	860 kΩ	610 kΩ
6	2.3	900	70 kΩ	2.56 MΩ
7	2.3	520	810 kΩ	6.95 MΩ
8	2.1	930	330 kΩ	2.35 MΩ
9	2.0	530	910 kΩ	520 kΩ
10	2.6	480	460 kΩ	510 kΩ
11	2.1	370	220 kΩ	420 kΩ
12	3.5	600	200 kΩ	1.07 MΩ
13	2.9	360	70 kΩ	1.04 MΩ

Table 5.1: List of 13 conventional (symmetric) Au-contacted CNT-FET devices measured as before and after exposure to NCysHFBI proteins.
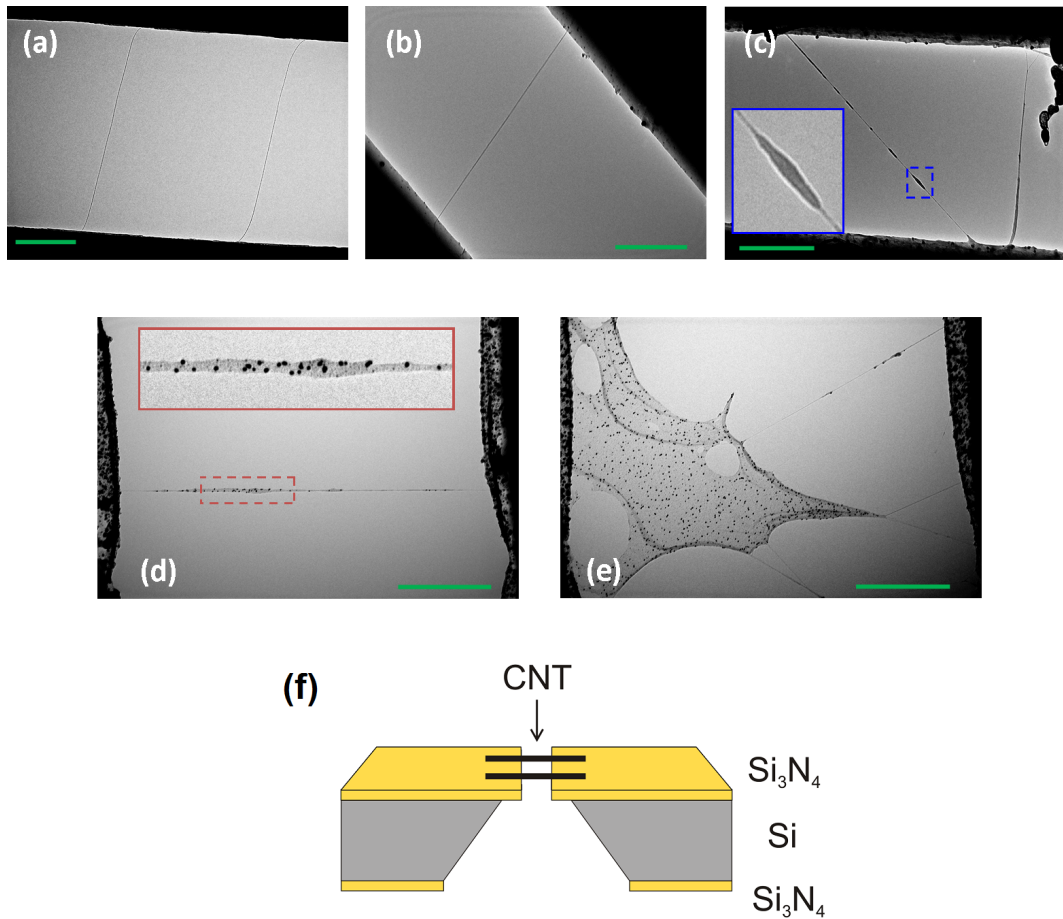
Figure 5.4: TEM images showing individually suspended SWNTs on silicon nitride slit as such (a) as-grown SWNTs, (b) after exposure to AuNP solution, (c) after incubation with NCsyHFBI solution, (d-e) after immersion in NCysHFBI solution and then followed in AuNP solution. The labeling of gold nanoparticles is successfully obtained, and indicating the immobilization of NCysHFBI proteins on SWNTs. The insets of panels (c-d) display the zoomed-in area of dash-line rectangles. A scale bar (green solid line) in each image is 500 nm. Image (f) illustrates the schematic of individual CNTs suspended on slit sample.
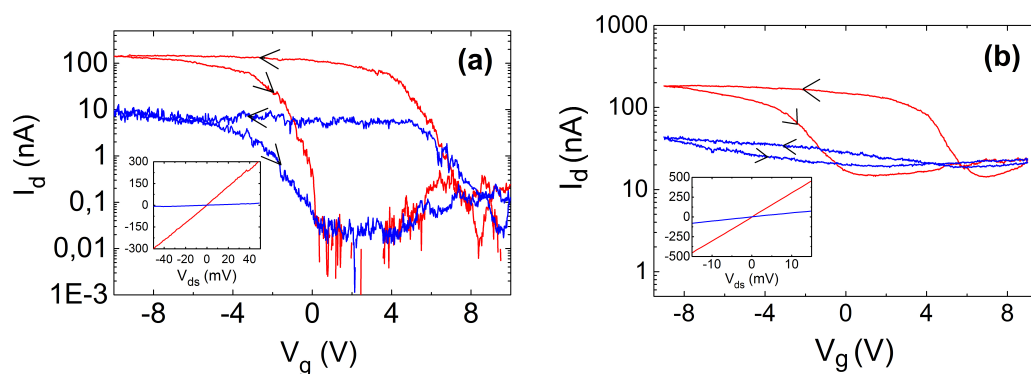
Figure 5.5: Showing the gate transfer measurements (I-V$_g$) of (a) SWNT-FET and (b) MWNT-FET while the insets are their I-V$_{ds}$ characteristics. The electronic transport properties of CNTs before exposure to NCysHFBI are plotted as red trace and after protein adsorption are plotted as blue trace. The source-drain voltage supplied to SWNT and MWNT is set constant at 10 mV and 1 mV, respectively.
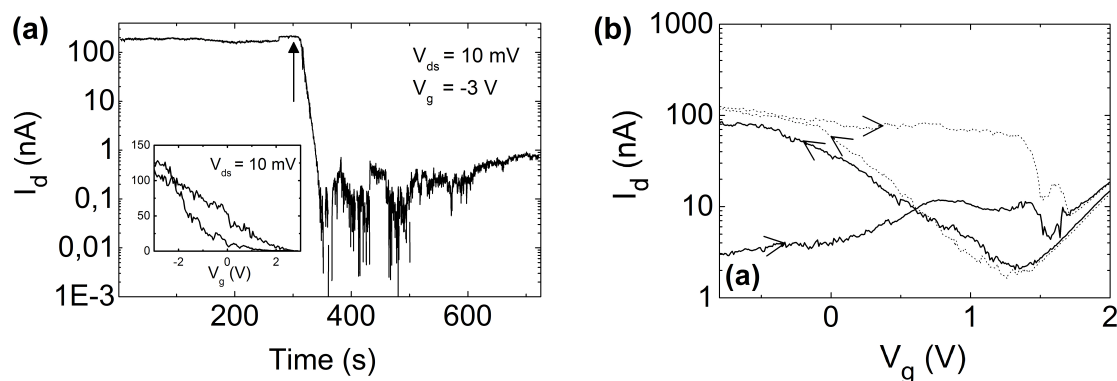
Figure 5.6: Real-time detections of SWNT-FETs in the presence of NCysHFBI molecules introduced into flow chamber. (a) Current-time dependent measurement is carried out with having source-drain voltage (V$_{ds}$) and gate potential (V$_g$) fixed at device ON-state conduction. The inset in panel (a) is the I-V$_g$ characterization in pure NaP buffer. (b) Current-gate response is performed with several gate voltage sweeps in pure NaP buffer solution (dotted lines) and in NCysHFBI/NaP (solid lines) at a constant bias of V$_{ds} = 10$ mV.
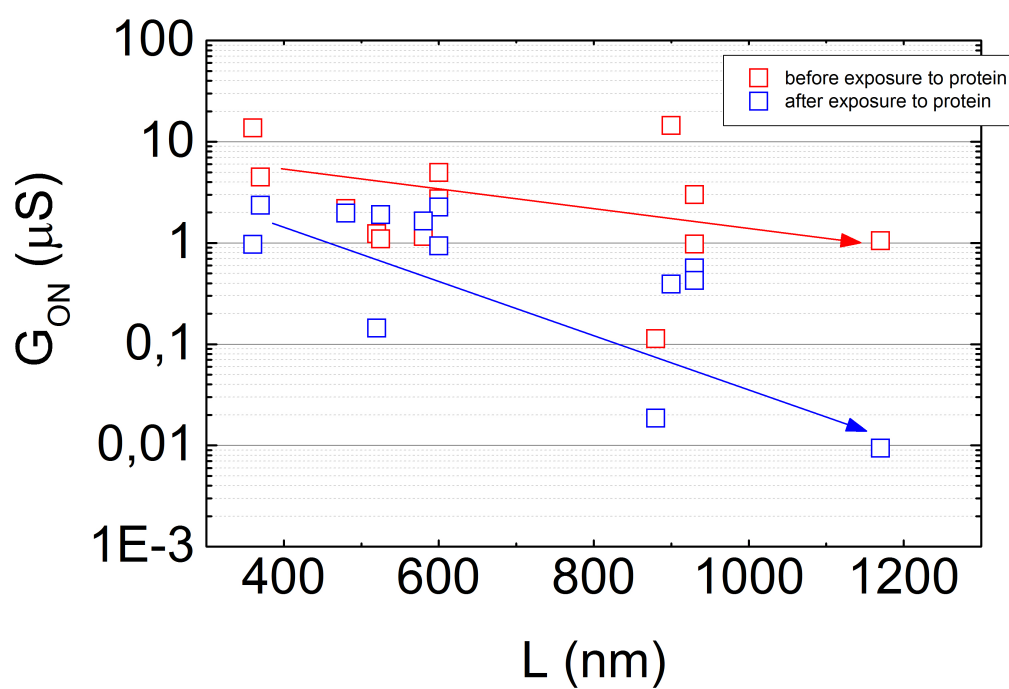
Figure 5.7: ON-state conductance (G_{ON}) plotted versus channel length (L) of p-type SWNT-FET devices measured in ambient (T = 300 K) as before (red square) and after (blue square) exposure to NCysHFBI molecules.

6 Electrical measurements on SWNTs contacted with asymmetric electrode configuration

6.1 Background on CNT contact configurations and motivation of this work

We have studied CNT-FET devices having different contact structures designed on the same tube. Normally, a CNT-FET device is fabricated in such a way that two metal electrodes are electrically contacted above carbon nanotube by normal vapour depositioning, acting as source and drain terminals, and we therefore call this contact feature (in this work) as conventional and/or symmetric contact configurations. Such contacts which has one metal electrode deposited on top of the nanotube are called "**embedded contacts**" and are depicted in Figure 6.1(a)-right. The other type of contact is called a "**line contact**", and is also shown in Figure 6.1(a)-left. This contact consists of pre-patterned metal on which the CNT is placed partially on top of. The key point is to focus on the different contact topologies of these specific samples where the symmetric CNT-FET device has both ends as embedded junctions while the asymmetric CNT-FET device composes of one end as embedded- and another end as line-junctions (see Figure 6.1(a-b)). Essentially, we have exploited the sufficiently long nanotubes which can combine these two different contact configurations on the same tube (see Figure 6.1) in order to make the results comparable and reliable.

With having different electrode configurations on the same CNT, the electronic properties of nanotube in different device sections (symmetric and asymmetric devices) are under certain circumstances expected to behave diversely in the same environment. Gold (Au) and palladium (Pd) metals have been chosen to perform as electrical contacts in these studies with low temperature measurements and on influence of oxygen (air). Since Au and Pd are well-known to provide ohmic contacts with CNTs [9,32,33], it would be interesting to explore the influence of both contact structures with these metals.

The fabrication method of CNT-FETs having both contact features has already been described in Chapter 3. We basically note here that the CNT materials used in

this experiment are mainly single-walled carbon nanotubes (SWNTs) and possibly few of double-walled carbon nanotubes (DWNTs). The device morphology of both symmetrical- and asymmetrical-contacted SWNT devices can be seen as AFM images in Figures 3.6 and 3.11, respectively. Besides, a diagram displaying the fabrication process as step-by-step has been provided in Figure 3.8.
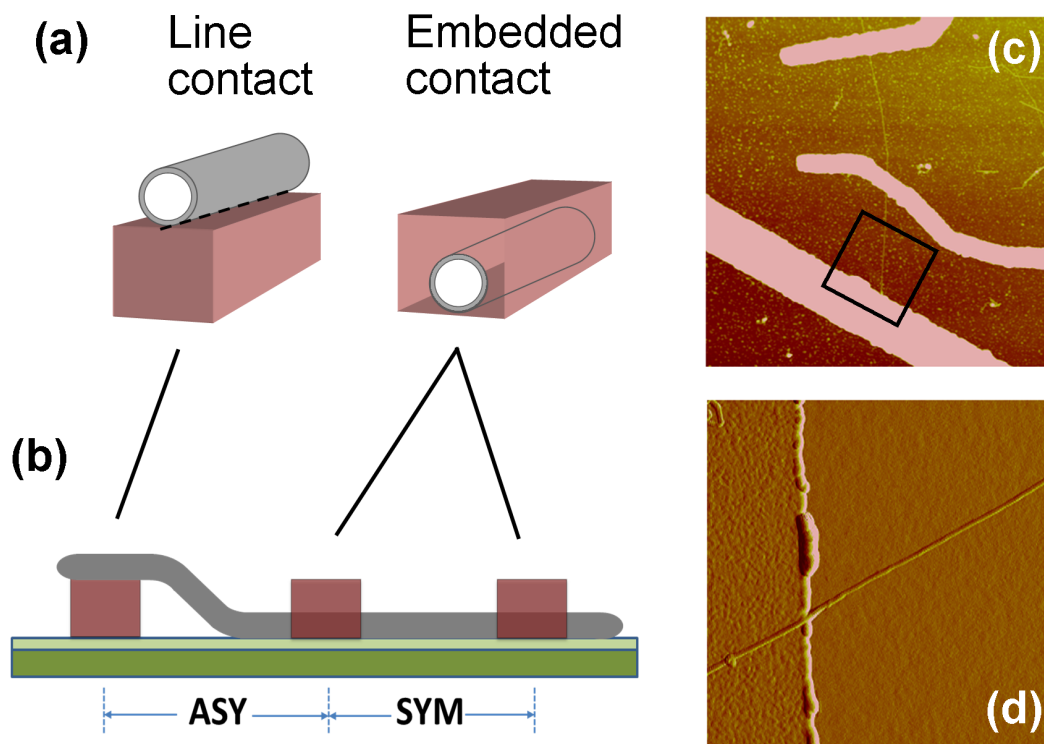
Figure 6.1: (a) Illustration of different metal-nanotube contact configurations. Line contact represents nanotube placed on top of electrode while embedded contact as metal deposited on top of nanotube. (b) Schematic of SWNT device consisting of asymmetrically (ASY) and symmetrically (SYM) contacted sections. (c) AFM image of an actual device showing a SYM section (upper electrode pair) and an ASY section (lower pair). (d) A magnified image, from the square in panel (c), displaying the line contact feature of the ASY section with nanotube lying on top of electrode. The image size is 1 μm and the tube diameter is ~ 2.9 nm.

6.2   Experimental setups and measurement details

Cryogenic setup

The Si chip containing several as-fabricated CNT-FET devices was inserted into a sample socket which is already mounted at the end of a home-made dipstick. A metallic cylinder closed from one end was utilized to cover the sample and was tightly sealed

with indium wire O-ring. The setup was then pumped down to vacuum until a pressure of ~ 0.01 mbar was reached. We afterwards brought the dipstick into a liquid helium dewar in which the sample was cooled down to 4.2 K. The temperature was approximately adjustable by controlling the height of the dipstick with respect to the liquid helium level and was monitored with a sensor placed nearby the sample.

The electronic properties of SWNT-FETs having both symmetric- and asymmetric-contacted devices were measured at different temperatures varied from room temperature (300 K) to liquid helium temperature (4.2 K). The source-drain voltage (V_{ds}) was always kept constant at $V_{ds} = 10$ mV for the gate transfer characterizations while having gate potential (V_g) swept for a few loops from positive to negative values. In addition, the I-V characteristics of SWNTs were measured. A more detailed explanation for cryogenic experimental setup has been previously described in Chapter 3 - section 3.3.4 Low temperature measurement setup. Also the schematic of a whole electrical measurement setup has been earlier illustrated in Figure 3.12.

Oxygen sensing setup

We note here that, there was an opportunity to study the effect of oxygen molecules on the device sensitivity. Before getting the setup under vacuum, we can measure the electrical transport behaviors of CNT-FETs at this stage as in ambient or oxygen condition. When the electrical measurements of oxygen sensing had been completed, the setup was further proceeded to be cooled down. The gate transfer measurements of SWNT-FET devices in oxygen and vacuum environments were carried out with having source-drain bias (V_{ds}) fixed at $V_{ds} = 10$ mV and having gate voltage (V_g) scanned from positive to negative values for several loops. At the same time, I-V characteristics of SWNTs were also measured in both conditions.

6.3   Transport measurements

In this section I describe the results of our measurements on the asymmetrically contacted SWNT-devices. Key data on the devices measured are summarized in Table 6.1 at the end of this Chapter.

6.3.1   Low temperature conduction measurements

The I-V_{ds} characteristics and the gate transfer measurements (I-V_g) at 300 K and 4.2 K of Pd-contacted SWNT devices are shown in Figure 6.3 (a) and (b), respectively. The
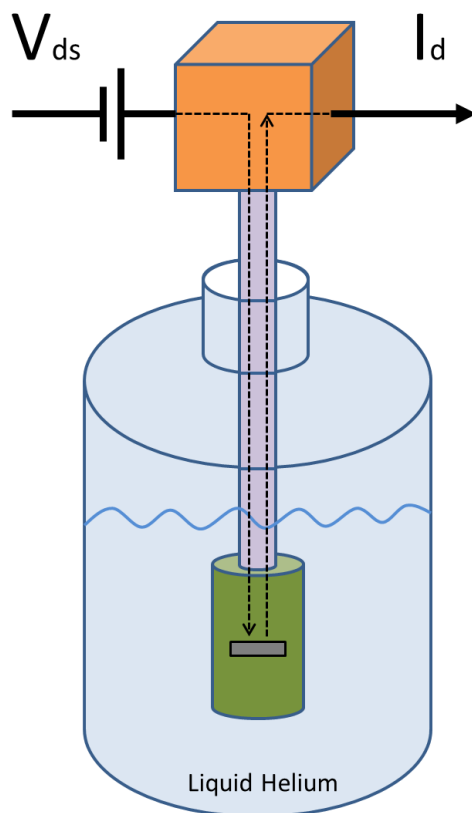
Figure 6.2: Showing a schematic of cryogenic measurement setup. A sample chip (grey rectangle) is mounted inside the chamber can (olive cylinder) and dipped into liquid helium (light-blue tank). The source-drain voltage (V_{ds}) is supplied between wires coming in and out, and the drain current (I_d) is basically measured with the external electronic equipment.

ASY section is indicated by red traces whereas the SYM section by black traces. The ASY and SYM devices are truly semiconducting with ON/OFF ratio of $\sim$ 2-3 orders of magnitude at 300 K. It is obvious that the ON-state current of the ASY section is significantly smaller than the ON-state current of the SYM section by approximately 1 order of magnitude, thus revealing that ASY device is more resistive than SYM device. The resulting resistances measured at 300 K are estimated to be 2.5 MΩ for the ASY section and 300 kΩ for the SYM section. The I-V_{ds} characteristics (at $V_g = 0$ V) of both ASY and SYM sections are linear at 300 K, however they behave non-linearly at 4.2 K. The SYM configuration actually shows a relatively symmetrical I-V_{ds} behavior at 4.2 K while the ASY configuration asymmetrically responds similarly to Schottky diode-like behavior [82]. Besides, the Coulomb blockade phenomena as drain-current oscillation can be observed at 4.2 K.

In the case of Au-contacted SWNT-FET devices comprising of ASY and SYM sections, they have also been explored in the range between 300 K and 4.2 K. However there

is no such systematic dependence on the different contact configurations observed in the experiment, unlike as clearly seen in Pd-contacted SWNT-FETs. The results are to some extent ambiguous because in some SWNTs, the ASY section is more conductive than the SYM section (opposite to the case of Pd-based contacts) whereas some SWNTs yield the same relation as obtained from Pd-SWNT devices.

The effect of different contact structures in Pd-based SWNT-FET devices is obviously distinguishable but relatively unclear for Au-based devices. This difference can be considered as a result of the surface oxidation and/or adsorption properties of these metals. Both are actually classified as noble metals according to their common definition. However, it is known that Pd can be contaminated and covered by other molecular surface layers very quickly in UHV condition while Au is easy to keep clean for a long time [83]. In addition, Pd is observed to form a thin oxide layer (with a chemical formula of Pd_5O_4) in the presence of oxygen and at moderate temperature conditions [84, 85]. Thus in our experiment, an atomically thin insulating layer of palladium oxide is most likely formed at the surface of Pd metal electrodes during the device fabrication because all SWNT-FET samples require several baking steps at $\sim$ 170°C for the e-beam lithography. Note that the thickness of this oxide is very small or even negligible in most cases as Pd is sorted in noble metal group, unlike non-noble metals for example Al and Ti which their native oxide layers are basically formed and detectable.

We therefore believe that the thin insulating layer of palladium oxide formed at the Pd-SWNT interface affects the charge transport mechanism at ASY junctions of asymmetrical-contacted SWNT-FET devices. This kind of thin oxide layer is actually acting like a tunneling barrier for the electron transport and this barrier is clearly observable in the I-V_{ds} characteristics measured at 4.2 K of Figure 6.3(a), as the ASY section I-V_{ds} curve is strongly asymmetric whereas the corresponding SYM section is symmetric.

6.3.2 Sensitivity of asymmetric-structured contacts to oxygen

The sensitivity to normal air of the ASY and SYM designed Pd-SWNT devices has been monitored in ambient and vacuum (0.01 mbar) conditions. The results from 6 SWNTs are shown in Figure 6.4. It is apparently seen that all the ASY devices are more resistive than the SYM devices. In addition, almost all the ASY sections are more sensitive to the presence of air than the SYM sections, as the resistance of ASY sections significantly decreases upon exposure to air while the SYM sections present the relatively tiny change in resistance.

Based on the previous studies [86, 87], it has been demonstrated that the reactive component in air is basically oxygen (O_2) and the effect of nitrogen (N_2) is negligible.
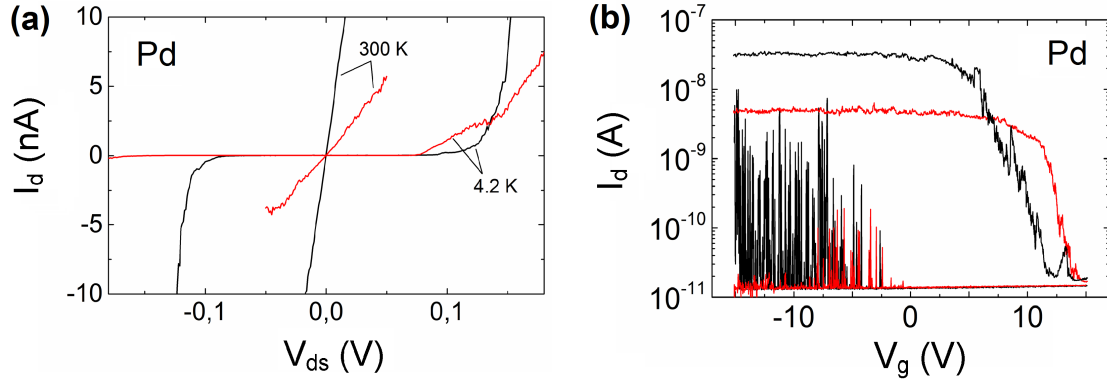
Figure 6.3: (a) I-V_{ds} characteristics of the ASY (red) and the SYM (black) configurations of Pd-contacted SWNT-FET devices measured at 4.2 K and at 300 K without gate potential ($V_g = 0$ V). (b) The gate transfer response I-V_g, of both ASY and SYM Pd-SWNT devices measured at 4.2 K (two lower curves) and at 300 K (two upper curves) with a fixed source-drain voltage of $V_{ds} = 10$ mV.

Besides, oxygen molecule is known as an oxidizer that can typically react to nanotube sidewalls [88]. Upon O_2 exposure and adsorption, the charge transfer tends to be increased as a consequence of the electron-withdrawing power of O_2 molecules which causes the doping to SWNTs with hole carriers [88]. This mechanism contributes to the increase of electrical transport in SWNTs, and then should equally affect the resistances of the same SWNT devices, no matter what kind of contact configurations are. However as we already stated, the resistance change due to O_2 adsorption of the ASY and SYM devices is different, the changes in ASY sections are mostly larger than in SYM sections. This implies that there might be other key factor(s) which plays an important role to the ASY structures (line contact). One possibility is the direct modification of SWNT work function as the oxygen doping onto carbon nanotube results in the increase of its work function [86, 88]. Since the work function of Pd is $\sim$ 5.12 eV and of SWNT is $\sim$ 4.9 eV [82, 89], the work function difference between Pd and SWNT after O_2 adsorption and doping should decrease and thus leading to the enhancement of device conductance. The second possibility is that the surface area of SWNTs with ASY configurations is larger than the surface area of SWNT devices with SYM contact design to interact and get chemisorbed with O_2 molecules. This difference can also affect, though maybe minor, the electrical conduction of SWNTs after being exposed to air, and thus contributing to the larger decrease in resistance of the ASY sections.

We eventually suggest that this kind of specific-made contact structure (ASY) is quite sensitive to ambient air (or oxygen) rather than a typical-made contact configuration (SYM) and it can be possibly utilized as a gas sensor.
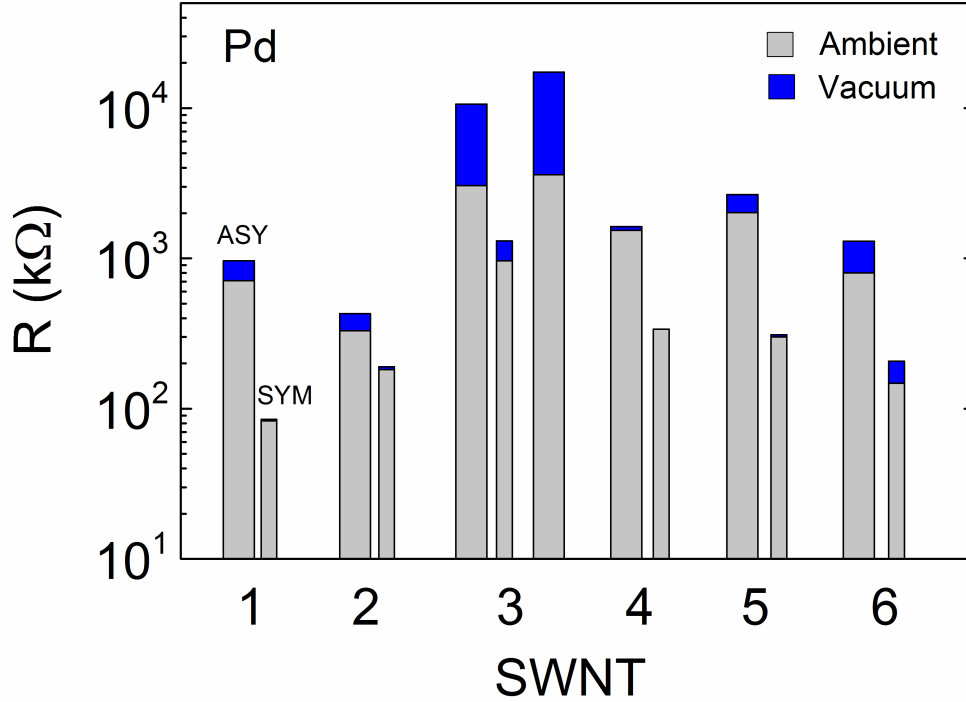
Figure 6.4: Diagram displaying the resistances at ON-state conduction of ASY (wide columns) and SYM (narrow columns) Pd-contacted SWNT-FET devices measured in ambient and vacuum conditions at 300 K. In the most cases, one nanotube basically consists of two different sections (ASY and SYM) but except SWNT #3 which has two ASY sections.

Device	Diameter	Channel length (nm)		R_{ON} (Ambient)		R_{ON} (Vacuum)	
(Pd)	(nm)	ASY	SYM	ASY	SYM	ASY	SYM
1	3.0	950	1100	800 kΩ	150 kΩ	1.3 MΩ	210 kΩ
2	2.1	910	1020	1.53 MΩ	340 kΩ	1.63 MΩ	330 kΩ
3	2.9	700	550	2.01 MΩ	300 kΩ	2.66 MΩ	310 kΩ
4	2.9	370	350	710 kΩ	80 kΩ	960 kΩ	90 kΩ
5	4.9	1100	720	330 kΩ	180 kΩ	430 kΩ	190 kΩ
6	1.6	640	600	3.05 MΩ	970 kΩ	10.63 MΩ	1.3 MΩ
		920		3.6 MΩ		17.39 MΩ	

Table 6.1: List of line (asymmetric - ASY) and embedded (symmetric - SYM) Pd-contacted CNT-FET devices measured in ambient and vacuum conditions.

7 Hemicellulose-CNT materials as transparent and conductive films

We have done the very first studies on CNT/Hemicellulose complex materials, which has very recently been developed by a local company. The role of the hemicellulose is to render CNTs water soluble. Section 7.1 describes the background to this topic and presents the measurements done in this work. Section 7.2 describes the experimental details of the measurements. Sections 7.3 and 7.4 describe the results of structural and conductivity measurements undertaken for the thin films of CNT/Hemicellulose studied.

7.1 Background: Cellulose and carbon nanotubes

Cellulose

Cellulose (β-(1,4)-D-glucopyranose polymer) is a natural linear polysaccharide in which D-glucopyranose rings are linked to others by β-(1→4)-glycosidic bonds [90]. Cellulose is one of the most crucial natural polymers among the bio-based materials and a key biosource of sustainable materials on an industrial scale [91]. Native cellulose basically consists of bundles of nanofibrills with the width in the range of 3-50 nm, depending on its origin [92]. Cellulose is the most abundant bioresource and it has outstanding mechanical and thermal properties [90]. The macroscopic Young's modulus of natural plant cellulose is relatively high up to 128 GPa which is higher than aluminum (70 GPa) and glass fibers (76 GPa) [93]. Its tensile strength is also large and estimated to be 17.8 GPa which is 7 times stronger than steel [94]. Cellulose nanofibrils have low thermal expansivity (0.1 ppm K^{-1}) and they are known not to melt but to thermally degrade at high temperatures [90]. These interesting and promising properties of cellulose nanofibrils show the potential to replace glass fiber as well as to be efficiently utilized as a reinforcement fiber for environmental-friendly composites. With the nanometer sizes of the structural elements, nanocellulose has a large surface area and therefore contributing to the effective interaction to surrounding components for instance water molecules, organic and polymeric compounds, nanoparticles, and living cells. Nanocelluloses (or cellulose nanofibrils) are in fact unique and consist of

substantial cellulose properties: hydrophilicity, broad chemical modification capacity, and the formation of versatile semicrystalline fiber structures [91].

Hemicellulose

Hemicellulose (also known as 'Polyose') is a heteropolymer (matrix polysaccharide) and is one type of various cellulose structures, appearing along with cellulose in almost all plant cell walls (see Figure 7.1). Hemicellulose contains many different sugar monomers such as glucose, xylose, mannose, galactose, and etc., whereas cellulose contains only glucose monomers [95]. However hemicelluloses are amorphous and weak with little strength while celluloses are crystalline and strong. Besides, a hemicellulose polysaccharide contains various shorter chains of 500 - 3000 sugar units per polymer which is obviously smaller than cellulose - which comprises of 7000 - 15000 glucose units per polymer [95]. These unique physical components result in a branched heteropolymer structure for hemicelluloses but a linear (unbranched) polymer structure for celluloses. In particular with side chain configurations formed in matrix polysaccharides, hemicelluloses are thus more reactive than celluloses.

Cellulose-CNT mixtures

The use of cellulose in electronic applications is attractive within nanotechnological research, especially in combination with carbon nanotubes. As the CNT is known to be a very excellent conductor (even the best one), the cellulose-CNT composites can lead to relatively well conductive films and they are potentially capable of being manufactured in large-scale production i.e. simply fabricated by printing technique [92]. The transparent and conductive thin films made from TEMPO-Oxidized nanocellulose/CNT composites have been successfully obtained by Isogai et al. [92] in which the maximum electrical conductivity is given as 10 S/cm. This kind of composite film can be utilized as a transparent electrode and also to some extent as a humidity sensor. In addition, the incorporation of MWNTs into bacterial cellulose pellicles has been carried out by Pyun et al. [98] but the best electrical conductivity of cellulose/MWNT composites in this work is quite small as 1.4×10^{-1} S/cm. While the composite nanomaterial films consisting of carboxymethyl cellulose and MWNTs achieved by Kitsyuk et al. [99] show greater electrical conductivity at 1.2×10^2 - 4 $\times 10^2$ S/cm. Moreover, the cellulose/SWNT nanocomposites have been successfully demonstrated and characterized their mechanical, thermal and electrical properties by Park et al. [100]. They find that adding a small amount of SWNTs to the cellulose can improve the nanocomposite film properties in which, for instance with having 1% of SWNTs added, the tensile strain at break-point, Young's modulus and toughness
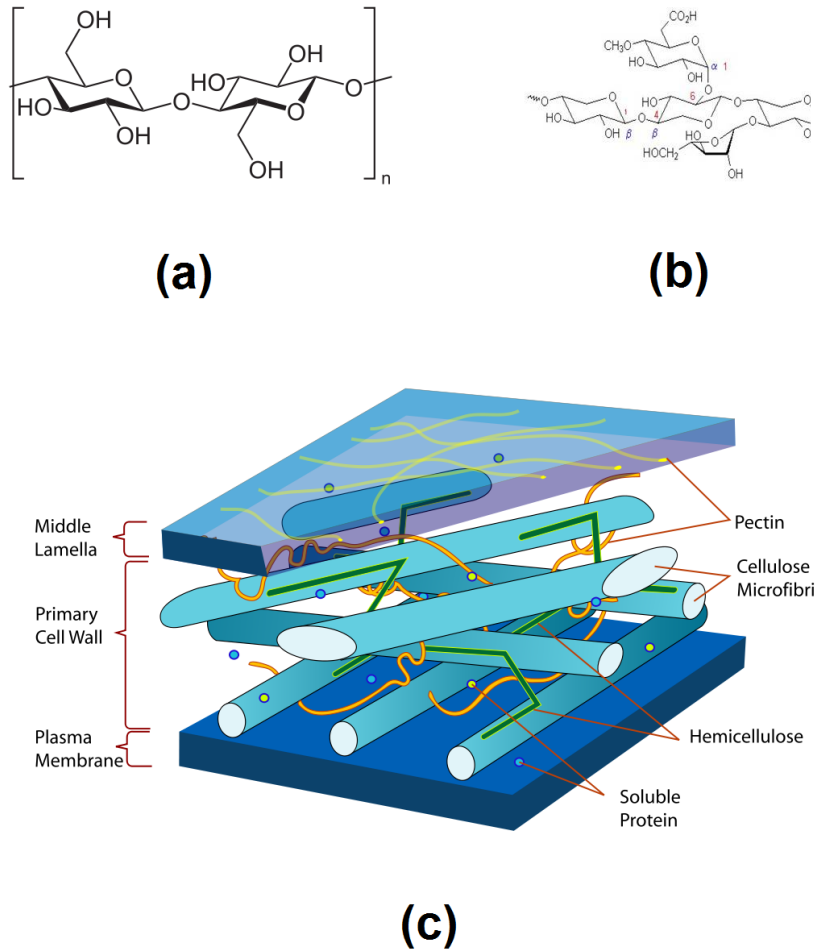
Figure 7.1: Schematics illustrating the chemical molecular structures of (a) cellulose - a linear polymeric chain consisting of only glucose units and (b) hemicellulose - a branched polymeric configuration comprising of different sugar monomers. (c) A cartoon displaying both celluloses and hemicelluloses found in the plant cell wall [96, 97].

increase $\sim$ 5.4, 2.2 and 6 times, respectively as well as the degradation temperature increases to 9 °C but the electrical conductivity is somewhat little at 3.74×10^{-2} S/cm.

Motivation of this work

Very recently, a local start-up company nEMCEl Ltd. [101], introduced a method [102] for mixing hemicellulose and CNTs, for the purpose of rendering the CNTs water-soluble. Therefore, the aim is not to make composites - the hemicellulose/CNT weight ratio is around 1/1, and thus in the dried material by and large the appearance of the

CNT/hemicellulose complexed material is close to that of pure bulk CNT material.

In this work the very first basic conduction measurements are undertaken of thin films that are made from this CNT/Hemicellulose complex dissolved in water and provided by nEMCEl Ltd. TEM and AFM images are also presented of the material.

7.2   Experimental details

Preparation of thin films from hemicellulose-CNT compound

The hemicellulose-CNT (HC-CNT) films were prepared on highly-doped silicon (Si) substrate covered with 500-nm thickness of thermally grown silicon dioxide (SiO_2) and with four electrodes having $\sim$ 3-nm Ti and 12-nm Au layers. The metallization of the electrodes was performed in UHV condition. Each pair of electrodes was equally separated by $\sim$ 200 μm - fixed for all samples in this work. A mixture of hemicellulose and double-walled carbon nanotubes (DWNTs) was dissolved in deionized water (DI) by a ratio of 1:1, followed with gentle shaking for a few times. Then a small amount of water-based HC-CNT solution was carefully dropped onto the surface of pre-patterned chips and at this point the volume of this droplet was controlled to be as small as possible but still spread thoroughly over the samples. From our previous experience, the size of the droplet had played an important role on the resulting film thickness: the smaller the droplet size the thinner the film. The HC-CNT films were obtained after the samples had been left dry in the fume hood (inside cleanroom) for 24-28 hr. In the case of thicker films, the repetition of this process was required until the desired film thickness was achieved. In addition, the effort to control the HC-CNT network thickness was further carried out via the spin-coating technique. The spinning speed was a key parameter to determine the thickness and therefore the HC-CNT films were achieved by spinning with different speeds. Note that reactive ion etching (RIE) was also employed to hydrophilize the SiO_2 surface before film deposition in both methods (drop-dry and spin coatings). Since the surface of SiO_2 is known to be relatively hydrophobic, SiO_2 indeed becomes more hydrophilic after the surface modification with RIE and thus the water-based HC-CNT suspension can be readily spread all over the chips.

In fact, the deposited films made by drop-dry coating technique had clearly darker edges due to non-uniform distribution of HC-CNT compound at the boundary of a droplet (an example is shown in Figure 7.2 (a)) while they were more uniform by the spin coating method. However all as-prepared films were then cleaned at the edges by using wet cotton sticks to leave only the uniform central area of each film and finally

had a rectangular shape, as well as covering all four electrodes. The morphological characterizations of all samples were carried out by optical microscope, AFM and TEM. The average film thickness was estimated by the data given from AFM images taken at the edges of the films (between film and SiO_2 surface).

Sample preparation for conduction measurements

A specific chip-carrier was used for the electrical measurement purposes and a ready chip was then attached on top of it. The final steps were to bond the wires and to connect the back gates to the HC-CNT samples. The ready devices for the electrical measurements in all conditions are shown in Figure 7.3 (a). Each device consists of four gold electrodes and two back-gate terminals while a rectangular transparent film made of HC-CNT material is deposited over all electrodes. The measurement circuit is basically set up as demonstrated in Figure 7.3 (b). In the experiments, the four-probe measurement technique is performed where the current (I) is applied throughout the film and the voltage (V) dropped across two inner electrodes is monitored.

The electronic properties of HC-CNT thin films with the thickness range of 8-100 nm had been investigated in three different environments. The electrical measurements were first done at low temperature (4.2 K - 300 K), then at high temperature (300 K - 420 K or $\sim$ 25-140°C) and finally under high humidity (up to $\sim$ 90% RH) conditions, separately.

## 7.3   Hemicellulose-CNT film characterizations

The hemicellulose-CNT film deposited on the glass is shown in Figure 7.2(a). Note that, this sample has been already wiped out partly at the right and left sides. However it still can be obviously seen that the boundary of the film is darker than the central area, as a result of non-uniform distribution of HC-CNT compound inside a droplet. With a ratio of hemicellulose and DWNTs as 1:1, the material is still somewhat transparent at its thickness of $\sim$ 40 nm. Moreover the HC-CNT film deposited onto the Si/SiO_2 substrate having Au electrodes patterned is shown in Figure 7.2(b), taken from an optical microscope. The composite material is located on the left side of the image (enclosed by dashed lines) while the gap represents the distance between two electrodes (specifically implying to the conducting channel). In addition, the AFM images have been taken at the central area and at the edge of the film, as shown in Figure 7.2 (c) and (d), respectively. In panel (c), it reveals the relatively homogeneous network of DWNTs including their bundles, and with a careful look one can observe many of the circular-shape CNTs. They are actually a bundle of DWNTs formed in

a ring structure. We found that these circular CNT bundles form before mixing in the pristine DWNT material together with hemicellulose as we also have observed the CNT rings in pure DWNT suspensions (DWNTs dispersed in dichloroethane). In panel (d), the thickness of the film can be estimated by measuring the height difference between a composite and SiO_2 surface, for example this film is approximately 10 nm thick (in average).

Note that the HC-CNT suspensions have been prepared since 16.7.2013 and they still remain well-dispersed in DI water (until now, for 9 months). Interestingly the deposited films are very sticky to both transparent-glass and SiO_2 surfaces, and also endurable to dry tools but easily removed by wet tools - for instance water-soaked cotton stick or water-soaked tissue paper.
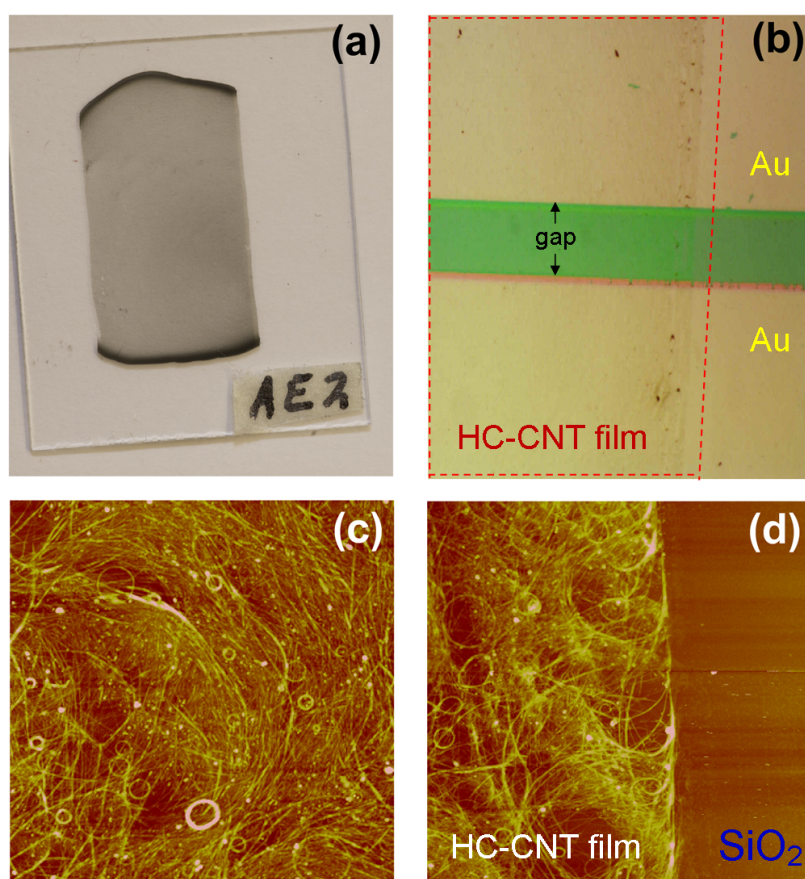
Figure 7.2: Displaying two different microscopy results: (a) and (b) as optical images, (c) and (d) as AFM images. In panel (a), HC-CNT film is prepared on the glass substrate by drop-dry coating method while panel (b) the film is deposited on an electrode-patterned Si/SiO_2 chip. The AFM image in panel (c) is taken at the central area whereas image (d) at the edge of the film. The size of both pictures (c) and (d) is 10 μm $\times$ 10 μm.
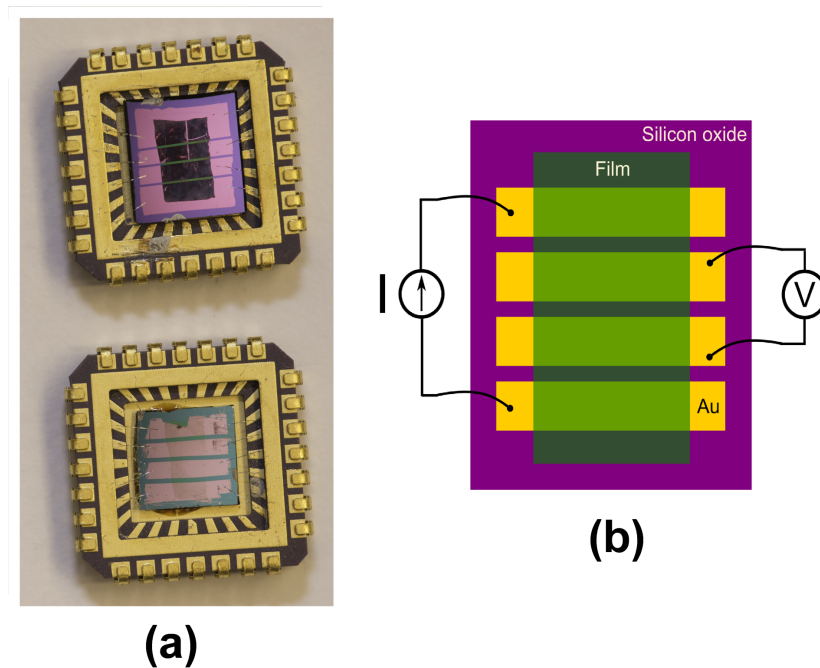
Figure 7.3: (a) Displaying two as-prepared HC-CNT devices for the electrical measurements. Films are transparent and particularly coated at the center of the Si/SiO$_2$ chips. (b) A schematic of four-terminal setup used in the electrical measurement for 2D thin films.
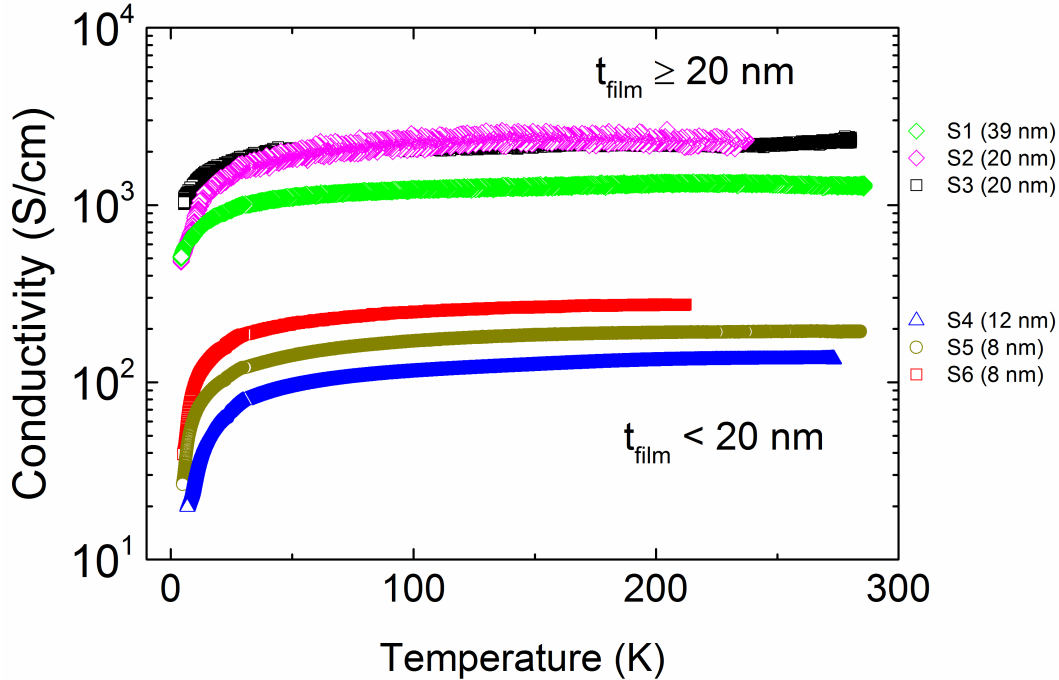
7.4 Conduction measurements

Low temperature conduction measurements

The electronic properties of Hemicellulose/CNT (HC-CNT) films having different thicknesses were first characterized as a function of temperature. The electrical conductivity of six HC-CNT samples was measured from room temperature (300 K) down to liquid helium temperature (4.2 K) as shown in Figure 7.4. The data points were taken continuously while the device temperature was being lowered. We find that the conductivity of our HC-CNT films monitored at room temperature is relatively high when compared to other similar studies on the CNT networks [92, 98, 99]. It is evidently seen that the electrical conduction of all samples remains unchanged when the temperature is decreasing, until they reach a threshold temperature ($\sim$ 7 K) and then start to decrease. The magnitude of change in film conductivity at temperature below 7 K varies in each sample and the results indicate that thinner films ($<$ 20 nm) are more sensitive to temperature below threshold. In contrast, the conductivity of thicker films ($\geq$ 20 nm) decreases with a little magnitude. We can generally imply that the electronic properties of HC-CNT samples with larger film resistance are more

sensitive to temperature below threshold, which here is observed to be ~ 7 K. Besides, we notice that the electrical conductivity of HC-CNT material is dependent on the film thickness as plotted in Figure 7.4.

The I-V characteristics (I-V_{ds}) and the current-gate response (I-V_g) were also measured at temperatures 300 K and 4.2 K. At room temperature, all HC-CNT samples exhibit a linear drain-current (I$_d$) response (Ohmic behavior) and no gate dependences are indeed observed. While monitored at 4.2 K, all HC-CNT films show a slightly non-linear I-V_{ds} response and the gate transfer characteristics are extremely small, and thus negligible. The results apparently indicate that the HC-CNT material is metallic.

Figure 7.4: The temperature dependent measurement of HC-CNT films with different thicknesses. The conductivity is monitored continuously starting from room temperature down to 4.2 K.

High temperature conduction measurements (25 - 140 °C)

The resistance measurements of HC-CNT samples at high temperature above boiling point of water were carried out in real time while the temperature was being increased, as shown in Figure 7.5. The samples were initially characterized at room temperature (25°C) and their resistances (red traces) as well as the system temperature (blue traces) were continuously recorded by time. The film temperature was then heated up to $\sim$ 140°C, before letting the system cool down again. We find that for thinner

sample (8 nm) the film resistance slightly decreases to $R_{min} \sim 243\ \Omega$ ($\Delta R = R_0$ - $R_{min} \approx 14\ \Omega$, or 5%) while the temperature is increasing to 140°C, but the resistance slightly increases and keeps stable at $R_{max} \sim 265\ \Omega$ which is slightly more than the initial resistance ($R_0 \sim 257\ \Omega$) when the system is getting cooled down to room temperature. The maximum change of film resistance is estimated to be $\Delta R_{max} =$ R_{max} - $R_{min} \approx 22\ \Omega$ (or 8.5%). On the contrary, the resistance of thick film (100 nm) is evidently fluctuating according to the temperature change as increasing while heating up to 135°C and decreasing while cooling down to room temperature. The initial film resistance is $R_0 \sim 5.65\ \Omega$ and the maximum resistance at the highest temperature is given to be $R_{max} \sim 6.1\ \Omega$, thus resulting in a shift-up of $\Delta R = R_{max}$ - $R_0 \approx 0.45\ \Omega$ (or 8%). Eventually the resistance of HC-CNT sample is reducing to be $R_{final} \sim 5.67\ \Omega$, which is quite close to its initial resistance. Interestingly the total change in these HC-CNT samples with different film thicknesses is obtained almost equally in terms of percentage values. We note here that the resistance fluctuations (δR) in HC-CNT thin films are relatively small ($\delta R \sim 8$-8.5 %), and thus can be negligible for high temperature (~ 100°C) electronic applications.
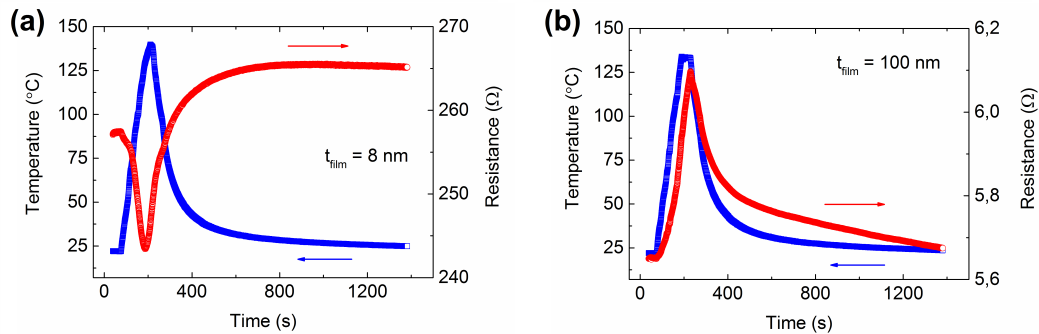


Figure 7.5: The electrical measurements of HC-CNT samples at high temperature above 100°C. The film resistance (red traces) is continuously recorded by time while the device temperature (blue traces) is being increased and later decreased.

Effect of humidity on conduction

Figure 7.6 presents the relative humidity dependence on HC-CNT samples with various film thicknesses. The measurement was performed as a loop starting from initial humidity, then slowly increasing to $\sim 90\%$ and finally decreasing to low humidity again, corresponding to the directions of arrows drawn in Figure 7.6. We observe that HC-CNT films to some extent are sensitive to humidity surrounding their surface as their conductivity diminishes while humidity level is being increased. Interestingly thinner films once again react to the environmental change, in this case humidity, with stronger response than thick films, thus leading to higher sensitivity. The largest decrease in device conductivity measured in the presence of water vapor is observed in

an 8 nm HC-CNT film with almost 1 order of magnitude whereas the rest shows relatively tiny subsidence. However during the backward measurements when releasing humidity, conductivity of all HC-CNT samples is eventually found to be lower than their initial values.

We conclude that the relative stability of the CNT/Hemmicellulose complex material renders it suitable for certain applications where the property of water solubility is major importance.
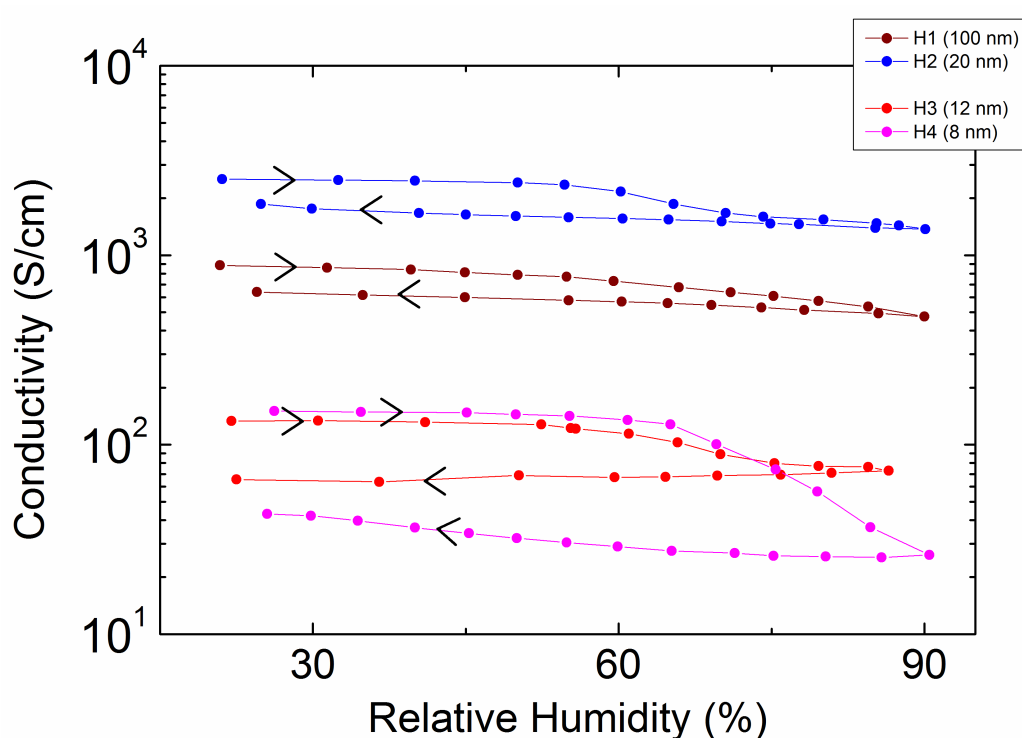
Figure 7.6: The humidity response on device conductivity of HC-CNT samples with different thicknesses. The maximum relative humidity reached in the experiment is $\sim 90\%$. Arrows indicate the direction of the measurements according to the change of humidity level in the system.

8 Conclusions

In this thesis the major goal is to study the effect of various essential factors surrounding the SWNTs. The key parameter to be investigated is the electronic properties of individual SWNT-FET devices that eventually have been successfully explored in Li-salt compound, NCysHFBI protein solution and oxygen/vacuum conditions. The additional study on the electrical properties of hemicellulose-CNT thin films has also been carried out and included in this thesis.

We have demonstrated that a mixture of THF-Naphthalene-Li can intercalate a bundle of CNTs yielding greater solubility and thus resulting in a highly stable suspension. The Li-intercalated CNT solution can be maintained with well dispersion more than 2 years in argon-filled glove box. It has been shown that the Li-treated CNTs have similar electronic properties to intrinsic CNTs when fabricated as FET devices. The effect of active Li-salt solution to the electronic properties of CNT-FETs has also been investigated in glove box at room temperature. We find that the Li-doping mechanism onto CNTs occurs and results to the reversal of their transport properties from p-type to n-type behavior. We also confirm the corresponding mild redox reactions during the liquid-phase alkali-doping process by monitoring the electrical conduction response in real time, in which the ON-state drain current (p-type) slowly decreases to be finally conducting at OFF-state level (n-type). Moreover it has been found that the Li-doping reaction is fully reversible by simply exposing to oxygen and the doping cycle is repeatable.

The effect of protein adsorption onto CNT sidewalls has been explored by means of optical and electrical experiments. We observe the random attachment of hydrophobin molecules onto single suspended SWNTs and also find the film-hanging formation above the neighbor CNTs - acting as supporting beams. For the CNTs spin-coated on Si/SiO_2 substrate, we observe that hydrophobins tend to cover as a nano-film in large area above CNTs and SiO_2 surface. We have demonstrated that the protein adsorption can be electrically monitored in real time via measuring the drain current response. The electronic properties of CNT devices after exposure to hydrophobins are observed to remain p-type characteristics but their ON-state conductance obviously decreases and the conductance change most likely correlates exponentially with the channel length.

We have investigated the electronic properties of asymmetrically contacted SWNT-FET devices - fabricating as one end of nanotube is lying underneath metal contact

whereas another end placing above metal electrode. In our study, we have used palladium and gold as metal electrodes. At room temperature, Pd-contacted SWNT devices with asymmetric configuration are always more resistive than symmetric-structured devices, however this relation cannot be observed in Au-contacted SWNT devices. The low temperature measurements have been carried out down to 4.2 K and we find that the relation of electrical transport properties between different device configurations still remains the same as observed at room temperature (300 K). At 4.2 K, we also observe the asymmetric I-V_{ds} characteristics (diode-like behavior) of asymmetrically Pd-contacted SWNTs but this behavior does not appear with symmetric Pd contacts. We believe that this effect is caused by a thin insulating layer of palladium oxide formed at the interface between Pd and SWNT, thus resulting in larger resistance and tunneling transport. Besides we have demonstrated the sensitivity of Pd-contacted SWNT devices with both structures to oxygen molecules and in almost all devices, the asymmetric sections are more sensitive to the presence of oxygen than the symmetric sections. This can be considered as a consequence of more air-exposed surface area of nanotube in the asymmetric configuration and also the direct electronic modification of nanotube workfunction by oxygen doping at the asymmetric Pd-SWNT junction.

In addition, we have successfully prepared the thin conductive films of hemicellulose-CNT compound with various thicknesses in order of nanometer scale. The ratio between amount of double-walled carbon nanotubes (DWNTs) and hemicellulose is kept fixed at 1:1 (50:50 %wt). The thinnest CNT network film that we have achieved is $\sim$ 8 nm. All the prepared CNT films were electrically measured in different conditions namely in the presence of humidity (up to $\sim$ 90% RH) and in the variation of temperature from 4.2 K to 420 K. The electronic properties of CNT films surrounding with humidity has been investigated. We find that the film conductivity is to some extent influenced by water molecules and the effect is likely dependent on film thickness. We have also shown that the film conductivity remains unchanged while temperature is decreasing, until reaching the threshold temperature ($\sim$ 7 K) the electronic properties of all CNT films start to get affected and then resulting in the reduction of their conductivity. For the range of high temperature (300 K - 420 K or $\sim$ 25-140°C), we observe that the film resistances are slightly influenced and the electrical response changes are relatively small (δR $\sim$ 8-8.5 %). In our study, we have obtained the maximum electrical conductivity of these particular thin films at $\sim 2\times10^3$ S/cm.

References

[1] H. W. Kroto, J. R. Heath, S. C. O'Brien, R. F. Curl, R. E. Smalley, Nature **318** (1985) 162–163.

[2] S. Iijima, Nature **354** (1991) 56–58.

[3] S. Iijima, T. Ichihashi, Nature **363** (1993) 603–605.

[4] D. S. Bethune, C. H. Klang, M. S. de Vries, G. Gorman, R. Savoy, J. Vazquez, R. Beyers, Nature **363** (1993) 605–607.

[5] K. S. Novoselov, A. K. Geim, S. V. Morozov, D. Jiang, Y. Zhang, S. V. Dubonos, I. V. Grigorieva, A. A. Firsov, Science **306** (2004) 666–669.

[6] A. K. Geim, K. S. Novoselov, Nature Materials **6** (2007) 183–191.

[7] A. D. Franklin, M. Luisier, S. J. Han, G. Tulevski, C. M. Breslin, L. Gignac, M. S. Lundstrom, W. Haensch, Nano Letters **12** (2012) 758–762.

[8] L. X. Zheng, M. J. O'Connell, S. K. Doorn, X. Z. Liao, Y. H. Zhao, E. A. Akhadov, M. A. Hoffbauer, B. J. Roop, Q. X. Jia, R. C. Dye, D. E. Peterson, S. M. Huang, J. Liu, Y. T. Zhu, Nature Materials **3** (2004) 673–676.

[9] A. Javey, J. Guo, Q. Wang, M. Lundstrom, H. Dai, Nature **424** (2003) 654–657.

[10] W. Yang, K. R. Ratinac, S. P. Ringer, P. Thordarson, J. J. Gooding, F. Braet, Angew. Chem. Int. Ed. **49** (2010) 2114–2138.

[11] Y. Wang, J. T. W. Yeow, Journal of Sensors (2009) doi:10.1155/2009/493904.

[12] M. Freitag, M. J. O. (Ed.), *Carbon Nanotubes: Properties and Applications*, Taylor & Francis Group, LLC, Boca Raton, FL, 2006.

[13] A. P. Moravsky, E. M. Wexler, R. O. Loutfy, T. Yamada, M. M. (Ed.), *CARBON NANOTUBES: SCIENCE AND APPLICATIONS*, Taylor & Francis Group, LLC, Boca Raton, FL, 2005.

[14] P. D. Kichambare, A. Star, C. S. S. R. K. (Ed.), *Nanotechnologies for the Life Sciences Vol. 8: Nanomaterials for Biosensors*, WILEY-VCH Verlag GmbH & Co. KGaA, Weinheim, 2007.

[15] J.-C. Charlier, X. Blase, S. Roche, Review of Modern Physics **79** (2007) 677–732.

[16] S. N. Kim, J. F. Rusling, F. Papadimitrakopoulos, Advanced Materials **19** (2007) 3214–3228.

[17] K. Varga, K. D. S. (Ed.), *Handbook of Nanophysics: Nanotubes and Nanowires*, Taylor & Francis Group, LLC, Boca Raton, FL, 2011.

[18] T. Ando, NPG Asia Materials **1** (2009) 17–21.

[19] C. Kittel, *Introduction to Solid State Physics 8th ed.*, John Wiley & Sons, Inc., ISBN 0-471-41526-X, 2005.

[20] M. Zheng, A. Jagota, E. D. Semke, B. A. Diner, R. S. Mclean, S. R. Lustig, R. E. Richardson, N. G. Tassi, Nature Materials **2** (2003) 338–342.

[21] D. Tasis, N. Tagmatarchis, V. Georgakilas, M. Prato, Chem. Eur. J. **9** (2003) 4000–4008.

[22] M. C. Hersam, Nature Nanotechnology **3** (2008) 387–394.

[23] J. Liu, A. G. Rinzler, H. Dai, J. H. Hafner, R. K. Bradley, P. J. Boul, A. Lu, T. Iverson, K. Shelimov, C. B. Huffman, F. Rodriguez-Macias, Y. S. Shon, T. R. Lee, D. T. Colbert, R. E. Smalley, Science **280** (1998) 1253–1256.

[24] C. A. Dyke, J. M. Tour, J. Phys. Chem. A **108** (2004) 11151–11159.

[25] Z. Gu, H. Peng, R. H. Hauge, R. E. Smalley, J. L. Margrave, Nano Letters **2** (2002) 1009–1013.

[26] A. Penicaud, P. Poulin, A. Derre, E. Anglaret, P. Petit, J. Am. Chem. Soc. **127** (2005) 8–9.

[27] K. Kurppa, H. Jiang, G. R. Szilvay, A. G. Nasibulin, E. I. Kauppinen, M. B. Linder, Angew. Chem. **119** (2007) 6566–6569.

[28] P. Avouris, Z. Chen, V. Perebeinos, Nature Nanotechnology **2** (2007) 605–615.

[29] S. Datta, *Electronic Transport in Mesoscopic Systems, 1st edition*, Cambridge University Press, UK, 1997.

[30] F. Flores, B. Biel, A. Rubio, F. J. Garcia-Vidal, C. Gomez-Navarro, P. de Pablo, J. Gomez-Herrero, J. Phys.: Condens. Matter **20** (2008) 304211–7.

[31] S. Heinze, J. Tersoff, R. Martel, V. Derycke, J. Appenzeller, P. Avouris, Physical Review Letters **89** (2002) 106801–4.

[32] J. Singh, *Semiconductor Devices: Basic Principles*, John Wiley & Sons, Inc., New York, 2001.

[33] Z. Chen, J. Appenzeller, J. Knoch, Y. Lin, P. Avouris, Nano Letters **5** (2005) 1497–1502.

[34] S. R. Elliot, *The Physics and Chemistry of Solids, first, corrected edition*, John Wiley & Sons Inc., UK, 2005.

[35] P. Liu, Q. Sun, F. Zhu, K. Liu, K. Jiang, L. Liu, Q. Li, S. Fan, Nano Letters **8** (2008) 647–651.

[36] L. Yang, S. Wang, Q. Zeng, Z. Zhang, L. M. Peng, Small **9** (2013) 1225–1236.

[37] S. Datta, *Quantum Transport: Atom to Transistor, first edition*, Cambridge University Press, UK, 2007.

[38] T. Durkop, S. A. Getty, E. Cobas, M. S. Fuhrer, Nano Letters **4** (2004) 35–39.

[39] M. Rinkio, A. Johansson, G. S. Paraoanu, P. Torma, Nano Letters **9** (2009) 643–647.

[40] B. Shan, K. Cho, Physical Review B **70** (2004) 233405.

[41] Nanocyl http://www.nanocyl.com/en/Products–Solutions/Products/Research–Grades/Single–Wall–Carbon–Nanotubes (read on 25.3.2014).

[42] A. E. Vladar, M. T. Postek, Microsc Microanal **11** (2005) DOI: 10.1017/S1431927605507785.

[43] D. Mann, A. Javey, J. Kong, Q. Wang, H. Dai, Nano Letters **3** (2003) 1541–1544.

[44] A. Makarovski, A. Zhukov, J. Liu, G. Finkelstein, Physical Review B **76** (2007) 161405(R).

[45] R. Martel, ACS Nano **2** (2008) 2195–2199.

[46] A. Ortiz-Acevedo, H. Xie, V. Zorbas, W. M. Sampson, A. B. Dalton, R. H. Baughman, R. K. Draper, I. H. Musselman, G. R. Dieckmann, J. Am. Chem. Soc. **127** (2005) 9512–9517.

[47] M. J. O'Connell, S. M. Bachilo, C. B. Huffman, V. C. Moore, M. S. Strano, E. H. Haroz, K. L. Rialon, P. J. Boul, W. H. Noon, C. Kittrell, J. Ma, R. H. Hauge, R. B. Weisman, R. E. Smalley, Science **297** (2002) 593–596.

[48] R. J. Chen, Y. Zhang, D. Wang, H. Dai, J. Am. Chem. Soc. **123** (2001) 3838–3839.

[49] N. Nakashima, Y. Tomonari, H. Murakami, Chemistry Letters (2002) 638–639.

[50] Y. L. Zhao, J. F. Stoddart, Accounts of Chemical Research **42** (2009) 1161–1171.

[51] M. Holzinger, O. Vostrowsky, A. Hirsch, F. Hennrich, M. Kappes, R. Weiss, F. Jellen, Angew. Chem. Int. Ed. **40** (2001) 4002–4005.

[52] J. Chen, M. A. Hamon, H. Hu, Y. Chen, A. M. Rao, P. C. Eklund, R. C. Haddon, Science **282** (1998) 95–98.

[53] S. Fogden, C. A. Howard, R. K. Heenan, N. T. Skipper, M. S. P. Shaffer, ACS Nano **6** (2012) 54–62.

[54] C. Zhou, J. Kong, E. Yenilmez, H. Dai, Science **290** (2000) 1552–1555.

[55] M. Bockrath, J. Hone, A. Zettl, P. L. McEuen, A. G. Rinzler, R. E. Smalley, Physical Review B **61** (2000) 10606–10608(R).

[56] M. Inagaki, O. Tanaike, Synthetic Metals **73** (1995) 77–81.

[57] E. Jouguelet, C. Mathis, P. Petit, Chemical Physics Letters **318** (2000) 561–564.

[58] P. Yotprayoonsak, K. Hannula, T. Lahtinen, M. Ahlskog, A. Johansson, Carbon **49** (2011) 5283–5291.

[59] K. B. Shelimov, R. O. Esenaliev, A. G. Rinzler, C. B. Huffman, R. E. Smalley, Chemical Physics Letters **282** (1998) 429–434.

[60] M. B. Linder, Current Opinion in Colloid & Interface Science **14** (2009) 356–363.

[61] G. R. Szilvay, A. Paananen, K. Laurikainen, E. Vuorimaa, H. Lemmetyinen, J. Peltonen, M. B. Linder, Biochemistry **46** (2007) 2345–2354.

[62] Z. Wang, M. Lienemann, M. Qiau, M. B. Linder, Langmuir **26** (2010) 8491–8496.

[63] J. Hakanpaa, A. Paananen, S. Askolin, T. Nakari-Setala, T. Parkkinen, M. Penttila, M. B. Linder, J. Rouvinen, J. Biol. Chem. **279** (2004) 534–539.

[64] J. Hakanpaa, G. R. Szilvay, H. Kaljunen, M. Maksimainen, M. LINDER, J. Rouvinen, Protein Science **15** (2006) 2129–2140.

[65] J. Hakanpaa, M. Linder, A. Popov, A. Schmidt, J. Rouvinen, Acta Crystallographica D **62** (2006) 356–367.

[66] G. R. Szilvay, T. Nakari-Setala, M. B. Linder, Biochemistry **45** (2006) 8590–8598.

[67] P. Laaksonen, M. Kainlauri, T. Laaksonen, A. Shchepetov, H. Jiang, J. Ahopelto, M. B. Linder, Angew. Chem. Int. Ed. **49** (2010) 4946–4949.

[68] M. Qin, S. Houa, L. Wang, X. Feng, R. Wang, Y. Yang, C. Wang, L. Yu, B. Shao, M. Qiao, Colloids and Surfaces B **60** (2007) 243–249.

[69] P. Laaksonen, J. Kivioja, A. Paananen, M. Kainlauri, K. Kontturi, J. Ahopelto, M. B. Linder, Langmuir **25** (2009) 5185–5192.

[70] J. M. Kivioja, K. Kurppa, M. Kainlauri, M. B. Linder, J. Ahopelto, Applied Physics Letters **94** (2009) 183901.

[71] Z. Wang, Y. Wang, Y. Huang, S. Li, S. Feng, H. Xu, M. Qiao, Carbon **48** (2010) 2890–2898.

[72] X. Wang, H. Wang, Y. Huang, Z. Zhao, X. Qin, Y. Wang, Z. Miao, Q. Chen, M. Qiao, Biosensors and Bioelectronics **26** (2010) 1104–1108.

[73] T. Laaksonen, P. Ahonen, C. Johans, K. Kontturi, ChemPhysChem **7** (2006) 2143–2149.

[74] A. Koshio, M. Yudasaka, S. Iijima, Chemical Physics Letters **356** (2002) 595.

[75] P. Myllyperkio, O. Herranen, J. Rintala, H. Jiang, P. R. Mudimela, Z. Zhu, A. G. Nasibulin, A. Johansson, E. I. Kauppinen, M. Ahlskog, M. Pettersson, ACS Nano **4** (2010) 6780–6786.

[76] L. Huang, B. White, M. Y. Sfeir, M. Huang, H. X. Huang, S. Wind, J. Hone, S. O'Brien, J. Phys. Chem. B **110** (2006) 11103–11109.

[77] M. Rinkio, A. Johansson, M. Y. Zavodchikova, J. J. Toppari, A. G. Nasibulin, E. I. Kauppinen, P. Torma, New Journal of Physics **10** (2008) 103019.

[78] W. Kim, A. Javey, O. Vermesh, Q. Wang, Y. Li, H. Dai, Nano Letters **3** (2003) 193–198.

[79] K. Besteman, J. O. Lee, F. G. M. Wiertz, H. A. Heering, C. Dekker, Nano Letters **3** (2003) 727–730.

[80] I. Heller, A. M. Janssens, J. Mannik, E. D. Minot, S. G. Lemay, C. Dekker, Nano Letters **8** (2008) 591–595.

[81] K. S. Chichak, A. Star, M. V. P. Altoe, J. F. Stoddart, Small **1** (2005) 452–461.

[82] M. H. Yang, K. B. Teo, W. I. Milne, D. G. Hasko, Applied Physics Letters **87** (2005) 253116.

[83] S. Fuchs, T. Hahn, H. G. Lintz, Chem. Eng. Process. **33** (1994) 363.

[84] H. Gabasch, W. Unterberger, K. Hayek, et al., Surface Science **600** (2006) 2980–2989.

[85] E. Lundgren, G. Kresse, C. Klein, M. Borg, J. N. Andersen, M. D. Santis, Y. Gauthier, C. Konvicka, M. Schmid, P. Varga, Physical Review Letters **88** (2002) 246103.

[86] A. Juutilainen, A. Volodin, M. Ahlskog, Physical Review B **86** (2012) 045405.

[87] P. G. Collins, K. Bradley, M. Ishigami, A. Zettl, Science **287** (2000) 1801.

[88] S. H. Jhi, S. G. Louie, M. L. Cohen, Physical Review Letters **85** (2000) 1710.

[89] H. M. Manohara, E. W. Wong, E. Schlecht, B. D. Hunt, P. H. Siegel, Nano Letters **5** (2005) 1469.

[90] T. Nishino, I. Matsuda, K. Hirao, Macromolecules **37** (2004) 7683–7687.

[91] D. Klemm, F. Kramer, S. Moritz, T. Lindstrom, M. Ankerfors, D. Gray, A. Dorris, Angew. Chem. Int. Ed. **50** (2011) 5438–5466.

[92] H. Koga, T. Saito, T. Kitaoka, M. Nogi, K. Suganuma, A. Isogai, Biomacromolecules **14** (2013) 1160–1165.

[93] D. H. Page, F. El-Hosseiny, K. Winkler, Nature **229** (1971) 252–253.

[94] A. K. Bledzki, J. Gassan, Prog. Polym. Sci. **24** (1999) 221–274.

[95] URL http://www.princeton.edu/∼achaney/tmve/wiki100k/docs/Hemicellulose.html (read on 25.3.2014).

[96] URL http://en.wikipedia.org/wiki/Cellulose (read on 25.3.2014).

[97] URL http://students.chem.tue.nl/ifp19/biomass.htm (read on 25.3.2014).

[98] S. H. Yoon, H. J. Jin, M. C. Kook, Y. R. Pyun, Biomacromolecules **7** (2006) 1280–1284.

[99] L. Ichkitidze, V. Podgaetsky, S. Selishchev, E. Blagov, V. Galperin, Y. Shaman, A. Pavlov, E. Kitsyuk, Materials Sciences and Applications **4** (2013) 1–7.

[100] D. H. Kim, S. Y. Park, J. Kim, M. Park, Journal of Applied Polymer Science **117** (2010) 3588–3594.

[101] nEMCEl Ltd. URL http://www.nemcel.fi/.

[102] Patent # PCT/FI2013/000019.